POLITECNICO DI MILANO

FACOLTÀ DI INGEGNERIA DEI SISTEMI

Corso di Laurea Magistrale
in Ingegneria Matematica

Third Generation Solar Cells: Modeling and Simulation

Relatore: Prof. Riccardo Sacco
Correlatori: Ing. Carlo de Falco
Prof. Maurizio Verri

Tesi di laurea di:
Maurizio Mansueto Cogliati Matr. 720865
Matteo Porro Matr. 724724

Anno Accademico 2009-2010

Contents

List of Figures

List of Tables

Riassunto della tesi

La presente tesi di Laurea Magistrale in Ingegneria Matematica è il risultato di un anno di lavoro svolto presso il Dipartimento di Matematica del Politecnico di Milano e in stretta collaborazione con il Prof. Marco Sampietro e l'Ing. Dario Natali del Dipartimento di Elettronica e Informazione per quanto riguarda i contenuti di Fisica ed Elettronica. La ricerca si inserisce nell'ambito generale delle *energie rinnovabili* e si focalizza sulla modellazione matematica e la simulazione numerica di celle fotovoltaiche di nuova generazione. La tesi si articola in sei capitoli il cui contenuto viene descritto nel seguito.

Capitolo 1: An introduction to photovoltaics

Motivazioni socio-economiche

Uno dei problemi più importanti che l'umanità dovrà affrontare nel corso di questo secolo è quello della produzione di energia poiché, di fronte alla continua crescita della popolazione globale e all'industrializzazione dei paesi in via di sviluppo, il fabbisogno energetico sarà in aumento e le attuali modalità di produzione non sono sostenibili per l'ecosistema della Terra. Per questo motivo la comunità internazionale con il Protocollo di Kyoto e l'Unione Europea con l'accordo del 2007 [58] si sono impegnate nella riduzione alle emissioni di diossido di carbonio, rispettivamente entro il 2012 e il 2020. In particolare il Consiglio Europeo ha stabilito che tale riduzione debba essere del 20% e che entro il 2020 i Paesi membri debbano produrre almeno il 20% dell'energia della quale necessitano da fonti rinnovabili.
Nonostante le menzionate linee guida legislative, la tecnologia del rinnovabile non ha ancora raggiunto maturità e un livello di avanzamento tali da rendere conveniente il ricorso a questo tipo di energia rispetto alle convenzionali fonti fossili e molta attività ricerca è prevista per il futuro, anche sotto la spinta di congrui finanziamenti dei governi nazionali e di investimenti delle aziende del settore.

L'energia solare

L'energia solare riveste un ruolo importante tra le varie fonti rinnovabili ed è forse quella che presenta i migliori margini di miglioramento in termini di riduzione dei costi e utilizzabilità. Esistono principalmente due modalità per ottenere energia dalla radiazione solare e sono:

- il solare termodinamico a concentrazione nella quale una grande quantità di luce è concentrata in uno spazio limitato per generare calore, utilizzato per riscaldare acqua che, a seconda della dimensione dell'impianto, può essere destinata ad uso domestico o ad azionare le turbine di una centrale per la produzione di energia elettrica;

- l'effetto fotoelettrico proprio di alcuni metalli e semiconduttori. Questa tecnologia ha il vantaggio di essere l'unica finora impiegata per la permettere la produzione diretta di elettricità.

Le prime celle sviluppate sono state quelle basate sul silicio cristallino e al giorno d'oggi esse hanno raggiunto un elevato livello di efficienza, accompagnato però da un elevato costo, soprattutto dovuto ai materiali necessari, che ne limita la diffusione. Nel tentativo di ridurre i costi di produzione la ricerca ha portato al concepimento di celle costruite con materiali alternativi al silicio, dette di seconda generazione, che utilizzano una tecnologia a film sottile e hanno raggiunto efficienze tali da permetterne la commercializzazione.
Le celle di più recente sviluppo, dette appunto di terza generazione, hanno approcci meno convenzionali per la produzione dell'elettricità e utilizzano materiali radicalmente diversi da quelli delle generazioni precedenti. All'interno di quest'ultima classe si possono individuare due principali tipologie di celle: celle solari dye-sensitized e celle solari organiche.

Capitolo 2: Dye sensitized solar cells

Le celle elettrochimiche di tipo Dye Sensitized Solar Cell (DSSC) sono state proposte da M. Graetzel nel 1991 [60]. Il dispositivo è costituito principalmente da uno strato nanoporoso di semiconduttore, solitamente ossido di titanio, rivestito da un colorante e immerso in una soluzione di ioni iodio (I^-) e triiodio (I_3^-), il tutto racchiuso tra due vetri conduttori, che fungono da anodo e catodo. Quando la cella viene illuminata avvengono i seguenti fenomeni illustrati in Fig. 2.3:

1. i fotoni vengono assorbiti dalle molecole di colorante le quali aumentando il proprio livello energetico passano a uno stato eccitato;

2. la molecola eccitata inietta un elettrone nella banda di conduzione del semiconduttore. La carica fotogenerata diffonde attraverso l'ossido di titanio fino a raggiungere l'anodo, dal quale esce dalla cella e raggiunge il catodo per mezzo del carico collegato al dispositivo;

3. l'elettrone rientra nella cella attraverso una reazione di ossidoriduzione con il triiodio (secondo la relazione (2.1)) generando una molecola di I^-;

4. lo ione iodio viene trasportato all'interno dell'elettrolita fino a contatto con il catione della molecola di colorante, riportandola allo stato neutro.

A tutt'oggi il funzionamento delle DSSC è oggetto di studio in quanto i fenomeni che avvengono localmente all'interfaccia sono particolarmente complessi e necessitano di ulteriori analisi [26]. La particolarità che contraddistinge queste celle rispetto ai convenzionali dispositivi al silicio è che il ciclo di funzionamento è rigenerativo e i meccanismi di generazione e trasporto della carica fotogenerata non avvengono interamente nel semiconduttore.
I modelli utilizzati nella presente tesi per la descrizione del funzionamento dei dispositivi elettrochimici sono costituiti da sistemi di equazioni alle derivate parziali non lineari di tipo diffusione-trasporto-reazione fortemente accoppiati completati dall'equazione di Poisson per il calcolo di un campo elettrico consistente con la distribuzione di carica e da equazioni alle derivate ordinarie che descrivono la cinetica delle reazioni chimiche che avvengono all'interno della soluzione elettrolitica. Per celle di particolare struttura (caratterizzate da un non trascurabile spessore dell'elettrolita), l'equazione di Poisson può essere legittimamente ridotta a una semplice condizione di elettroneutralità. Consistentemente con la natura rigenerativa delle celle elettrolitiche considerate, è necessario imporre condizioni di tipo integrale che esprimono la conservazione delle varie specie ioniche presenti nella soluzione. L'imposizione di tali condizioni nell'ambito della formulazione debole del problema considerato è discussa in dettaglio nel Capitolo 4.

Capitolo 3: Organic solar cells

Il carbonio e il silicio presentano una configurazione elettrica molto simile in quanto hanno lo stesso numero di elettroni nell'orbitale più esterno, e per questo motivo particolari composti molecolari e polimerici del carbonio manifestano apprezzabili proprietà conduttive. Tali materiali hanno la caratteristica, detta *coniugazione*, di avere orbitali molecolari delocalizzati e ciò si verifica quando gli atomi di carbonio sono legati tra loro attraverso doppi legami covalenti alternati a legami semplici. L'orbitale non occupato avente il livello energetico più basso è detto LUMO mentre

con HOMO si indica quello occupato a energia più alta. Tali livelli energetici agiscono rispettivamente alla stessa maniera della banda di conduzione e di quella di valenza dei semiconduttori inorganici, permettendo lo spostamento degli elettroni all'interno della molecole stesse mentre il passaggio intermolecolare è dovuto a un fenomeno denominato *hopping*, composizione degli effetti di vibrazioni fononiche e tunneling quantistico. I semiconduttori organici hanno lo svantaggio di presentare basse mobilità per i portatori di carica ma hanno costi molto contenuti e sono facilmente solubili, cosa che permette la produzione di celle con tecniche a basso costo utilizzate dall'industria della stampa.
Quando colpiti da radiazione visibile o ultravioletta, a differenza dei semiconduttori inorganici, i materiali organici non rilasciano una coppia di portatori di carica di segno opposto, ma sono caratterizzati dalla seguente complessa fenomenologia descritta in Fig. 3.8(a), Fig. 3.8(b) e Fig. 3.9:

1. formazione di stati eccitati detti *eccitoni* nei quali le cariche si attraggono vicendevolmente per mezzo di forti interazioni coulombiane;

2. moto degli eccitoni per diffusione verso l'interfaccia dei due materiali con differente affinità elettronica, possando a un nuovo stato, detto *polarone* nel quale tra le cariche vi è ancora un legame ma di minore energia rispetto a quello degli eccitoni.

3. dissociazione dei polaroni intrappolati alla superficie in due cariche di segno opposto nei due materiali, i quali assumono i nomi di *donore* e *accettore*;

4. moto delle cariche per diffusione e convezione verso gli elettrodi.

È possibile raggruppare i tipi di morfologie utilizzati per l'organizzazione interna di accettore e donore in tre categorie. La più semplice tra di esse è quella delle celle *bilayer* nelle quali i due materiali sono disposti a strati planari a formare un dispositivo di facile produzione ma caratterizzato da bassa efficienza. Più avanzata è la morfologia a *eterogiunzione di volume* (BHJ) nella quale donore e accettore sono mescolati fino a livello nanometrico a formare una struttura convoluta che assicura una grande area di interfaccia per la separazione dei portatori ma che, al contempo, è caratterizzata da una bassa mobilità degli stessi. Dispositivi di più recente concepimento prevedono la nanostrutturazione dello strato fotoattivo al fine di massimizzare generazione e trasporto di carica.
I modelli utilizzati nella presente tesi per la descrizione del funzionamento dei dispositivi organici sono costituiti da sistemi di equazioni alle derivate parziali non lineari di tipo diffusione-trasporto-reazione fortemente accoppiati completati dall'equazione

di Poisson per il calcolo di un campo elettrico consistente con la distribuzione di carica e da equazioni alle derivate ordinarie che descrivono la cinetica della densità di polaroni. Nel caso particolare dei dispositivi bilayer per tenere conto di fenomeni con scale spaziali caratteristiche molto diverse, vengono introdotte appropiate relazioni che legano i flussi di portatori di carica attraverso l'interfaccia fra i diversi materiali alla densità (per unità di area) di polaroni intrappolati a cavallo dell'interfaccia stessa.

Capitolo 4: Numerical methods

La struttura matematica di tipo multifisica e multiscala che caratterizza i modelli fisici discussi nei Capitoli 2 e 3 si presta bene a una formulazione unificata che comprende:

- un sistema di N equazioni alle derivate parziali di tipo parabolico con termini di convezione in forma di gradiente che rappresentano altrettante equazioni di continuità per le N specie chimiche in gioco;
- un'equazione di Poisson per la descrizione autoconsistente del campo elettrico associato alle N specie chimiche di cui sopra;
- un sistema di M equazioni differenziali alle derivate ordinarie per tenere conto di eventuali reazioni chimiche volumetriche e/o di interfaccia;
- un sistema di $Q \leq N$ condizioni integrali che esprimono la conservazione delle specie ioniche.

A fronte di questa complessa formulazione differenziale-algebrico-integrale del problema, nel presente capitolo vengono illustrati i procedimenti numerici appropriati per gestire in modo efficiente e accurato ciascuna delle peculiarità sopra menzionate. In particolare:

- nella Sezione 4.1 viene descritto il metodo di Rothe utilizzato per la semidiscretizzazione in tempo di ciascuna equazione parabolica accoppiato con l'uso di metodi BDF, scelti per la loro capacità di trattare sistemi differenziali caratterizzati da scale temporali variabili;
- nella Sezione 4.2 viene descritta l'iterazione funzionale di Newton per la linearizzazione del sistema di equazioni ellittiche derivante dalla semidiscretizzazione di cui al punto precedente;

- nella Sezione 4.3 viene descritto il metodo di discretizzazione Galerkin elementi finiti di tipo EAFE utilizzato per l'approssimazione numerica del problema di diffusione-trasporto-reazione in forma conservativa;

- nella Sezione 4.4 viene descritta la metodologia di *Substructuring* impiegata per la gestione del problema di diffusione-trasporto-reazione introdotto al punto precedente all'interno di un dominio di calcolo fortemente eterogeneo. Particolare attenzione viene posta al trattamento delle condizioni di trasmissione all'interfaccia tra i due sottodomini;

- nell'ultima Sezione 4.5 viene infine descritta la formulazione debole con moltiplicatore di Lagrange per l'imposizione delle condizioni integrali che esprimo la conservazione della carica.

Capitolo 5: Numerical simulations

In questo capitolo si affronta una approfondita analisi di validazione dei modelli e delle metodologia di risoluzione illustrati nei Capitoli 2, 3 e 4, attraverso la simulazione a calcolatore di numerosi casi test relativi a celle fotovoltaiche elettrochimiche e a polimeri organici. Nel condurre questa analisi si è costantemente tenuta in considerazione la letteratura scientifica più aggiornata del settore.
Precisamente, per quanto riguarda le celle elettrochimiche è stata condotta una dettagliata simulazione del dispositivo studiato in [61]. Trattasi di una schematizzazione unidimensionale di una struttura costituita da uno strato nanoporoso di ossido di titanio e uno strato di elettrolita posti in contatto con l'esterno tramite due elettrodi che fungono rispettivamente da catodo e anodo. Il trasporto di massa e il trasporto degli elettroni fotogenerati vengono descritti dal sistema di equazioni alle derivate parziali corredato dalle condizioni integrali di elettroneutralità oggetto del Capitolo 2. In una preliminare validazione degli algoritmi computazionali viene condotta una analisi dettagliata delle prestazioni della cella in funzione del rate di illuminazione fotonica. Successivamente, l'analisi viene estesa al caso in cui sia incluso il trasporto delle cariche fotogenerate. I risultati ottenuti mostrano l'importanza di disporre di un sufficiente strato di elettrolita per incrementare le reazioni di ossidoriduzione all'interfaccia con la struttura nanoporosa di ossido di titanio, importanti per l'efficiente funzionamento del dispositivo.
Relativamente allo studio delle celle fotovoltaiche a polimeri organici, sono state condotte simulazioni di due configurazioni morfologiche, corrispondenti al caso di celle BHJ e di celle bilayer interdigitate.
Per quanto riguarda le prime, trattasi di calcoli atti a convalidare le prestazioni del

codice bidimensionale sviluppato nella tesi rispetto ad analoghe simulazioni condotte in una geometria monodimensionale in un precedente lavoro di tesi [23] e in [20]. Vengono in particolare analizzati i transitori di accensione della cella in funzione di diverse condizioni di illuminazione e illustrati gli andamenti delle principali grandezze che determinano il comportamento elettrico del dispositivo (concentrazioni dei portatori fotogenerati e campo elettrico). I risultati ottenuti confermano pienamente le conclusioni tratte nei precedenti riferimenti bibliografici.
Per quanto riguarda le celle bilayer, trattasi di un importante contributo originale di questa tesi. Il modello considerato è una estensione e ri-interpretazione di quanto proposto recentemente in letteratura in [78] dove si affronta la simulazione numerica di blend polimerici separati da una superficie di interfaccia a larga dimesione allo scopo di aumentare l'efficienza di conversione della cella. I complessi fenomeni che governano il processo di fotogenerazione interfacciale vengono descritti nella tesi attraverso opportune condizioni di trasmissione non lineari, mentre il trasporto della carica fotogenerata nelle relative regioni accettore e donore del dispositivo è regolato dal classico modello Drift-Diffusion, caratterizzato da mobilità dipendenti dal campo elettrico secondo la relazione fenomenologica di Poole-Frankel. I risultati ottenuti sono in ottimo accordo con quanto illustrato nell'articolo di letteratura precedentemente citato e mostrano come l'efficienza della cella dipenda in modo critico dall'aumento della profondità di interdigitazione tra materiale accettore e materiale donore, e/o dall'infittimento dell'interfaccia medesima.

Capitolo 6: Concluding remarks and future work

Questo capitolo conclusivo è dedicato a riassumere i principali contributi forniti in questa tesi alla modellazione e simulazione numerica di dispositivi avanzati per la conversione elettrica dell'energia solare, individuando inoltre alcuni spunti per sviluppi futuri di ricerca, tra cui:

- descrizione completa della distribuzione della radiazione elettromagnetica all'interno dei dispositivi, al fine di migliorare il potere predittivo del modello;
- confronto dei risultati ottenuti tramite simulazioni numeriche con dati sperimentali, in modo da validare il modello e calibrare i parametri;
- simulazione multidimensionale delle celle DSSC considerando in maniera dettagliata le reazioni chimiche che avvengo all'interfaccia;
- considerazione degli effetti del disordine energetico sull'iniezione e il trasporto di carica nelle celle OSC.

Abstract

The aim of this Master thesis work is the development and the implementation of computational models for third-generation solar cells.
The thesis is organized in six chapters whose content is shortly described below.
Chapter 1 contains a brief presentation of renewable energies market, solar power in general followed by an introduction to the two main families of third generation cells, namely Dye Sensitized Solar Cells (DSSCs) and Organic Solar Cells (OSCs).
In **Chapter 2** the physical phenomena driving the operation of DSSCs are presented in detail and two mathematical models are proposed for them.
Chapter 3 is devoted to introduce the basic physics of OSCs. Two model are proposed for different types of morphologies along with several parameter models.
Chapter 4 describes the mathematical methods used to discretize and to solve the equations of the models.
In **Chapter 5** the numerical results of the simulations are described for both DSSCs and OSCs, considering different operating conditions and parameter values.
Finally in **Chapter 6** some conclusions and perspectives for future activities are presented.

Chapter 1

An introduction to photovoltaics

In 2003, during a lecture at Rice University, the Nobel prize Richard Errett Smalley drew up a list of which would have been the *humanity's top ten problems* in the following fifty years [70]. The list read:

1. energy
2. water
3. food
4. environment
5. poverty
6. terrorism and war
7. disease
8. education
9. democracy
10. population.

It is noticeable that energy is at the first place despite the much more important attention that media and public figures reserve to the other issues that occupy the following places, but this is somehow obvious from a rational point of view, since many of the them, above all environment, depend on or are related with it. International community and national governments are well aware that many efforts have to be made on this topic and Kyoto Protocol is the main attempt in that direction, in which developed countries committed to reduce the emissions of *greenhouse gases* (carbon dioxide, methane, nitrous oxide, sulphur hexafluoride), hydrofluorocarbons and perfluorocarbons of 5.2 percent from 1990 levels by 2012. However its effectiveness is in serious doubt since United States still have not ratified it and the conference held in Copenhagen in 2009, whose purpose was to establish the objectives of a post-2012 agreement, ended without binding decisions. The main source of greenhouse gases is fossil fuel combustion and for this reason the goal of limiting emissions is equivalent to finding new methods for using renewable energy along with avoiding energy waste. In the meanwhile, in 2007, European Community established its own rules on the matter [58], deciding that carbon dioxide emissions should decrease by 20 percent and that 20 percent of the energy produced in EU

should originate from *renewable energy* sources not later than 2020.

1.1 Renewable energy

According to the International Energy Agency, renewable energy is the one derived from natural processes that are constantly replenished. This definition then includes electricity and heat generated from wind, sunlight, biomass, geothermal resources, hydropower, oceans, biofuels and hydrogen derived from renewable resources. These energies are unlimited on the human time scale, so that their use does not harm the natural resources for future generations. Non-renewable energies, instead, have very long renewal time compared to the actual consumption rate (e.g. fossil fuels as oil, coal, natural gas) or are not inexhaustible on the human time scale (as ^{235}U isotope for nuclear energy), so they are expected to reach their limit in the near future. When the term *alternative sources* is used the reference is to all the sources different from fossil fuels, then grouping renewable energy and nuclear one.
Fig. 1.1 shows a comparison between fuel shares for primary energy, which includes every form of energy used in the world that has not been subjected to any conversion or transformation process between 1973 and 2008. Even if increased in absolute value, the amount from renewable sources remained constant in percentage (around 12.5%) for 35 years. Data are taken from [1]. Fig. 1.2, instead, shows the same com-

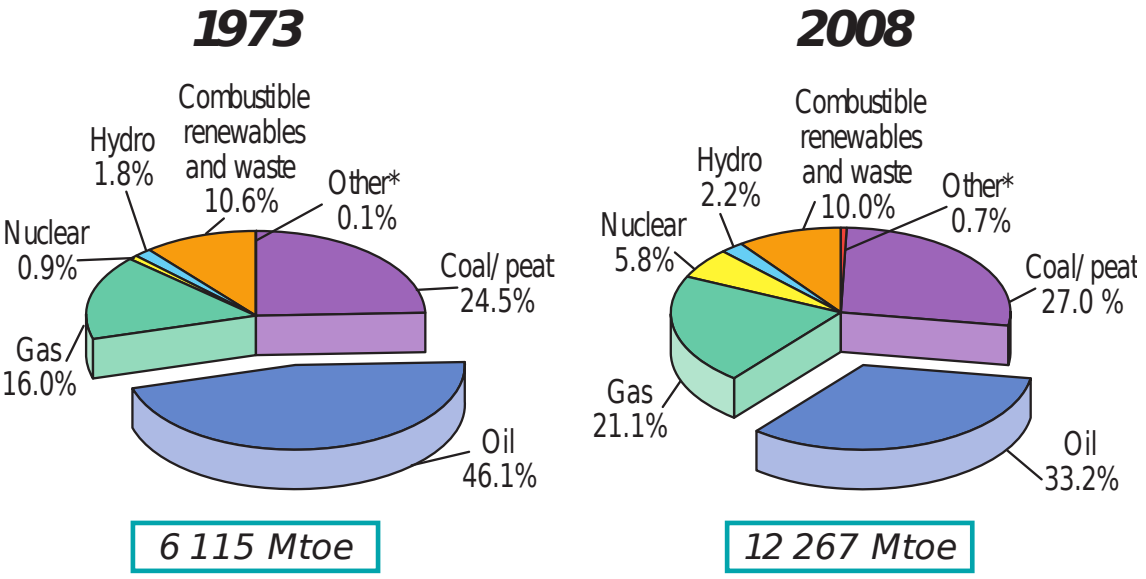

Figure 1.1: Comparison of fuel shares of world primary energy supply between 1973 and 2008.

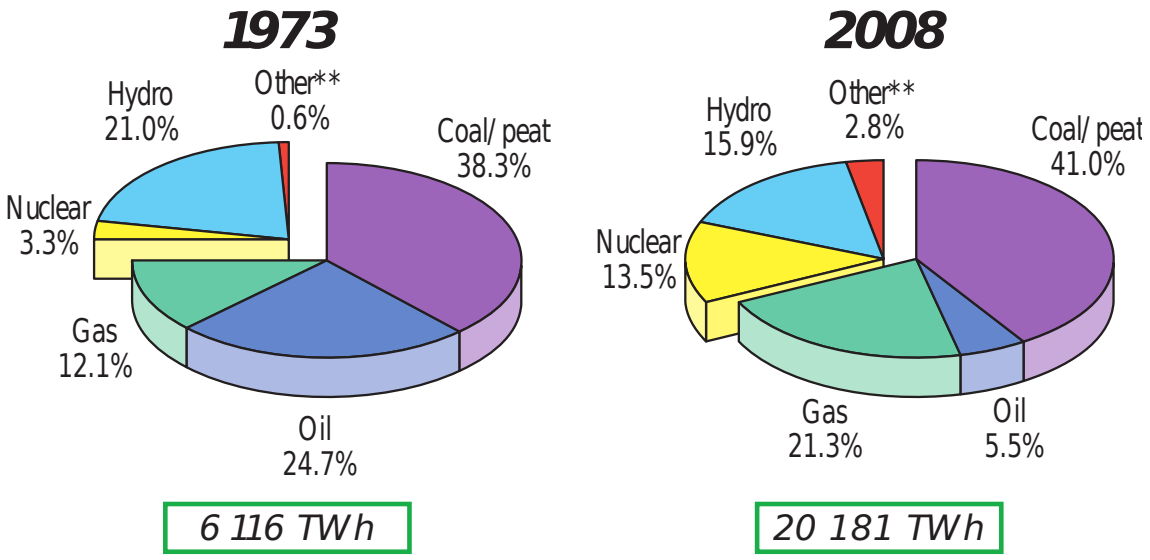

Figure 1.2: Comparison of fuel shares for electricity production between 1973 and 2008.

parison, referred to electricity production data. This is, in fact, the field in which renewable sources are the most suitable to be used and this is testified by the rise in percentage of the field in red, which does not include hydropower, whose contraction is mostly due to the fact that the best locations for the plants have already been occupied.

Anyway the two figures we showed cannot represent the latest progress of renewables diffusion, work which is done better by Fig. 1.3 and Fig. 1.4 [28]. The number of countries with renewable policy targets is continuously rising and despite the global crisis the investments have not experienced a reduction. The total power capacity from renewables (not including the one from big hydro plants) raised of more than the 20 percent just in 2009, from 250 to 305 GW, and for the second year in a row, in both the United States and Europe, more renewable power capacity was added

SELECTED INDICATORS	2007	2008	2009
Investment in new renewable capacity (annual)	104	130	150 billion USD
Renewables power capacity (including only small hydro)	210	250	305 GW
Renewables power capacity (including all hydro)	1,085	1,150	1,230 GW
Hydropower capacity (existing, all sizes)	920	950	980 GW
Wind power capacity (existing)	94	121	159 GW
Solar PV capacity, grid-connected (existing)	7.6	13.5	21 GW
Solar PV production (annual)	3.7	6.9	10.7 GW
Solar hot water capacity (existing)	125	149	180 GWth
Ethanol production (annual)	53	69	76 billion liters
Biodiesel production (annual)	10	15	17 billion liters

Figure 1.3: Several indicators for renewables in the period 2007-2009.

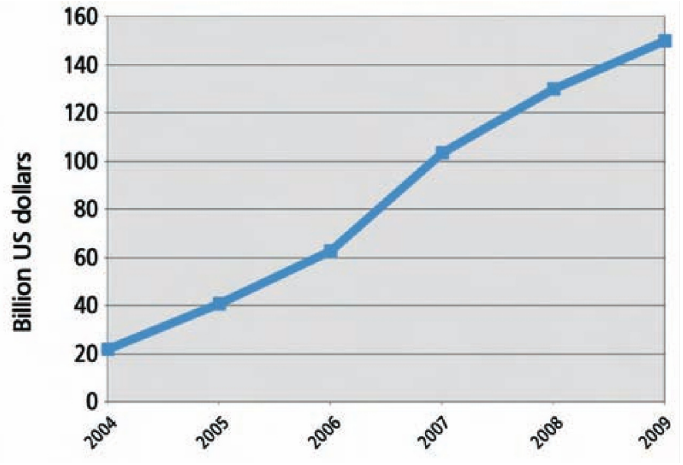

Figure 1.4: Global investments in renewable energy.

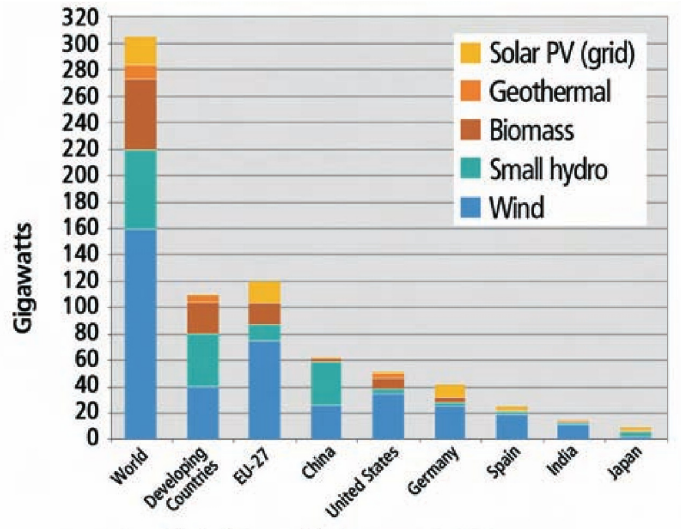

Figure 1.5: Renewable power capacities (excluded large hydro plants) by country.

than conventional one [28]. Great contribution is due to the increased commitment of China that added 37 GW of renewable power capacity, more than any other country in the world, mostly in hydro (31 GW) and wind power (13.8 GW), doubling in one year the capacity for the latter. Solar photovoltaics additions registered a record too with 7 GW with Germany as the top market, followed by Italy and Japan. Solar thermal capacity increased too with a rate of 20%. A very important aspect for the diffusion of renewable energies, probably the most important one, which is responsible of the boost of the latest years, is that the state governments implemented convenient tax subsides, rebates and financings to encourage the consumers and the companies to switch to them. For example in Italy, feed-in tariff incentives "conto energia" and "nuovo conto energia" gave great impulse to the installation of solar plants in the country with more than new 100000 systems for a total power of

1750MW [38].
Renewable technologies are more versatile than conventional ones since they are suitable for both large scale projects and small off-grid applications, e.g. in rural and remote areas, where common supply lines are not present and energy is a crucial problem. Moreover solar photovoltaic and thermodynamic systems are addressed among the best solutions for developing countries [27].
Forecasts for the future see a progressive growth of the importance of renewable energies. Fig. 1.6 [1] shows the projections for the fuel shares of total primary energy supply, the data we presented at the beginning of this section, in 2030 according to two different scenarios. The reference scenario (RS) is based on current energetic world policy, while the other takes into account a plausible climate policy post-2010 targeting 450 ppm CO_2-equivalent greehouse gases concentrations. Notice that in the reference scenario the total amount of energy needed is continuously increasing with the shares very similar to the ones in Fig. 1.1 since in actual policy, which is assumed to hold for the future too, the renewable increase rate is not greater than the conventional one. In the second scenario, instead, the most important fact to be noticed is the limitation of energy need (15 percent less than reference scenario) that would be achieved with the application of the regulations against energy waste of the international protocols. Moreover the progressive substitution of conventional sources with alternative ones would lead to a share greater than 20% for renewable energies.

1.2 Solar power

Solar radiation can be used to produce electrical and thermal energy and from this point of view the sun can be regarded as an inexhaustible source on the human time scale. In fact, since the incident radiation amounts to 125000 TW [69], it supplies to the Earth in just seven minutes the equivalent of the electricity used by the whole mankind in one year. The main technologies used to harvest this kind of energy are:

- **Concentrating solar power (CSP).** The working principle of this technology is to concentrate solar beams into a small area in order to produce high levels of heat that, depending on the target of the plant, can be used to boil water for direct utilization of for activating a turbine in an electric plant.

- **Photovoltaics (PV).** Photovoltaic solar cells convert sunlight into electricity by means of *photoelectric effect*, a phenomenon typical of metals and semimetals in which electrons are emitted as a consequence of absorption of energy from electromagnetic radiation of very short wavelength, such as visible or

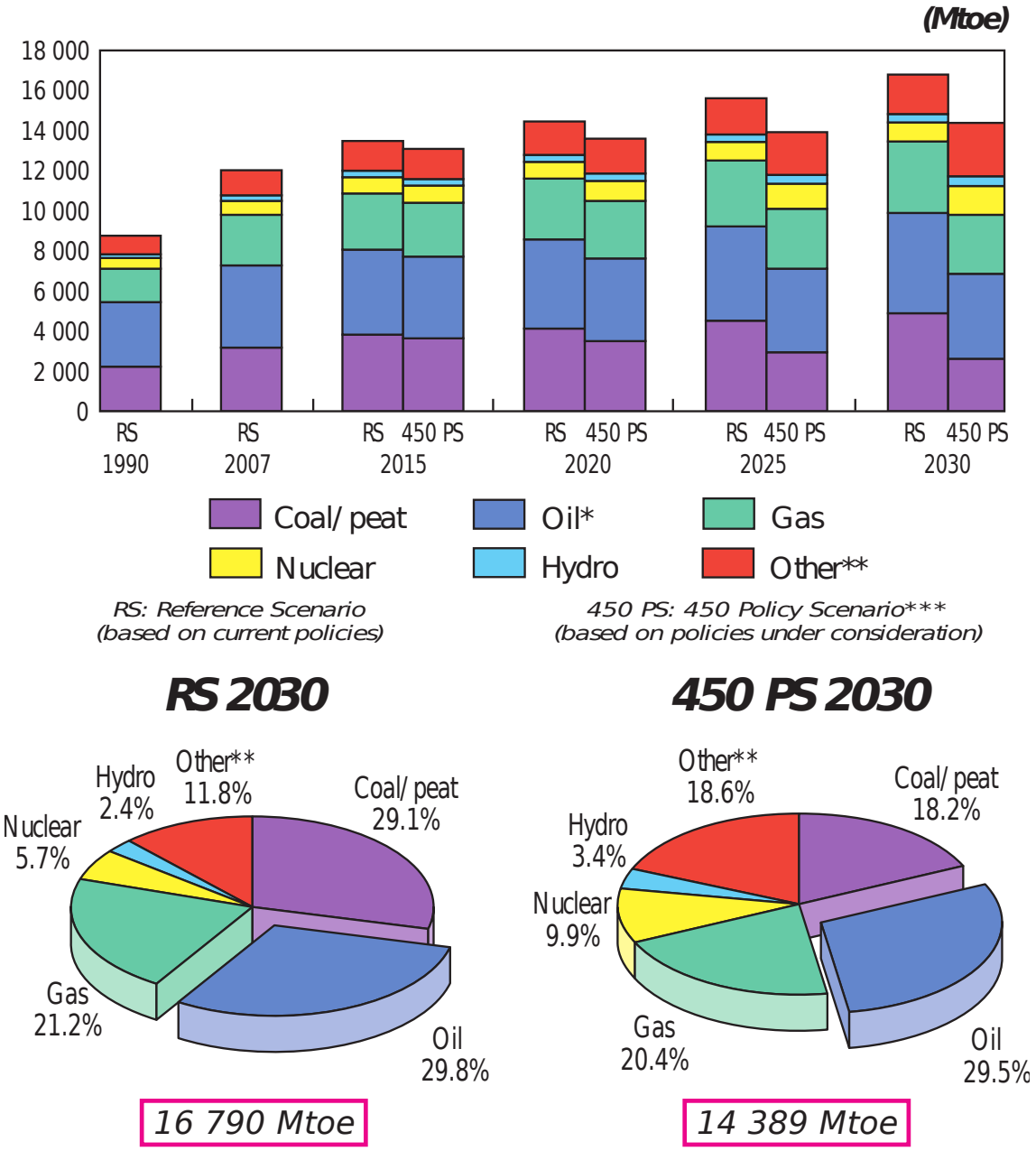

Figure 1.6: Forecast of fuel shares for world primary energy supply.

ultraviolet light. These devices have the unique characteristic of direct production of electricity, while all the other technologies used in this field need for an alternator to convert mechanical energy into electric one.

The concept of solar concentration has been applied to solar cells too (Concentrating photovoltaics) and recent devices couple the production of electricity and heat in the perspective of *cogeneration*.

We now present the two main types of solar plants for electricity production, highlighting their advantages and disadvantages.

1.2.1 Thermodynamic solar power plants

As we already reported, in this kind of plants light is focused from a large area to a small one using mostly systems of lenses or mirrors that follow the sun by means of tracking systems that adapt their orientation during the day hours. The main advantage for these plants is the fact that they utilize the turbine technology typical of conventional energy, which is cheap and reliable. A disadvantage is instead that to reach high production levels a plant has to be located in high irradiation areas which are often deserts and hence far from consumers and water, necessary for the operation of turbines. In addiction the size of the plant has to reach a minimum level required by the turbines to work at regime and for this reason their flexibility is limited.
Nowadays the most important markets for these facilities are US and Spain where between 2005 and the end of 2010 the capacity installed nearly doubled to reach 662 MW [28]. As obvious, the biggest plants are located in those nations and are respectively for the parabolic technology the Solar Energy Generating System (SEGS) in the Mojave Desert (California, US) with a capacity of 354 MW, and for solar towers the PS20 (Seville, Spain) with 20MW. Two pictures of these plants are shown in Fig. 1.7. A great expansion of the sector is forecast in the next years, under the

Figure 1.7: SEGS plant in the Mojave Desert, US and PS10 solar power tower in Andalusia, Spain.

impulse of the two international leader but also in other European countries and in North Africa and Middle East, where this technology has enormous potential. Storage technologies are also advancing, for example, two plants in Spain were built with a thermal energy storage systems, which allow continued power generation after sundown for a seven hours period [28].

1.2.2 Photovoltaic solar power plants

In the past decades photovoltaics were used mainly to produce electrical energy in areas not served by providers and the development of grid-connected systems of various dimension is quite recent, see Fig. 1.8. This kind of technology has two main

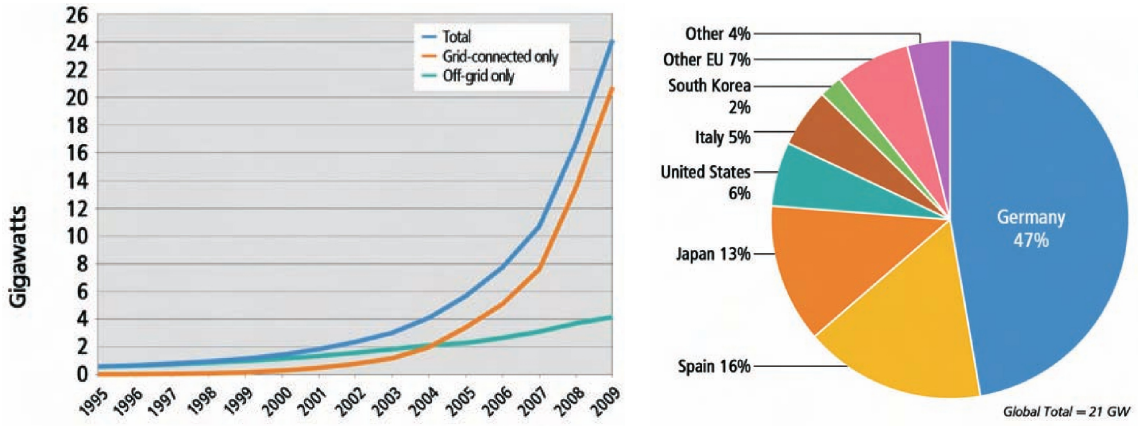

Figure 1.8: Solar PV existing world capacity and country shares.

advantages with respecto to CSP. First, no water is needed for electricity production, since the transformation of radiation energy into electric one is direct, and this greatly simplifies installation and integration of the systems. Secondly, there is no minimum or standard dimension for the plants and in this way they can easily be dimensioned in accordance with their specific requirements and needs. The most important defect of this technology is price and perhaps this, in addition to the aspects we mentioned previously, makes it more suitable for small applications rather than big energy plants. In any case the market for both small and large plants is constantly growing since cumulative global PV installations are now nearly six times than at the end of 2004 and analysts expect even higher growth in the next four to five years [28]. To convey the idea of the size of large plants, Fig. 1.9 reports the largest one which was built in germany in 2010 and has a capacity of 80.7 MW.
Germany is, in fact, the country that has first believed in photovoltaics giving great contribute in research and development for cost reduction and still it has almost half of the world total capacity. Many states are now following the German example with ambitious programs also boosted by feed-in tariffs directed to prompt privates to adopt this tecnhology.
As we said before, despite the average size of PV projects increases, there is growing interest in very small-scale, off-grid systems, particularly in developing countries. These systems account for only some 5 percent of the global market, but since in many remote areas the price of PV electricity is already at parity with fossil fuels they represent an important tool for development and improvement [28].

1.3 Solar cells

We already introduced solar cells and their working principles in a very basic way and we also described the recent sudden booming of their market. But at the same time we showed the fuel shares of primary energy sources and electricity sources in Fig. 1.1 and Fig. 1.2 and the renewable power capacities in Fig. 1.5 where the percentage of solar PV plays a marginal role in the total market of energy. What limits the diffusion of photovoltaic cells to this day, is the lack of competitiveness with respect to fossil fuels and other renewable source that can be synthesized by three main factors, namely cost, durability and efficiency.
Looking at the aspect of costs, in order to be convenient, a particular kind of photovoltaic solar cell has to produce electricity to a price similar, or at least close to be so, to the ones obtained from other sources, that it represented by the purchase price from the providers. This concept is known in the economical field as *grid parity* [36, 37]. Nowadays the grid parity for photovoltaics has been reached only in a few areas of the world in presence of very non common situations, such as in the Hawaii State, where both high irradiation and minor availability energy from conventional plants acted towards parity. In the rest of the world the achievement of grid parity is necessarily bounded to *incentives* and improvement of characteristics and performance by means of *research*.
Nevertheless, even though cost is the most important factor in determining the success of a photovoltaic technology, as we already stated product lifetime and efficiency play a role. A product succeeding in just two of these factors will only be suitable for niche applications.

Figure 1.9: Finsterwalde Solar Park, Germany.

The effort of scientific research during the last decades then focused on these three aspects to improve cell performance and many paths were explored, bringing to a series of devices that can be grouped into three main *generations* that we will now briefly describe.

1.3.1 First generation solar cells

When addressing to *first generation* solar cells, one refers to devices with a the original silicon-based technology that nowadays hold a share of about 84 percent on the global market, see Fig. 1.10. It is possible to further divide these cells in two groups,

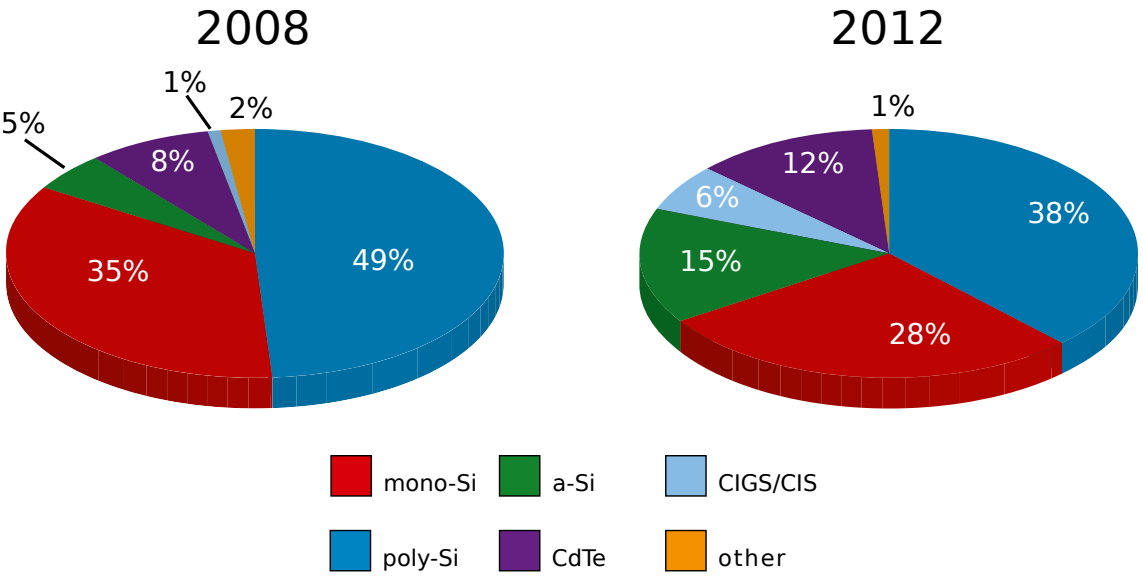

Figure 1.10: Market shares of photovoltaic technologies in 2008 and forecast for 2012.

differing in the production process.

Monocrystalline silicon cells are produced with an expensive and complex procedure in which a very pure crystal is obtained and cut in slices. After that its surfaces are doped to enhance charge separation and treated for preventing reflexes and permit current harvesting. These cells are characterized by very high efficiency (14-17%) and long durability but their price is very high.

Poly- or **multicrystalline silicon** cells are obtained with the same procedure as monocrystalline ones but in place of pure silicon, electronic production scraps are used instead. These cells have a characteristic striped surface and lower efficiency than mono-Si cells (12-14%) but this comes with a cheaper price. Durability and performance maintaining are still high.

In Fig. 1.11 the appearance of these two kinds of cells is compared and the higher purity of monocrystalline ones is clear.

Producers estimate that mono-Si and poly-Si solar cells will reach efficiencies of

respectively 20 and 18 percent by 2020, and hence very close to the theoretical limit of 31% [79], with a consistent decrease of production costs but even in those situations, materials will have high impact on the final price. For this reason new approaches were attempted for finding alternatives to replace crystalline silicon in the production of solar cells.

1.3.2 Second generation solar cells

The family of *second generation* solar cells is based on the *thin film* technology and it possible to distinguish three main groups depending on the materials used in the films.

Amorphous silicon (a-Si) solar cells are produced with the technique of vapor deposition of a thin (1-2 μm) layer of silicon on a flexible grass or plastic substrate. These cells have a efficiency of about 8%, but they experience a sudden decrease in such a parameter after the first period of operation.

Cadmium telluride (CdTe) solar cells replace silicon with cadmium telluride which has a lager absorption spectra and hence a potentially higher efficiency. Cadmium would be toxic if released but its percentage of the total weight is very low and the compound used is very stable and non soluble. Registered efficiencies are between 10 and 11 percent.

Copper indium gallium selenide (CIGS/CIS) solar cells use several ternary compounds that present crystal lattices suited for charge transport. Their efficiency is about 11% and cost reduction is expected in the future.

These devices, despite having lower efficiency, exhibit several advantages with respect to silicon based solar cells. First of all, the very small thickness of the layers allow to save a great quantity of material and hence lower the final cost. Secondly,

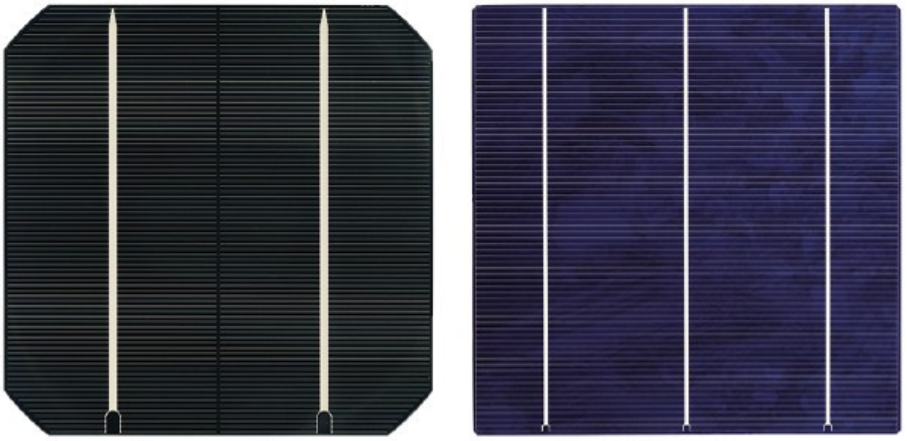

Figure 1.11: Comparison between mono- and polycrystalline solar cells.

with thin film technology it is possible to integrate on a flexible substrate the production of more than one cell in a unique step, process that is not feasible in the case of silicon cells. From an industrial point of view this could lead to automated continuous processes instead of batch ones with consequent lower unitary prices. In addiction, flexibility and transparency are very important aspects for architectural integrability, also in consideration of the rapid expansion of *Building Integrated Photovoltaics*, see Section 1.3.4. Finally, these devices have better performances at high temperatures and, as a consequence of disordered interior structure, in presence of diffuse light. An example of this kind of cells is reported in Fig. 1.12.

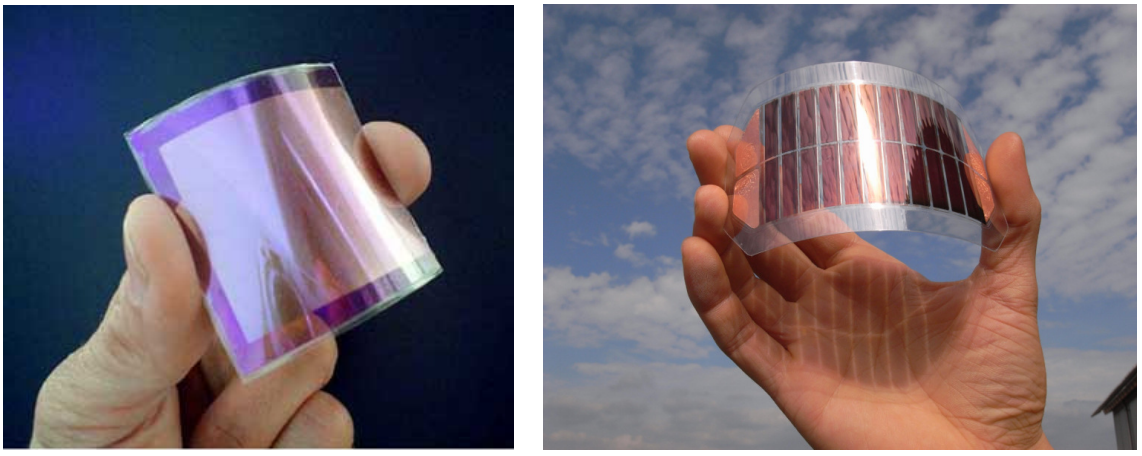

Figure 1.12: Thin film and organic solar cell. They share flexibility and transparency properties.

Even if these devices represent a hot topic for researchers, there are several industrial products on the market and their cumulative share amounted to 14% in 2008, see Fig. 1.10. According to [37] this technology could experience a rapid success, reaching a percentage of 33% by 2012, with a-Si and CdTe cells leading with respectively 15 and 12%.

1.3.3 Third generation solar cells

Third generation solar cells family groups together a various number of technological attempts, whose common denominator is the use of semiconducting organic materials. Carbon is the base element of these latter and since it has the same outer electric configuration as silicon, they share some properties. Three main groups can be signed out, differing in the working principles and the measures in which carbon compounds are used.

Dye sensitized solar cells (DSSC) are electrochemical solar cells in which absorption of light occurs by means of dye molecules bounded to a substrate of TiO_2. A

fundamental role is played by some negative ions free to move into a liquid phase that are involved in photon absorption and are regenerated at one of the electrodes.
Organic solar cells (OSC) embrace all the devices in which the photoactive part is made of organic material, usually two different polymers, with several possibilities for internal morphology.
Hybrid solar cells are very close to OSCs since working principles and device structure are in common but one organic material is replaced by an inorganic one. These devices can be manufactured as thin film cells of flexible and low cost substrates (see Fig. 1.12) but in addition organic polymers are mostly soluble and for this reason make viable the exploitation of very cheap industrial processes like ink-jet printing, radically decreasing the costs. Moreover, the advantages we reported for thin film cells still hold for OSCs. Anyway, it is important to highlight that by now there are no commercial products based on these technologies and prototypes are still confined in the laboratories. It is possible to estimate in 3 to 5 years the period before their availability on the market and the expected prices are interestingly low.

1.3.4 Other recent technologies and applications

Recently it has been proposed to use the concept of light concentration, proper of solar thermodynamic, on photovoltaic cells too, in order to reduce the quantity of materials needed and as a consequence the cost. This particular technology is called **Concentrating Photovoltaic** (CPV) and concentrating systems can be based on mirrors (reflection), lens (refraction) or light guides, see Fig. 1.13. Since a great amount of light is concentrated in a small spot, high efficiency solar cells like silicon ones are commonly used since they give much better results in absorption. A negative feature of these devices is their poor architectural integrability due to the presence itself of the optical system.

Over the last years the attention of the operators of the sector focused on an another technology, **Building Integrated Photovoltais** (BIPV) that consists in substituting conventional materials with photovoltaic ones in the production of architectural elements. These devices have then to ensure both electrical production and structural performances, as thermal insulation, wind and rain resistance and rigidity. This concept has not to be confused with *Building Applied Photovoltaics* (BAPV), which is the traditional system of placement of photovoltaic modules on the already existent structures.

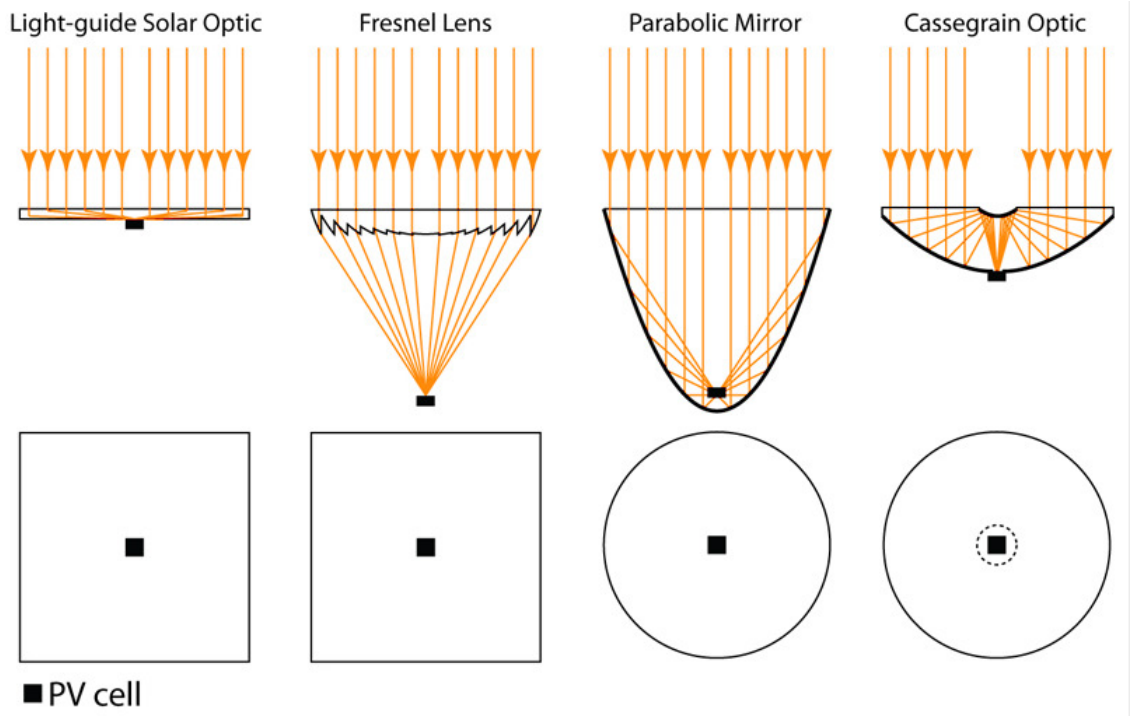

Figure 1.13: Concentrating systems in PVC devices.

Chapter 2

Dye sensitized solar cells

2.1 Historical background

The first recorded observation of a photoelectrochemical phenomenon was made by Henry Becquerel [8] in 1839, who noted the photocurrent and photovoltage produced by illumination of a silver chloride-coated platinum electrode in various electrolytes. His research was motivated by the first photographic images made by Daguerre in 1837 and by Fox Talbot's studies made in 1839 on halide process, although the art of emulsion became a science only with the theoretical analysis of the process by Gurney and Mott [39] in 1938. Initially, films were insensitive to mid-spectrum and red-light, because the semiconductor energy diagram of the silver halide grains has a band gap ranging between from 2.7 to 3.2 electron volts (eV). In 1883 Vogel discovered that silver halide emulsion could be sensitized by adding a dye, which extended the photosensitivity to longer wavelengths [76]. The concept of dye enhancement was carried over by Moser [55] from photography to photoelectrochemical cells using different dyes on silver halide electrodes. However, the clear recognition of the parallels between the two procedures, photography and photoelectrochemical, is dated only to the 1960s, when Gerischer and Tributsch [33] discovered that the same dyes could be used in both systems. It was also recognized that the dye should be absorbed on the semiconductor electrodes in a closely packed monolayer for maximum efficiency [56]. The concept of using dispersed particles to provide a sufficient interface area then emerged, and was employed for the photoelectrodes.
After 1970 the interest in photoelectrochemical cells increased; in particular, research was carried out on dye photophysics, electrolyte redox chemistry and on morphology of semiconductors, until the announcement in 1991 by Graetzel and co-workers of the construction of a sensitised electrochemical photovoltaic device with efficiency of 7.1% under solar illumination [60]. That evolution has continued progressively since then, with certified efficiencies over 11% by now.

2.2 Photoelectrochemical cells

A photoelectrochemical cell (PEC), is a device which generates electrical energy or hydrogen from solar light, in a process similar to the electrolysis of water. Basic components are a semiconducting photoanode and a cathode immersed in an electrolyte. The main feature of this type of cell is the junction between a semiconductor and an electrolyte. In most cases the electrolyte is a liquid.
Over the last years, research has focused on two types of PECs, illustrated in Fig. 2.1. The first type is the regenerative cell, which converts light into electric power leaving no net chemical change behind. Photons of energy exceeding that of the band gap generate electron-hole pairs, which are separated by the electron field present in the space charge layer between semiconductor and electrolyte. The negative charge carriers move through the semiconductor to the current collector and the external circuit. The positive holes are driven to the surface where they are collected and removed by the reduced form of the redox relay molecule, indicated in figure with R, oxidizing it: $h^+ + R \rightarrow O$. The oxidized form O is reduced back to R by the electrons that re-enter in the cell through the counter electrode, from the external circuit.
The second type, denoted photosynthetic cells, are inspired to the natural photosynthesis. The operation is similar to the first type except that there are two redox systems: one reacting with the holes on the surface of the semiconductor and the second reacting with the electrons entering the counter-electrode. In the example shown in Fig 2.1(b), we can observe a cell that generates a chemical fuel, in particular hydrogen, through the photo-cleavage of water. In this case water is oxidized to oxygen at the semiconductor surface (anode) and reduced to hydrogen at the cathode.
Titanium dioxide (TiO_2) is the most used semiconductor in PECs, although it has a large band gap and absorbs only the ultraviolet part of solar emission. This limitation implies a low efficiency of the cell, because the semiconductor is insensible to the visible spectrum. The problem was resolved by the separation of the optical absorption and charge generation phenomena, using an electron transfer sensitizer absorbing in the visible spectrum to inject charge carriers across the semiconductor-electrolyte junction into a substrate with a wide band gap. The addition of a dye on the semiconductor surface led to the birth of a new type of cell that is called dye-sensitized solar cell (DSSC) or Grätzel Cell. We can say that DSSCs operate and consist of materials different of a common solar cell, but with the same scope convert solar energy into electricity. To understand how a DSSC works, we compare it with a standard silicon solar cell, or p/n cell, and emphasize what are the main difference and similarities between them. The main difference with respect to a conventional

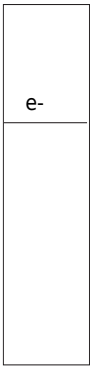

Figure 2.1: Operation of photoelectrochemical cells. **a**. Regenerative type cell producing electric current from sunlight; **b**. cell that generates a chemical fuel, hydrogen.

p/n cell are the following:

- light absorption occurs in the semiconductor, this leads to photogeneration of electrons directly in the semiconductor;
- in the semiconductor minority and majority carriers are present. In the n-type silicon layer, the free electrons are called majority carriers whereas the holes are called minority carriers. Conversely, in the p-type silicon layer, electrons are termed minority carriers and holes are termed majority carriers;
- charge separation is driven by the electric field in the space charge region. The electrical field is formed at the interface between the n-doped and p-doped semiconductor;
- the photovoltage is equal to the reduction of the built-in electric potential;
- the semiconductor surface must be free of impurities and grain.

The only important feature shared by the two types of cells is that the recombination rate at and near the photovoltaically active junction should be minimized to maximize the efficiency of the cells.
The summary of the difference of the two devices leads to the question how such a DSSC can work at all as a photovoltaic cell. This will become clear from the following section.

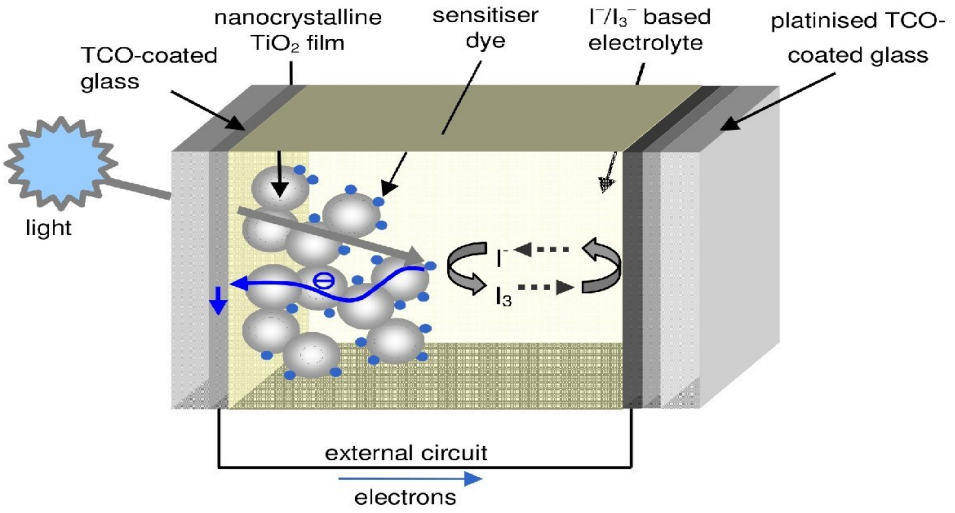

Figure 2.2: Diagram of a liquid electrolyte dye-sensitised solar cell.

2.3 Operating principle of the DSSC

A DSSC consists of four main components: a nanoporous semiconductor coated with a dye, an electrolyte and two transparent conducting electrodes. The device can be constructed using different combinations of materials choosing among a set of them that are known to facilitate the motion of charges within the device. In our work we address the most conventional configuration, which consists of a layer of nanoparticles of TiO_2, a N3-ruthenium (Ru) dye complex and an iodide/triiodide (I^-/I_3^-) electrolyte system. The diagram of a DSSC and its operating principle are shown in Fig. 2.2. The manufacture of the cell is performed through several steps. The first step is the preparation of TiO_2 by hydrolysis, which is subsequently treated to increase the porosity of its surface. Then, the semiconductor is deposed onto a glass plate which is coated with a layer of a transparent conductive oxide (TCO), for example SnO_2. The thickness of the TiO_2 is about 10 μm and its nanoporous structure leads to a surface area increased by a factor of one thousand compared to a smooth surface. Characteristic values for porosity are 50% and 65% [34]. The large internal surface area of the film is coated with a monolayer of dye capable of charge transfer that in the case we consider is ruthenium (Ru) dye complex, by soaking the nanoporous film in dye solution until the desired coverage is achieved. The dyed nanoporous film constitutes the DSSC anode. After, this operation the TiO_2 is flooded with the electrolyte, which consists of a redox couple solution, in present case made of iodide (I^-) and triiodide (I_3^-). The counter electrode is formed by sandwiching the semiconductor-dye-electrolyte between the existing transparent conducting electrode (TCE) and another TCO coated glass plate. The counter elec-

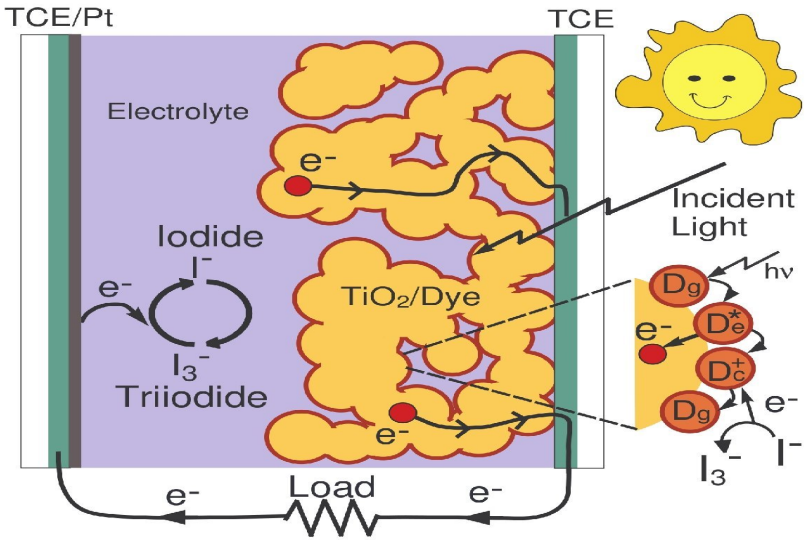

Figure 2.3: Schematic operating system. Photoexcitation of the sensitizer dye is followed by electron injection into the conduction band of the mesoporous semiconductor, and electron transport through the metal oxide film to the TCO-coated glass working electrode. The dye molecule is regenerated by the redox system, which is itself regenerated at the platinised counter electrode by electrons passing through the external circuit.

trode adjacent to the electrolyte is covered by platinum, which acts as a catalyst for the redox reaction between electrolyte and the TCO.

During operation, the solar cell is illuminated bye the side of the electrode contact with the semiconductor, which acts as a collector for the current of electrons the current collector, as shown in Fig. 2.3. The photons hitting the cell are absorbed by the molecules D_g of the dye, which are excited to a new state, D_e^*:

$$D_g + h\nu \rightarrow D_e^*.$$

The excited molecules inject electrons at high rate (0.1 ps) into the conduction band of the semiconductor, and they are oxidized to cation state, D_c^+. The electrons in the TiO_2 diffuse through the solid to the glass electrode and out of the cell. Then, they then reach the counter electrode, after passing through the external circuit where a load is placed. Here they reduce the redox species via the following reaction:

$$I_3^- + 2e^- \rightarrow 3I^-.$$

Ions I^- are transported through the electrolyte and in contact with the oxidized dye

molecules they react, bringing back the dye to the initial state or ground state D_g:

$$D_c^+ + e^- \rightarrow D_g.$$

Due to the energy level positioning in the system, the cell is capable of producing voltage between its electrodes and across the external load. The maximum theoretical value for the photovoltage at open circuit condition is determined by the potential difference between the conduction band of the TiO_2 an the redox potential of the electrolyte [15]. The operation of the cell is regenerative in nature, since no chemical substance are neither consumed nor produced during the working cycle.

2.4 Detailed analysis of chemical reactions

We now analyze in detail the reactions that occur at the interfaces between electrolyte-counter electrode, electrolyte-dye and electrolyte-semiconductor.
At regime operation, under irradiation, at the platinized counter electrode the return of electrons in the device occurs via the reaction

$$2e^-(Pt) + I_3^- \rightarrow 3I^-, \tag{2.1}$$

where e^-(Pt) is an electron from the platinum electrode where the metal acts as a catalyst. I^- ions diffuse through the solution reaching the semiconductor, and reduce the oxidised dye molecules via the electron returning reaction

$$2D_c^+ + 3I^- \rightarrow 2D_g + I_3^-. \tag{2.2}$$

It is clear from reactions (2.1) and (2.2) that I_3^- ions are consumed at the counter electrode and produced at the TiO_2.
The surface of the semiconductor may not be fully covered by the dye, so there may be locations where electrolyte and semiconductor are in direct contact. This produces a loss mechanism within the DSSC, in particular a net oxidation-reduction reaction, where an electron in the conduction band of the TiO_2 reduces the I_3^-, namely

$$I_3^- + 2e^-(TiO_2) \rightleftharpoons 3I^-. \tag{2.3}$$

The reduction reaction of the I_3^- ions is still under investigation, and several theories have been proposed in literature. A first possible scheme that describes in more detail the reaction (2.3) that occurs at the interface between electrolyte and semiconductor is a two electron reaction [24]:

$$2I^\bullet \rightleftharpoons 2I + 2e^-$$

$$2I \rightleftharpoons I_2 \tag{2.4}$$

$$I + I_2 \rightleftharpoons I_3^-, \tag{2.5}$$

where $I^\bullet$ is an intermediate species. The chemical reactions (2.4) and (2.4) are fast and are assumed to be in equilibrium [24].
An alternative scheme is based on the introduction of an intermediate species, the anion radical $I_2^{\bullet -}$. This species appears in the electron returning reaction (2.2) and in the oxidation-reduction reaction (2.3). In [42] the following scheme of reactions is proposed for the net reaction given in (2.3) at the back electrode and at the semiconductor-electrolyte interface:

$$I_3^- \rightleftharpoons I_- + I_2$$

$$e^- + I_2 \rightarrow I_2^{\bullet -}$$

$$2I_2^{\bullet -} \rightarrow I_3^- + I^-$$

This pattern of chemical reactions can be expanded as shown in [7]:

$$D_c^+ + 2I^- \rightarrow D_g + I_2^{\bullet -}$$

$$2I_2^{\bullet -} \rightarrow I_3^- + I^- \tag{2.6}$$

$$I_2^{\bullet -} + e^- \rightarrow 2I^- \tag{2.7}$$

$$I_3^- + e^- \rightarrow I_2^{\bullet -} + I^-.$$

The lifetime of the radical ion is very short and this is due to the high rate of the reactions (2.6) and (2.4).
The introduction of the intermediate species has led to further studies, in particular on the reactions at the interface between dye and semiconductor. In relation to this problem the following reaction system was proposed [26]:

$$D_c^+ + I^- \rightarrow D_g + I^\bullet$$

$$I^\bullet + I^- \rightarrow I_2^{\bullet -}$$

$$2I^\bullet \rightarrow I_3^- + I^-.$$

Transport of these charged species within the electrolyte depends on the solvent used and also on the tortuous nature of the film. We conclude from the above presentation that the interactions of the electrolyte species at the interfaces within the DSSC are not well understood and their mathematical characterization is still under scrutiny; for this reason, we will model them in a simplified manner in the following section.

2.5 Electrode transport in the semiconductor

As we previously said, electron transport occurs in the TiO_2 electrode and we now address the its features.
The semiconductor nanoparticle network works not only as a large surface area substrate for the dye molecules but also as a transport media for the electrons injected from the excited dye. The nanoporous structure of the electrode can be viewed as a network of individual particles through which electrons percolate by hopping from one particle to the next. Measurements indicate that diffusion of electrons is characterized by a distribution of diffusion coefficients, which have been related to the hopping of electrons via surface traps of different depths. These electron traps are localized at energy states just below the conduction band edge of the TiO_2 and they play a significant role in the electron transport. Trapping of electrons at the TiO_2 surface may be a pathway for recombination, resulting in photocurrent losses and therefore photovoltage losses, due to kinetic reasons.
The diffusion coefficient of electrons depends on the light intensity. At low light intensity only deep traps participate in the electron transport determining a low diffusion coefficients. Increasing the intensity, deep traps are filled at steady state condition, while shallow traps contribute to the electron motion, resulting in a larger diffusion coefficient [40].
Understanding the transport of electrons in the electrode in DSSC is very important for the further development of the device, especially to increase the efficiency of the cell.

2.6 Kinetics of operations

We said that the main difference between DSSC and a conventional p/n junction solar cell is the existence of a dye monolayer between semiconductor and electrolyte. This configuration does not require excitation in the bulk semiconductor to drive charge separation. Though this may be an advantage, there are many loss mechanisms in DSSCs caused by the porous nature of the semiconductor and the high contact area between it and the electrolyte. The electrons that are formed after separation from the dye have a high probability of recombining at the electrolyte-dye-TiO_2 interface. This probability is influenced not only by the contact surface, but also by the rate of the chemical reactions. Within the device, it is desirable to have very fast rates for the ones that contribute to charge movement in the desired direction and to have limited or slow rates for reaction that contribute to losses.
Another loss mechanism that occurs in the cell is due to the incomplete coverage of the surface of the semiconductor by the dye. The current generated by these inac-

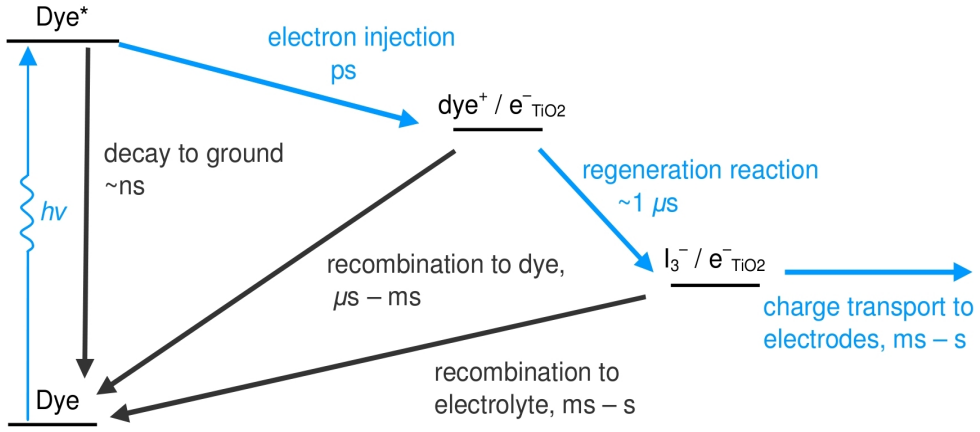

Figure 2.4: State diagram representation of the kinetics of DSSC function. Forward processes are indicated by blue arrows. The competing loss pathways are shown in grey.

curacies is called dark current, which may be opposite to the operating current of the cell. The cell efficiency increases if the value of dark current is as low as possible [72].

Figure 2.4 is a photochemical view of the working principle of a DSSC, illustrating the sequence of electron transfer and charge-transport processes which result in photocurrent flow. This figure also illustrates several competing loss pathways, shown as blue arrows. These latter include decay of the dye from excited to ground state and charge recombination of injected electrons with dye cations and with the redox couple. Efficient electron injection requires the rate of electron injection to exceed the rate of decay of the dye excited state which is in the range 10^7 - 10^{10} s^{-1}. The rate of electron injection depends on the electronic coupling between the dye excited-state LUMO orbital and accepting states in the TiO_2, and on the relative energetics of these states. Electron injection rates larger than 10^{12} s^- have been reported for a range of sensitizer dyes, consistent with efficient electron injection [22]. However it should be noted that fast electron injection dynamics requires both strong electronic coupling of the dye LUMO orbital to the metal oxide conduction-band states, and a sufficient free energy difference to drive the reaction. As such, electron-injection dynamics are dependent on the energetics of the TiO_2 conduction band, and therefore on the concentration of potential-determining ions (e.g. Li+) in the electrolyte. Omission of such ions from the electrolyte can result in an insufficient energetic driving force, reducing the quantum yield of charge injection, and thereby reducing device photocurrent.

Efficient dye regeneration requires the rate of re-reduction of the dye cation by the redox couple to exceed that of charge recombination of injected electrons with these dye cations. This recombination reaction has been shown to be strongly dependent on the electron density in the TiO_2 electrode and therefore on the light intensity and cell voltage. The regeneration reaction is dependent on the iodide concentration, electrolyte viscosity and dye structure. For the commonly used sensitizer dye, and employing a low-viscosity electrolyte, the regeneration reaction has a half-time of about 1μs, sufficiently fast to compete effectively with the recombination reaction and ensuring that the regeneration reaction can be achieved with unit quantum efficiency [35].
Efficient charge collection by the external circuit requires the time constant for electron transport within the TiO2 matrix to be faster than charge recombination of injected electrons with the redox couple. Electron transport is a diffusive process, strongly influenced by electron trapping in localised sub-bandgap states, resulting in the dynamics being strongly dependent on position of the TiO2 electron Fermi level. Typical electron-transport times under solar irradiation are of the order of milliseconds [63],[30].
Given the relatively slow timescale for charge transport in DSSCs compared with most other photovoltaic devices, and the extensive interfacial area available for charge recombination in the device (due to its mesoscopic structure), it is remarkable that the quantum efficiency of charge collection can approach unity. The key factor enabling this high efficiency is the slow rate constant for the interfacial charge recombination of injected electrons with the oxidised redox couple. This reaction is a multi-electron reaction, most simply being described by (2.3) or (2.1). The intermediate states of the mechanism of this reaction have been extensively studied 2.4, and while the details remain somewhat controversial, it is apparent that without a catalyst as platinum at the counter electrode, one or more of the intermediates steps exhibits a significant activation barrier, resulting in a slow overall rate constant for this reaction. The low rate constant for this recombination reaction on TiO_2 is a key factor behind the remarkable efficiencies achieved to date for DSSCs. Nevertheless, reaction (2.3) is the primary recombination pathway in DSSCs. The flux of this recombination pathway increases with increasing electron density in the semiconductor electrode.
The kinetics competition between charge transport and recombination in DSSC can be analysed in terms of effective carrier diffusion length L_e, given by

$$L_e = \sqrt{D_{eff}\tau} \tag{2.8}$$

where D_{eff} is the effective electron diffusion length, and τ is the electron lifetime due to the charge-recombination reaction given by reaction (2.3) [63]. The diffusion

length increases with light intensity, due to the increased electron density in the TiO_2 film, whilst τ shows a proportional decrease, resulting in a value for L_e that is almost independent of light intensity. Typical values for L_e are 5-20 μm.
It is important to emphasise that the energetics and kinetics of DSSC may not be considered interdependently. The kinetics of the interfacial electron-transfer dynamics strongly depend on the energetics of the TiO_2/dye/electrolyte interface and on the density of electrons in the TiO_2. Raising the energy of the TiO_2 conduction band reduces recombination losses, and therefore may give a high cell output voltage, but at the expense of a lower free energy driving force for charge separation, which may result in a lower quantum efficiency for charge generation and therefore a lower output current. In practice, modulation of this energetics and kinetics to achieve optimum device performance remains one of the key challenges in DSSC research and development.

2.7 Mathematical models for DSSCs

We will now present the mathematical models of the physical phenomena, described so far. These phenomena are quite complex because there are many parameters, interfacial reactions and chemical species to be taken into account complicating the formulation of a mathematical model that can describe the device at best.
Over the last decade, several papers concerning with the mathematical simulation of transport and physical phenomena in DSSCs have been published which provide valuable insight into the functioning of the cell. We can divide the numerical models into three groups. The first group includes models that do not consider neither electron transport in the TiO_2 network nor the back reaction between electrons and the electrolyte at the cathode [61]. These simplified models are used to explore the influence of various parameters on the device operation but also allow to compute the optimal iodide and triiodide concentrations in the cell electrolyte. In fact, the main effect that can be studied with them is mass transport of the ionic species present between the electrodes in the liquid either in the pores of the mesoporous material or in the bulk.
The second group of models include the electron transport and the possibility to study the dependency on time of the various phenomena. As a matter of fact, if the model is time dependent, the electrons transport through the semiconductor is affected by the trapping/detrapping effect, that improves the simulation result but, at the same time, complicates the numerical solution. In any case, if trapping/detrapping effect is accounted for, the the simulation includes only electron transport [48].
In this way the result of the simulation will be the density distribution of the species at the end of transition [25], [9].
The last group of model studies the semiconductor-dye-interface representation of each interfacial charge injection and recombination reaction within the DSSC [62]. This type of model is very complex, but it allows an accurate comparison with experimental data, in particular to understand the kinetics reaction.

In our work, we analyse the first two types of models: in particular, we study a modified model proposed by Grätzel and co-workers [61] and a model that includes electron transport. All these models will be considered in stationary conditions.

2.7.1 Mass transport model for a DSSC

The model proposed in this section is an improvement of the model presented in [61]. We are interested in the steady state operation of the device and we want to

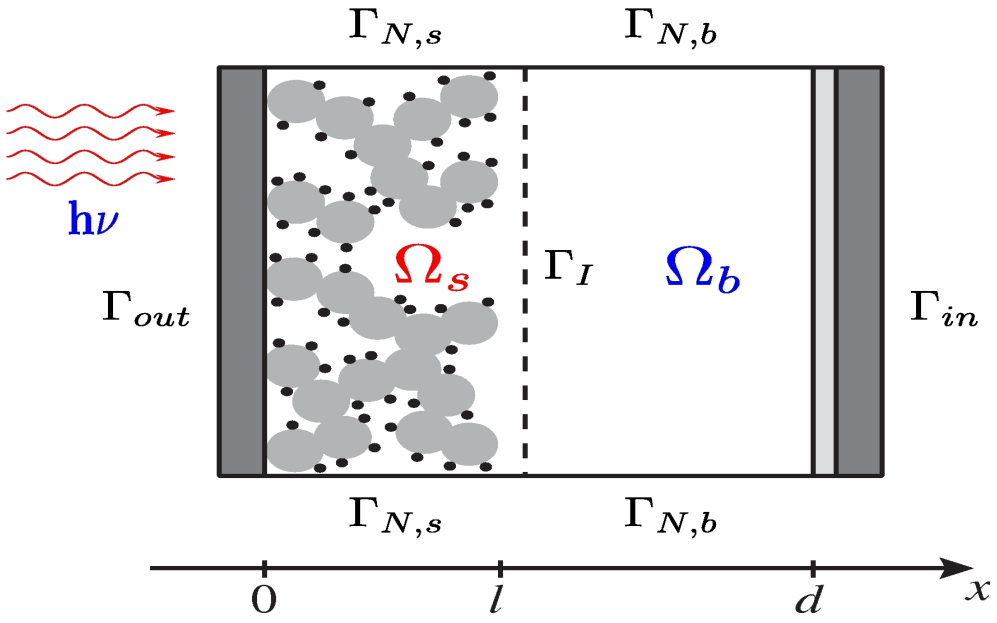

Figure 2.5: Schematic representation of the domain of the model for a dye-sensitised solar cell.

investigate the mass transport within the cell. The parameters that influence mass transport are various and the most important ones are the thickness the cell and its liquid bulk layer, but also species diffusion coefficients, the light irradiation and the ion migration play an important role.
We assume the same simplifications as in the model proposed in [61], in particular:

- the cell is irradiated perpendicularly to its electrodes;
- under open-circuit operation, no successful injection takes place;
- electrons are produced by illuminating the region of the device where the dyed-TiO_2 is present;
- the I_3^- production and I^- the consumption rate are proportional to the number of photons absorbed for unit time at any location;
- the influence of TCO, TCE and glass are neglected.

The cross-section of the device is schematically depicted in Fig. 2.5. The domain $\Omega \equiv \Omega_s \cup \Omega_b$ representing respectively a section of the cell is divided in two subregions: Ω_s where the dyed-TiO_2 nanoporous layer is mixed uniformly with the electrolyte and Ω_b where there is only the bulk electrolyte layer. The boundary of the domain, $\Gamma \equiv \partial\Omega$, is divided in four subregions Γ_I, Γ_{out}, Γ_{in} and Γ_N, representing the interface between the two subregion, the anode, the cathode and interior artificial boundaries respectively. The subregions connected with anode and cathode are

indicated with Γ_{out} and Γ_{in} because at Γ_{out} the electrons leave the cell, while at Γ_{in} they enter back into the device.
With n_{I^-} and $n_{I_3^-}$ we indicate the negatively charged carrier densities (ionic fraction per volume (m^{-3})) while with n_C we denote positively charged carrier density (cations). We refer to $n_{i,s}$ and $n_{i,b}$ for the restrictions respectively on Ω_s and Ω_b. In other works instead, such as in [61], the ionic concentrations in the electrolyte (mM) are considered.
Considering first Ω_s, taking into account the stechiometric coefficients of the reactions (2.2) and (2.3), the densities of the redox ions and cations obey to:

$$\begin{cases} -\dfrac{1}{q}\operatorname{div}\mathbf{J}_{I^-,s} = \dfrac{3}{2}G \\ -\dfrac{1}{q}\operatorname{div}\mathbf{J}_{I_3^-,s} = -\dfrac{1}{2}G \qquad \text{in } \Omega_s, \\ \dfrac{1}{q}\operatorname{div}\mathbf{J}_{C,s} = 0 \end{cases} \tag{2.9}$$

In the system (2.9) $\mathbf{J}_{I^-,s}$, $\mathbf{J}_{I_3^-,s}$ and $\mathbf{J}_{C,s}$ denote the iodide, triiodie and cation charge flux densities respectively, while G is the generation term, that is the number of electrons successfully injected in the TiO_2 per unit of time and volume. It is related to the current, I, that flows out of the cell, via:

$$G = \frac{I}{q\eta l_s}, \tag{2.10}$$

where q is the value of the elementary charge, l_s the thickness of the semiconductor layer and η the TiO_2 porosity. From this relation, we can observe an important aspect of this unusual electronic device model: the current that flows out of the device is an *input parameter* and not, as usually happens in the design of an electronic circuit, an output computed quantity.
The drift-diffusion model is used for the charge density fluxes:

$$\begin{cases} \mathbf{J}_{I^-,s} = qD_{I^-,s}\nabla n_{I^-,s} - q\mu_{I^-}n_{I^-,s}\nabla\varphi_s \\ \mathbf{J}_{I_3^-,s} = qD_{I_3^-,s}\nabla n_{I_3^-,s} - q\mu_{I_3^-}n_{I_3^-,s}\nabla\varphi_s \qquad \text{in } \Omega_s, \\ \mathbf{J}_{C,s} = -qD_{C,s}\nabla n_{C,s} - q\mu_C n_{C,s}\nabla\varphi_s \end{cases} \tag{2.11}$$

where the parameters $D_{i,s}$ and $\mu_{i,s}$ are the charge carrier diffusion coefficients and the carrier mobilities respectively, while φ is the electric potential. The relation between the diffusion coefficient and the mobility for each species can be described through the Einstein relation

$$D_{i,s} = \mu_{i,s}V_{TH}, \tag{2.12}$$

where V_{TH} is the thermal voltage, defined as $V_{TH} = K_B T/q$, K_B being the Boltzmann constant and T the absolute temperature. The electric potential φ is assumed to satisfy Poisson equation

$$-\operatorname{div}(\varepsilon_0 \varepsilon_{r,s} \nabla \varphi_s) = q(n_{C,s} - n_{I^-,s} - n_{I_3^-,s}) \quad \text{in} \quad \Omega_s, \tag{2.13}$$

where ε_0 is the vacuum permittivity and $\varepsilon_{r,s}$ is relative dielectric constant for the mixture of dyed-TiO_2 and electrolyte.
Next, we consider the equations in Ω_b. In this region there is only the bulk liquid, then the continuity equations for the carriers are expressed as follows:

$$\begin{cases} -\dfrac{1}{q} \operatorname{div} \mathbf{J}_{I^-,b} = 0 \\ -\dfrac{1}{q} \operatorname{div} \mathbf{J}_{I_3^-,b} = 0 \qquad \text{in } \Omega_b. \\ \dfrac{1}{q} \operatorname{div} \mathbf{J}_{C,b} = 0 \end{cases} \tag{2.14}$$

We observe that the continuity equations for to the cations that appear in both systems (2.9) and (2.14) are homogeneous, then we can conclude that this species is not involved in charge transfer. As in Ω_s, the charge flux densities $\mathbf{J}_{i,b}$ are assumed to obey the Drift-Diffusion model:

$$\begin{cases} \mathbf{J}_{I^-,b} = qD_{I^-,b} \nabla n_{I^-,b} - q\mu_{I^-} n_{I^-,b} \nabla \varphi_b \\ \mathbf{J}_{I_3^-,b} = qD_{I_3^-,b} \nabla n_{I_3^-,b} - q\mu_{I_3^-} n_{I_3^-,b} \nabla \varphi_b \qquad \text{in } \Omega_b. \\ \mathbf{J}_{C,b} = -qD_{C,b} \nabla n_{C,b} - q\mu_C n_{C,b} \nabla \varphi_b \end{cases} \tag{2.15}$$

Again, the ionic diffusion coefficient $D_{i,b}$ and the ionic mobility $\mu_{i,b}$ are mutually related via the Einstein relation:

$$D_{i,b} = \mu_{i,b} V_{TH}. \tag{2.16}$$

and for the electric potential φ the following Poisson equation holds:

$$-\operatorname{div}(\varepsilon_0 \varepsilon_{r,b} \nabla \varphi_b) = q(n_{C,b} - n_{I^-,b} - n_{I_3^-,b}) \quad \text{in} \quad \Omega_b, \tag{2.17}$$

where $\varepsilon_{r,b}$ is the relative dielectric constant for the bulk liquid in Ω_b.
To close the model, we need to specify the boundary conditions and the interfacial conditions on Γ_I. We start introducing the boundary conditions for the continuity equation (2.9) defined in Ω_s and we observe that at the anode, Γ_{out}, there are no chemical reactions that involve the three species, so the net fluxes related with them

are null and we can impose the following Neumann conditions:

$$\begin{aligned} &\mathbf{J}_{I^-,s} \cdot \boldsymbol{\nu} = 0 \\ &\mathbf{J}_{I_3^-,s} \cdot \boldsymbol{\nu} = 0 \quad \text{on } \Gamma_{out}, \\ &\mathbf{J}_{C,s} \cdot \boldsymbol{\nu} = 0 \end{aligned} \tag{2.18}$$

where $\boldsymbol{\nu}$ is the outward normal unit vector along the boundary Γ. On $\Gamma_{N,s}$ and $\Gamma_{N,b}$, we impose Neumann homogeneous conditions, because these boundaries are artificial boundaries where symmetry conditions hold. At the interface of the two regions, we need to apply two condition for each species. The first condition is the continuity of the carrier flux densities, while in the second condition we impose that the ionic densities change discontinuously at the interface according to the porosity of the TiO_2, that is:

$$\begin{aligned} &\mathbf{J}_{I^-,s} \cdot \boldsymbol{\nu} = \mathbf{J}_{I^-,b} \cdot \boldsymbol{\nu} \\ &\mathbf{J}_{I_3^-,s} \cdot \boldsymbol{\nu} = \mathbf{J}_{I_3^-,b} \cdot \boldsymbol{\nu} \quad \text{on } \Gamma_I, \\ &\mathbf{J}_{C,s} \cdot \boldsymbol{\nu} = \mathbf{J}_{C,b} \cdot \boldsymbol{\nu} \end{aligned} \tag{2.19}$$

$$\begin{aligned} &n_{I_s^-} = \eta \cdot n_{I_b^-} \\ &n_{I_{3,s}^-} = \eta \cdot n_{I_{3,b}^-} \quad \text{on } \Gamma_I, \\ &n_{C_s} = \eta \cdot n_{C_b} \end{aligned} \tag{2.20}$$

For the continuity equations (2.14), we have to impose the boundary condition on the cathode, Γ_{in}, where electrons enter back into the cell. At the cathode reaction (2.1) takes places and in particular triiodides are consumed and the iodides are produced by the re-entered electrons. Again, taking into consideration the steichiometric parameters, the following Neumann condition holds on Γ_{in}

$$\begin{aligned} &\mathbf{J}_{I^-,b} \cdot \boldsymbol{\nu} = \frac{3}{2} J_{ext} \\ &\mathbf{J}_{I_3^-,b} \cdot \boldsymbol{\nu} = -\frac{1}{2} J_{ext} \quad \text{on } \Gamma_{in}, \\ &\mathbf{J}_{C,b} \cdot \boldsymbol{\nu} = 0 \end{aligned} \tag{2.21}$$

where J_{ext} is the flux of electrons that flow out of the device, that we already said to be an input parameter.

The only charge that flows out of the device is that of electrons, so that for the other ionic species within the cell the conservation of the initial mass must hold. This fact is expressed in mathematical terms with the following integral conditions, stating that the total number of the ionic species within the cell does not change:

$$\begin{aligned}
&\int_{\Omega_s} n_{I^-,s}(\mathbf{x})d\mathbf{x} + \int_{\Omega_b} n_{I^-,b}(\mathbf{x})d\mathbf{x} = n^0_{I^-,s}|\Omega_s| + n^0_{I^-,b}|\Omega_b| \\
&\int_{\Omega_s} n_{I_3^-,s}(\mathbf{x})d\mathbf{x} + \int_{\Omega_b} n_{I_3^-,b}(\mathbf{x})d\mathbf{x} = n^0_{I_3^-,s}|\Omega_s| + n^0_{I_3^-,b}|\Omega_b| \\
&\int_{\Omega_s} n_{C,s}(\mathbf{x})d\mathbf{x} + \int_{\Omega_b} n_{C,b}(\mathbf{x})d\mathbf{x} = n^0_{C,s}|\Omega_s| + n^0_{C,b}|\Omega_b|
\end{aligned} \tag{2.22}$$

$n^0_{i,s}$ and $n^0_{i,b}$ being the initial densities of the species called also dark densities. Finally, the boundary conditions for the two Poisson equations are:

$$\begin{aligned}
&\varepsilon_0\,\varepsilon_{r,s}\nabla\varphi_s\cdot\boldsymbol{\nu} = 0 && \text{on}\Gamma_{out} \\
&\varepsilon_0\,\varepsilon_{r,s}\nabla\varphi_s\cdot\boldsymbol{\nu} = 0 && \text{on}\Gamma_{N,s} \\
&\varphi_b = 0 && \text{on}\Gamma_{in} \\
&\varepsilon_0\,\varepsilon_{r,b}\nabla\varphi_b\cdot\boldsymbol{\nu} = 0 && \text{on}\Gamma_{N,b}
\end{aligned} \tag{2.23}$$

while the interfacial conditions on Γ_I are

$$\begin{aligned}
&\varphi_s = \varphi_b \\
&\varepsilon_0\varepsilon_{r,s}\,\nabla\varphi_s\cdot\,\boldsymbol{\nu} = \varepsilon_0\varepsilon_{r,b}\,\nabla\varphi_b\cdot\,\boldsymbol{\nu}
\end{aligned} \qquad \text{on } \Gamma_I. \tag{2.24}$$

Since the potential is known up to a constant, we are allowed to set it equal to zero at one of the boundaries.
Summarizing the model described in this section, the subproblems that have to be solved are:

Iodide subproblem

$$\begin{cases}
-\text{div}\left(\mu_{I^-,s}V_{TH}\nabla n_{I^-,s} - \mu_{I^-,s}\,n_{I^-,s}\nabla\varphi_s\right) = \dfrac{3}{2}\,G & \text{in } \Omega_s \\
-\text{div}\left(\mu_{I^-,b}V_{TH}\nabla n_{I^-,b} - \mu_{I^-,b}\,n_{I^-,b}\nabla\varphi_b\right) = 0 & \text{in } \Omega_b \\
\left(\mu_{I^-,s}V_{TH}\nabla n_{I^-,s} - \mu_{I^-,s}\,n_{I^-,s}\nabla\varphi_s\right)\cdot\boldsymbol{\nu} = 0 & \text{on } \Gamma_{out}\cup\Gamma_{N,s} \\
\left(\mu_{I^-,b}V_{TH}\nabla n_{I^-,b} - \mu_{I^-,b}\,n_{I^-,b}\nabla\varphi_b\right)\cdot\boldsymbol{\nu} = \dfrac{3}{2}J_{ext} & \text{on } \Gamma_{in} \\
\left(\mu_{I^-,b}V_{TH}\nabla n_{I^-,b} - \mu_{I^-,b}\,n_{I^-,b}\nabla\varphi_s\right)\cdot\boldsymbol{\nu} = 0 & \text{on } \Gamma_{N,b} \\
\mathbf{J}_{I^-,s}\cdot\boldsymbol{\nu} = \mathbf{J}_{I^-,b}\cdot\boldsymbol{\nu} & \text{on } \Gamma_I \\
n_{I_s^-} = \eta\cdot n_{I_b^-} & \text{on } \Gamma_I
\end{cases} \tag{2.25}$$

Triiodide subproblem

$$\begin{cases} -\mathrm{div}\left(\mu_{I_3^-,s} V_{TH} \nabla n_{I_3^-,s} - \mu_{I_3^-,s}\, n_{I_3^-,s} \nabla \varphi_s\right) = -\dfrac{1}{2} G & \text{in } \Omega_s \\ -\mathrm{div}\left(\mu_{I_3^-,b} V_{TH} \nabla n_{I_3^-,b} - \mu_{I_3^-,b}\, n_{I_3^-,b} \nabla \varphi_s\right) = 0 & \text{in } \Omega_b \\ \left(\mu_{I_3^-,s} V_{TH} \nabla n_{I_3^-,s} - \mu_{I_3^-,s}\, n_{I_3^-,s} \nabla \varphi_s\right) \cdot \boldsymbol{\nu} = 0 & \text{on } \Gamma_{out} \cup \Gamma_{N,s} \\ \left(\mu_{I_3^-,b} V_{TH} \nabla n_{I_3^-,b} - \mu_{I_3^-,b}\, n_{I_3^-,b} \nabla \varphi_b\right) \cdot \boldsymbol{\nu} = -\dfrac{1}{2} J_{ext} & \text{on } \Gamma_{in} \\ \left(\mu_{I_3^-,b} V_{TH} \nabla n_{I_3^-,b} - \mu_{I_3^-,b}\, n_{I_3^-,b} \nabla \varphi_b\right) \cdot \boldsymbol{\nu} = 0 & \text{on } \Gamma_{N,b} \\ \mathbf{J}_{I_3^-,s} \cdot \boldsymbol{\nu_s} = \mathbf{J}_{I_3^-,b} \cdot \boldsymbol{\nu_b} & \text{on } \Gamma_I \\ n_{I_{s,3}^-} = \eta \cdot n_{I_{3,b}^-} & \text{on } \Gamma_I \end{cases} \tag{2.26}$$

Cation subproblem

$$\begin{cases} -\mathrm{div}\left(\mu_{C,s} V_{TH} \nabla n_{C,s} + \mu_{C,s}\, n_{C,s} \nabla \varphi_s\right) = 0 & \text{in } \Omega_s \\ -\mathrm{div}\left(\mu_{C,b} V_{TH} \nabla n_{C,b} + \mu_{C,b}\, n_{C,b} \nabla \varphi_s\right) = 0 & \text{in } \Omega_b \\ \left(\mu_{C,s} V_{TH} \nabla n_{C,s} + \mu_{C,s}\, n_{C,s} \nabla \varphi_s\right) \cdot \boldsymbol{\nu_s} = 0 & \text{on } \Gamma_{out} \cup \Gamma_{N,s} \\ \left(\mu_{C,b} V_{TH} \nabla n_{C,b} + \mu_{C,b}\, n_{C,b} \nabla \varphi_b\right) \cdot \boldsymbol{\nu_b} = 0 & \text{on } \Gamma_{in} \cup \Gamma_{N,b} \\ \mathbf{J}_{C,s} \cdot \boldsymbol{\nu_s} = \mathbf{J}_{C,b} \cdot \boldsymbol{\nu_b} & \text{on } \Gamma_I \\ n_{C_s} = \eta \cdot n_{C_b} & \text{on } \Gamma_I \end{cases} \tag{2.27}$$

Electric potential subproblem

$$\begin{cases} -\mathrm{div}\left(\varepsilon_0 \varepsilon_{r,s} \nabla \varphi_s\right) = q(n_{C,s} - n_{I_-,s} - n_{I_-^3,s}) & \text{in } \Omega_s \\ -\mathrm{div}\left(\varepsilon_0 \varepsilon_{r,b} \nabla \varphi_b\right) = q(n_{C,b} - n_{I_-,b} - n_{I_-^3,b}) & \text{in } \Omega_b \\ \varepsilon_0\, \varepsilon_{r,s} \nabla \varphi_s \cdot \boldsymbol{\nu_s} = 0 & \text{on } \Gamma_{out}, \\ \varepsilon_0\, \varepsilon_{r,s} \nabla \varphi_s \cdot \boldsymbol{\nu_s} = 0 & \text{on } \Gamma_{N,s}, \\ \varphi_b = 0 & \text{on } \Gamma_{in}, \\ \varepsilon_0\, \varepsilon_{r,b} \nabla \varphi_b \cdot \boldsymbol{\nu_b} = 0 & \text{on } \Gamma_{N,b}, \end{cases} \tag{2.28}$$

Integral conditions

$$\begin{aligned}
\int_{\Omega_s} n_{I^-,s}(\mathbf{x})d\mathbf{x} + \int_{\Omega_b} n_{I^-,b}(\mathbf{x})d\mathbf{x} &= n^0_{I^-,s}|\Omega_s| + n^0_{I^-,b}|\Omega_b| \\
\int_{\Omega_s} n_{I_3^-,s}(\mathbf{x})d\mathbf{x} + \int_{\Omega_b} n_{I_3^-,b}(\mathbf{x})d\mathbf{x} &= n^0_{I_3^-,s}|\Omega_s| + n^0_{I_3^-,b}|\Omega_b| \\
\int_{\Omega_s} n_{C,s}(\mathbf{x})d\mathbf{x} + \int_{\Omega_b} n_{C,b}(\mathbf{x})d\mathbf{x} &= n^0_{C,s}|\Omega_s| + n^0_{C,b}|\Omega_b|
\end{aligned} \tag{2.29}$$

2.7.2 Electron transport model for a DSSC

In the previous section we introduced a mass transport model for DSSC, which does not include the treatment of the electron transport in the semiconductor electrode. Now, we present a model in which both motion of the photo-generated electrons and ionic species are considered. Cations provide the charge neutrality to the electrolyte, nevertheless they are not involved in the charge transport process in the device. In comparison with the system of the equations (2.25)–(2.29), we have to add a continuity equation, with the electron density flux once again modeled by Drift Diffusion model and two new terms for electron generation and recombination. In addition, the integral conditions, related to the iodide and triiodide species, need to be changed since instead of mass conservation we have to consider the stoichiometric balances of the redox reactions.

We divide the structure of the DSSC in the same way as in the previous section and we use the same notation for the domain, the boundary and the ionic species densities. In addition, we introduce the electron densities n_e and the charge carrier density $\mathbf{J}_e$.

The first important equation that we introduce is the continuity equation for conduction band electrons

$$-\frac{1}{q}\operatorname{div}\mathbf{J}_e = G(\mathbf{x}) - R \quad \text{in} \quad \Omega_s, \tag{2.30}$$

where $G(\mathbf{x})$ and $R(\mathbf{x})$ denoting respectively photo generation and recombination by the back-reaction (2.3) of electrons. There are many ways to model the generation term. A first approach is based on an optical model of the device, which leads to very accurate results, see [75], but we do not consider it in our work. A simpler way is to use a generation term of the following form

$$G(\mathbf{x}) = \int_{\lambda_{min}}^{\lambda_{max}} \alpha(\lambda)\,\Phi(\lambda)\,e^{-\alpha(\lambda)x}\,d\lambda. \tag{2.31}$$

In this relation, α denotes the absorption coefficient, Φ is the spectral incident photon flux density, λ_{min} and λ_{max} are the wavelengths that limit the absorption band of the DSSC.
We assume that only electrons from the conduction band can recombine with the triiodide in the electrolyte (see reaction (2.3)). We also assume that recombination is linearly dependent on the electron density, so that we can write the relative term as [26]

$$R(\mathbf{x}) = k_e(n_e(\mathbf{x}) - n_e^0) \tag{2.32}$$

Here, k_e denotes electron relaxation rate constant and n_e^0 is the initial electron concentration in the nanoporous layer. We also consider another more complex model recombination, which includes nonlinear dependence on iodides and triodides densities this model reads [10]

$$R(\mathbf{x}) = k_e \left\{ n_e \sqrt{\frac{n_{I_3^-,s}}{n_{I^-,s}}} - n_e^0 \sqrt{\frac{n^0_{I_3^-,s}}{(n^0_{I^-,s})^3}}\, n_{I^-,s} \right\}. \tag{2.33}$$

As in previous section we use the Drift-Diffusion equation to model for the carrier flux densities and in particular for electrons it reads

$$\mathbf{J}_e = qD_e\nabla n_e - q\mu_e n_e \nabla\varphi \tag{2.34}$$

where D_e is electron diffusion coefficient in the TiO_2, depending on the porosity of the semiconductor. According to [57] for porosity values such that $P \in [0.41, 0.7]$ we have

$$D_e = \beta|P - P_c|^\mu \tag{2.35}$$

with the critical porosity P_c set as 0.76, the power law exponent, μ=0.82, and β is a constant equal to $4 \cdot 10^{-8}$ $\mathrm{m^{-1}s^{-1}}$. For porosity values, $P < 0.41$, the electron diffusion coefficient is calculated with:

$$D_e = 1.69 \cdot 10^{-8}(-17.48P^3 + 7.39P^2 - 2.89P + 2.15). \tag{2.36}$$

In our model we simply assume in a more classical way that Einstein relation hold for the diffusion coefficient, that is:

$$D_e = \mu_e V_{TH}. \tag{2.37}$$

The continuity equation and the drift-diffusion model for the other three ionic species

are the same as in the previous section, except for the right-hand side term of the ones relative to iodides and triodides, since the contributions due to the recombination reaction have to be added. For completeness we report the continuity equations for iodides, triiodides and cations in Ω_s:

$$\begin{cases} -\dfrac{1}{q}\mathrm{div}\,\mathbf{J}_{I^-,s} = \dfrac{3}{2}(G-R) \\ -\dfrac{1}{q}\mathrm{div}\,\mathbf{J}_{I_3^-,s} = -\dfrac{1}{2}(G-R) \qquad \text{in } \Omega_s, \\ \dfrac{1}{q}\mathrm{div}\,\mathbf{J}_{C,s} = 0 \end{cases} \tag{2.38}$$

where G is given by (2.31) and R is given by one of the two relations (2.32) or (2.33). In Ω_b we can write the following equations for the three ionic species:

$$\begin{cases} -\dfrac{1}{q}, \mathrm{div}\,\mathbf{J}_{I^-,b} = 0 \\ -\dfrac{1}{q}, \mathrm{div}\,\mathbf{J}_{I_3^-,b} = 0 \qquad \text{in } \Omega_b. \\ \dfrac{1}{q}\mathrm{div}\,\mathbf{J}_{C,b} = 0 \end{cases} \tag{2.39}$$

The Drift-Diffusion relations for the iodide, triiodide and cations in the two region are given by (2.11) in Ω_s and (2.15) in Ω_b respectively.
The electric potential φ is coupled with ionic densities by means of the Poisson equation, the only modification with respect to the previous section being on the right hand side for the subdomain Ω_s, where n_e ho to be added:

$$-\,\mathrm{div}\,(\varepsilon_0\varepsilon_{r,s}\nabla\varphi) = q(n_{C,s} - n_{I^-,s} - n_{I_3^-,s} - n_e) \quad \text{in} \quad \Omega_s, \tag{2.40}$$

while in the liquid bulk we still have

$$-\,\mathrm{div}\,(\varepsilon_0\varepsilon_{r,b}\nabla\varphi) = q(n_{C,b} - n_{I^-,b} - n_{I_3^-,b}) \quad \text{in} \quad \Omega_b. \tag{2.41}$$

Finally we introduce the boundary conditions needed to close the problem. For electrons we impose:

$$n_e = N_c \exp\left(-\frac{\varphi_{bar}}{V_{TH}}\right) \quad \text{on } \Gamma_{out} \tag{2.42}$$

$$\mathbf{J_e}\cdot\boldsymbol{\nu_s} = 0 \quad \text{on } \Gamma_I \tag{2.43}$$

$$\mathbf{J_e}\cdot\boldsymbol{\nu_s} = 0 \quad \text{on } \Gamma_{N,s} \tag{2.44}$$

Here N_c is the conduction band density of states, while φ_{bar} is the thermionic emission injection barrier height for electrons at the anode. The first condition (2.42) is a

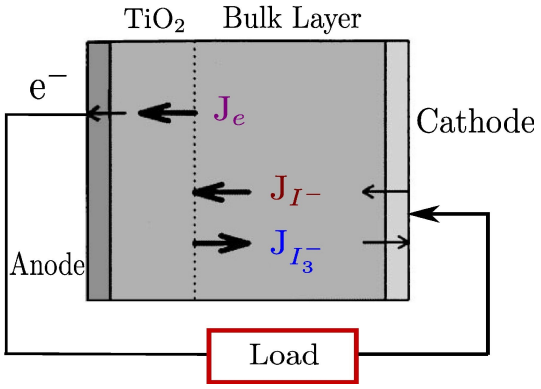

Figure 2.6: Schematic representation of the fluxes within the DSSC

typical result of the assumption of ohmic behavior of the semiconductor TCO glass interface, while (2.44) takes into account the fact that electrons cannot flow in the region where there is only the liquid bulk.

For the boundary conditions of the continuity equation (2.38) defined in Ω_s, we observe that at the anode, Γ_{out}, there are no chemical reactions that involve the three species, so the net relative fluxes are null and we can impose the following Neumann conditions:

$$\begin{aligned} \mathbf{J}_{I^-,s} \cdot \boldsymbol{\nu}_s &= 0 \\ \mathbf{J}_{I_3^-,s} \cdot \boldsymbol{\nu}_s &= 0 \quad \text{on } \Gamma_{out}. \\ \mathbf{J}_{C,s} \cdot \boldsymbol{\nu}_s &= 0 \end{aligned} \tag{2.45}$$

For each ionic species it necessary to consider two conditions on the interface. As before, the first one is given by the continuity of the charge flux densities and the second takes into account that the ionic densities change discontinuously at the interface according to the porosity of the TiO_2. The conditions for the fluxes on Γ_I are then:

$$\begin{aligned} \mathbf{J}_{I^-,s} \cdot \boldsymbol{\nu} &= \mathbf{J}_{I^-,b} \cdot \boldsymbol{\nu} \\ \mathbf{J}_{I_3^-,s} \cdot \boldsymbol{\nu} &= \mathbf{J}_{I_3^-,b} \cdot \boldsymbol{\nu} \quad \text{on } \Gamma_I, \\ \mathbf{J}_{C,s} \cdot \boldsymbol{\nu} &= \mathbf{J}_{C,s} \cdot \boldsymbol{\nu} \end{aligned} \tag{2.46}$$

while the conditions for the discontinuity of the ionic charges on Γ_I read

$$\begin{aligned} n_{I_s^-} &= \eta \cdot n_{I_b^-} \\ n_{I_{3,s}^-} &= \eta \cdot n_{I_{3,b}^-} \quad \text{on } \Gamma_I, \\ n_{C_s} &= \eta \cdot n_{C_b} \end{aligned} \tag{2.47}$$

At stationary regime a current J_e defined by

$$J_e = \frac{1}{|\Gamma_{out}|} \int_{\Gamma_{out}} \mathbf{J}_e \cdot \boldsymbol{\nu},$$

flows out of the anode and reaches the cathode through the external circuit. Here reaction (2.1) takes place resulting in net fluxes for iodides and triiodides that linearly dependent on J_e with parameters equal to the stoichiometric coefficient. We then impose the following boundary conditions on Γ_{in}:

$$\begin{aligned} &\mathbf{J}_{I^-,b} \cdot \boldsymbol{\nu}_b = \frac{3}{2} J_e \\ &\mathbf{J}_{I_3^-,b} \cdot \boldsymbol{\nu}_b = -\frac{1}{2} J_e \quad \text{on } \Gamma_{in}. \\ &\mathbf{J}_{C,b} \cdot \boldsymbol{\nu}_b = 0 \end{aligned} \tag{2.48}$$

The last relation meaning as usual that cations are confined in the cell.
The first charge conservation condition expresses the fact that the total number of cations within the cell does not change with respect to the configuration in the dark

$$\int_{\Omega_s} n_{C,s}(\mathbf{x}) d\mathbf{x} + \int_{\Omega_b} n_{C,b}(\mathbf{x}) d\mathbf{x} = n^0_{C,s}|\Omega_s| + n^0_{C,b}|\Omega_b|. \tag{2.49}$$

The second boundary condition we consider is the conservation of the total number of iodine atoms. Taking into account that triodides have three atoms instead of iodides that are composed by just one, the condition reads:

$$\begin{aligned} &\int_{\Omega_s} (n_{I_3^-,s}(\mathbf{x}) + 1/3 n_{I^-,s}(\mathbf{x})) d\mathbf{x} + \\ &\int_{\Omega_b} (n_{I_3^-,b}(\mathbf{x}) + 1/3 n_{I^-,b}(\mathbf{x})) d\mathbf{x} = (n^0_{I_3^-,s} + 1/3 n^0_{I^-,s})|\Omega_s| + (n^0_{I_3^-,b} + 1/3 n^0_{I^-,b})|\Omega_b|. \end{aligned} \tag{2.50}$$

The third integral condition describes the balance between electrons and iodides resulting from reactions (2.1). In this reaction every three iodide ions two conduction band electrons, are generated so we can impose that

$$\begin{aligned} &\int_{\Omega_s} (1/2 n_e(\mathbf{x}) + 1/3 n_{I^-,s}(\mathbf{x})) d\mathbf{x} + \\ &\int_{\Omega_b} (1/3 n_{I^-,b}(\mathbf{x})) d\mathbf{x} = (1/2 n^0_e + 1/3 n^0_{I^-})|\Omega_s| + 1/3 n^0_{I_3^-,b}|\Omega_b|. \end{aligned} \tag{2.51}$$

Finally the boundary conditions and interfacial conditions for the two Poisson equation are the same as in the previous section, namely, relations (2.23) and (2.24).
Again we summarise the model,dividing it into subproblems.

Electron subproblem

$$\begin{cases} -\mathrm{div}\left(\mu_e V_{TH}\nabla n_e - \mu_e\, n_e \nabla\varphi_s\right) = G - R & \text{in } \Omega_s \\ n_e(\mathbf{x}) = N_c \exp\left(-\dfrac{\varphi_{bar}}{V_{TH}}\right) & \text{on } \Gamma_{out} \\ \left(\mu_e V_{TH}\nabla n_e - \mu_e\, n_e \nabla\varphi_s\right)\cdot \boldsymbol{\nu_s} = J_e & \text{on } \Gamma_{out} \\ \left(\mu_e V_{TH}\nabla n_e - \mu_e\, n_e \nabla\varphi_s\right)\cdot \boldsymbol{\nu_s} = 0 & \text{on } \Gamma_{in}\cup\Gamma_{N,s} \end{cases} \tag{2.52}$$

Iodide subproblem

$$\begin{cases} -\mathrm{div}\left(\mu_{I^-,s} V_{TH}\nabla n_{I^-,s} - \mu_{I^-,s}\, n_{I^-,s} \nabla\varphi_s\right) = \dfrac{3}{2}(G - R) & \text{in } \Omega_s \\ -\mathrm{div}\left(\mu_{I^-,b} V_{TH}\nabla n_{I^-,b} - \mu_{I^-,b}\, n_{I^-,b} \nabla\varphi_b\right) = 0 & \text{in } \Omega_b \\ \left(\mu_{I^-,s} V_{TH}\nabla n_{I^-,s} - \mu_{I^-,s}\, n_{I^-,s} \nabla\varphi_s\right)\cdot \boldsymbol{\nu} = 0 & \text{on } \Gamma_{out}\cup\Gamma_{N,s} \\ \left(\mu_{I^-,b} V_{TH}\nabla n_{I^-,b} - \mu_{I^-,b}\, n_{I^-,b} \nabla\varphi_b\right)\cdot \boldsymbol{\nu} = \dfrac{3}{2} J_e & \text{on } \Gamma_{in} \\ \left(\mu_{I^-,b} V_{TH}\nabla n_{I^-,b} - \mu_{I^-,b}\, n_{I^-,b} \nabla\varphi_b\right)\cdot \boldsymbol{\nu} = 0 & \text{on } \Gamma_{N,b} \\ \mathbf{J}_{I^-,s}\cdot \boldsymbol{\nu_n} = \mathbf{J}_{I^-,b}\cdot \boldsymbol{\nu_b} & \text{on } \Gamma_I \\ n_{I_s^-} = \eta \cdot n_{I_b^-} & \text{on } \Gamma_I \end{cases} \tag{2.53}$$

Triiodide subproblem

$$\begin{cases} -\mathrm{div}\left(\mu_{I_3^-,s} V_{TH}\nabla n_{I_3^-,s} - \mu_{I_3^-,s}\, n_{I_3^-,s} \nabla\varphi_s\right) = -\dfrac{1}{2}(G - R) & \text{in } \Omega_s \\ -\mathrm{div}\left(\mu_{I_3^-,b} V_{TH}\nabla n_{I_3^-,b} - \mu_{I_3^-,b}\, n_{I_3^-,b} \nabla\varphi_b\right) = 0 & \text{in } \Omega_b \\ \left(\mu_{I_3^-,s} V_{TH}\nabla n_{I_3^-,s} - \mu_{I_3^-,s}\, n_{I_3^-,s} \nabla\varphi_s\right)\cdot \boldsymbol{\nu} = 0 & \text{on } \Gamma_{out}\cup\Gamma_{N,s} \\ \left(\mu_{I_3^-,b} V_{TH}\nabla n_{I_3^-,b} - \mu_{I_3^-,b}\, n_{I_3^-,b} \nabla\varphi_b\right)\cdot \boldsymbol{\nu} = -\dfrac{1}{2} J_e & \text{on } \Gamma_{in} \\ \left(\mu_{I_3^-,b} V_{TH}\nabla n_{I_3^-,b} - \mu_{I_3^-,b}\, n_{I_3^-,b} \nabla\varphi_b\right)\cdot \boldsymbol{\nu} = 0 & \text{on } \Gamma_{N,b} \\ \mathbf{J}_{I_3^-,s}\cdot \boldsymbol{\nu_s} = \mathbf{J}_{I_3^-,b}\cdot \boldsymbol{\nu_b} & \text{on } \Gamma_I \\ n_{I_{s,3}^-} = \eta \cdot n_{I_{3,b}^-} & \text{on } \Gamma_I \end{cases} \tag{2.54}$$

Cation subproblem

$$\begin{cases} -\text{div}\left(\mu_{C,s} V_{TH} \nabla n_{C,s} + \mu_{C,s}\, n_{C,s} \nabla \varphi_s\right) = 0 & \text{in } \Omega_s \\ -\text{div}\left(\mu_{C,b} V_{TH} \nabla n_{C,b} + \mu_{C,b}\, n_{C,b} \nabla \varphi_b\right) = 0 & \text{in } \Omega_b \\ \left(\mu_{C,s} V_{TH} \nabla n_{C,s} + \mu_{C,s}\, n_{C,s} \nabla \varphi_s\right) \cdot \boldsymbol{\nu_s} = 0 & \text{on } \Gamma_{out} \cup \Gamma_{N,s} \\ \left(\mu_{C,b} V_{TH} \nabla n_{C,b} + \mu_{C,b}\, n_{C,b} \nabla \varphi_b\right) \cdot \boldsymbol{\nu_b} = 0 & \text{on } \Gamma_{in} \cup \Gamma_{N,b} \\ \mathbf{J}_{C,s} \cdot \boldsymbol{\nu_s} = \mathbf{J}_{C,b} \cdot \boldsymbol{\nu_b} & \text{on } \Gamma_I \\ n_{C_s} = \eta \cdot n_{C_b} & \text{on } \Gamma_I \end{cases} \tag{2.55}$$

Electric potential subproblem

$$\begin{cases} -\text{div}\left(\varepsilon_0 \varepsilon_{r,s} \nabla \varphi_s\right) = q(n_{C,s} - n_{I_-,s} - n_{I_-^3,s}) & \text{in } \Omega_s \\ -\text{div}\left(\varepsilon_0 \varepsilon_{r,b} \nabla \varphi_b\right) = q(n_{C,b} - n_{I_-,b} - n_{I_-^3,b}) & \text{in } \Omega_b \\ \varepsilon_0\, \varepsilon_{r,s} \nabla \varphi_s \cdot \boldsymbol{\nu} = 0 & \text{on } \Gamma_{out} \\ \varepsilon_0\, \varepsilon_{r,s} \nabla \varphi_s \cdot \boldsymbol{\nu} = 0 & \text{on } \Gamma_{N,s} \\ \varphi_b = 0 & \text{on } \Gamma_{in} \\ \varepsilon_0\, \varepsilon_{r,b} \nabla \varphi_b \cdot \boldsymbol{\nu} = 0 & \text{on } \Gamma_{N,b} \end{cases} \tag{2.56}$$

Integral conditions

$$\begin{aligned} &\int_{\Omega_s} (n_{I_3^-,s}(\mathbf{x}) + 1/3 n_{I_3^-,s}(\mathbf{x}))d\mathbf{x} + \\ &\int_{\Omega_b} (n_{I_3^-,b}(\mathbf{x}) + 1/3 n_{I_3^-,b}(\mathbf{x}))d\mathbf{x} = (n^0_{I_3^-,s} + 1/3 n^0_{I_3^-,s})|\Omega_s| + (n^0_{I_3^-,b} + 1/3 n^0_{I_3^-,b})|\Omega_b| \\ &\int_{\Omega_s} (1/2 n_e(\mathbf{x}) + 1/3 n_{I^-,s}(\mathbf{x}))d\mathbf{x} + \int_{\Omega_b} (1/3 n_{I^-,b}(\mathbf{x}))d\mathbf{x} = (n^0_e + 1/3 n^0_{I^-})|\Omega_s| + 1/3 n^0_{I_3^-,b}|\Omega_b| \\ &\int_{\Omega_s} n_{C,s}(\mathbf{x})d\mathbf{x} + \int_{\Omega_b} n_{C,b}(\mathbf{x})d\mathbf{x} = n^0_{C,s}|\Omega_s| + n^0_{C,b}|\Omega_b| \end{aligned} \tag{2.57}$$

Chapter 3

Organic solar cells

This chapter is devoted to the second type of solar cells we considered in our work, namely organic solar cells (OSC). What makes OSCs different from the devices described in the previous chapter is that the photo-active layer is composed of one or more molecular or polymeric organic materials rather than of a mixture of ions in a liquid solution. The main advantage of a OSC over DSSCs is the increased mechanical and thermal robustness of such devices which, however, comes at the cost of slightly lower energy conversion efficiencies. Furthermore, from the physical point of view OSCs have little in common with DSSCs as the phenomena causing energy absorption is the transit of electrons in the photosensitive layer to higher energy states within the same material rather than an oxidation reaction. Nonetheless, as will be shown later, the mathematical equations stemming by the different models bear many similarities. Although organic electronics have earlier origins, the key event in the historical development of OSCs was the discovery of conductive organic polymers which is set to 1977 by Heeger, MacDiarmid and Shirakawa, whose work was so important to earn them the Nobel Prize in Chemistry in 2000 [68]. In 1985 in his pioneering work [73] Tang showed the first organic solar cell with an efficiency of about 1%. Many developments have been made since then and nowadays the efficiency record is 8.3%, obtained by Heliatek laboratories [41] using small organic molecules and a particular tandem architecture in which two cells are stacked.
In this chapter we first illustrate the basic concepts of organic electronics and then we switch to the physical phenomena underlying the working principle of these cells. After that, the various types of internal morphologies are described and finally we discuss the main mathematical models for OSCs presently available in the specialized literature and highlight some improvements that where introduced during the development of the present thesis.
Our presentation of organic electronics is far from being exhaustive. For a thorough details see, for example, [45] while for the state of the art in device morphology we

refer see, e.g., [52].

3.1 Organic electronics

To introduce organic electronics we might say that the role played by silicon in inorganic electronics is taken by carbon in organic materials. These two elements share the outer electron configuration and, as silicon compounds can be either insulators or conductors, carbon molecules and macromolecules show the same variety of behaviour depending on their structure. Carbon atom has six electrons, four of which in the outer orbitals ($2s^2 2p^2$). When bound together, these orbitals can hybridize in three forms sp_1, sp_2 or sp_3 and therefore they can give origin to three kinds of bounds [3]. The most interesting state for organic electronics is sp_2 which is shown in Fig. 3.1. When sp_2 hybridized carbon atoms are bound together, a double bond

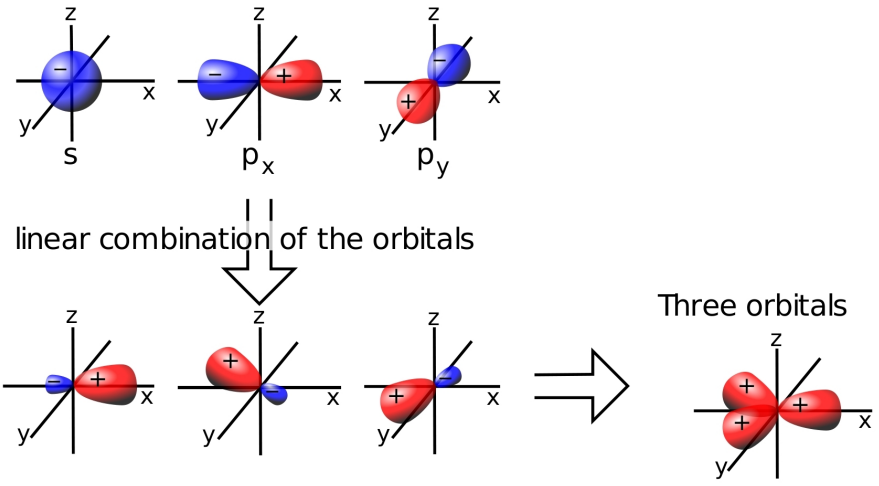

Figure 3.1: sp_2 orbitals, as linear combination of atomic orbitals.

is formed by the interaction of two sp_2 orbital (σ bond) and of the two remaining p orbitals (π bond). The first interaction is a strong one, which determines the structure of the molecule and the electrons involved are confined with high ionization potentials. π-type bonds are instead weaker and the electrons are more delocalized and they are responsible of the semiconducting properties of some organic molecules. A classical example of this structure is represented by ethylene, see Fig. 3.2.
The property of an organic structure to set up delocalized molecular orbitals is called conjugation. In particular, in carbon atom sequences like the ones in organic polymers, conjugation occurs when single and double covalent bonds appear alternately. In such a situation a series of molecular orbitals is formed by interference of electron

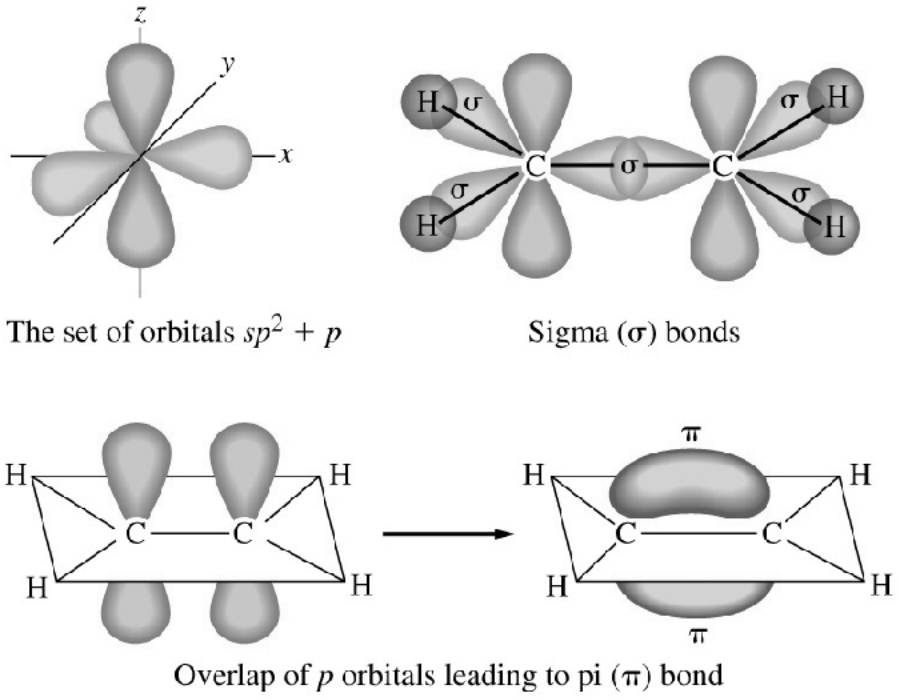

Figure 3.2: σ and π molecular orbitals in case of ethylene.

wavefunctions, each with a different energy level, and just half of them (π-type) are filled by electrons, while the remaining (π^*-type) are left unoccupied. The highest occupied π molecular orbital is called HOMO and it is the inorganic counterpart of the valence band in organic semiconductors, while the lowest unoccupied π^* molecular orbital is called LUMO and corresponds to the conduction band. Between them there is a forbidden range of energies, analogous to the concept of energy gap.
When a neutral molecule gains an electron, it occupies the lowest free π^* orbital. If an electron is lost instead, the uncharged molecule is assumed to gain a hole, which occupies the highest π orbital. Materials showing these two behaviors are respectively called electron acceptors and electron donors and the phenomenon is strictly connected with the concept of electron affinity. Charges can move in the organic material by means of two processes, motion inside each molecule and the intermolecular *hopping*. The first is a direct consequence of the phenomenon of delocalized molecular orbitals we explained before. Coherent intermolecular transmission is very unlikely since in an organic solid, molecules are bound together by weak Van der Wals forces, that lead to poor orbital overlap. Charges move instead from a molecule to another by means of a combination of phononic vibrations and quantum tunneling, respectively for overcoming energetic and spatial barriers. Fig. 3.3 reports a schematic representation of the phenomenon. Intramolecular coherent transport is much faster

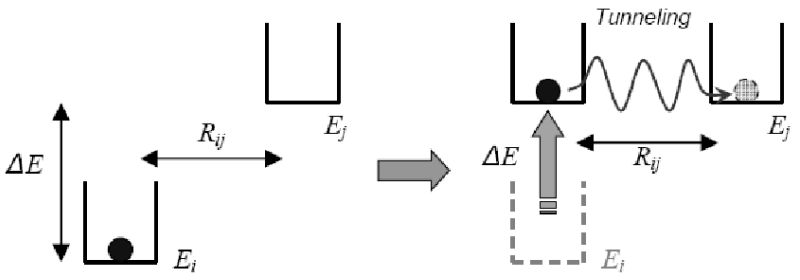

Figure 3.3: Hopping event. A phonon has to be absorbed in order to fill the energetic gap. Then the spatial gap is overcome with a tunneling event.

than tunneling-based intermolecular one. For this reason the latter acts as a bottleneck for charge motion, bringing to the characteristic low global mobility values for organic semiconductors, usually in the range of 10^{-11}-10^{-7} $m^2V^{-1}s^{-1}$.
Organic materials have other features that, in addiction to the ones we already explained, can be seen as advantages with respect to classical inorganic semiconductors and for this reason researchers started to use them in photovoltaics. First of all they are much cheaper and employing them in the fabrication of solar cells could bring to an important reduction in the material cost. Secondly they are mainly soluble an this opens to several inexpensive deposition techniques like casting, spin coating and ink-jet printing, unsuitable for inorganic semicondutors. All these techniques take place at low temperatures, which allows devices to be fabricated on plastic substrates. Moreover they have particular characteristics of transparency, colour, light weight and flexibility that can be exploited in many applications.
Several conjugated materials have been synthesized and in this work we focused mainly on polymers. Some examples of molecules used in photovoltaics are reported in Fig. 3.4 where on the first row are shown hole-conducting (p-type) polymers while on the second are electron-conducing (n-type) materials, in particular PCBM, a derivative of fullerene, a non-organic compound of carbon. All these materials can absorb light in the visible-UV parts of the spectrum and the resulting neutral excited state is called singlet exciton, an analogue of a bound electron-hole pair in conventional inorganic semiconductors but with higher values of binding energy between 0.1-1.4 eV.
These aspects are better discussed in the next section, where the operational principles of OSCs are outlined together with the description of the device morphologies used in producing solar cells.

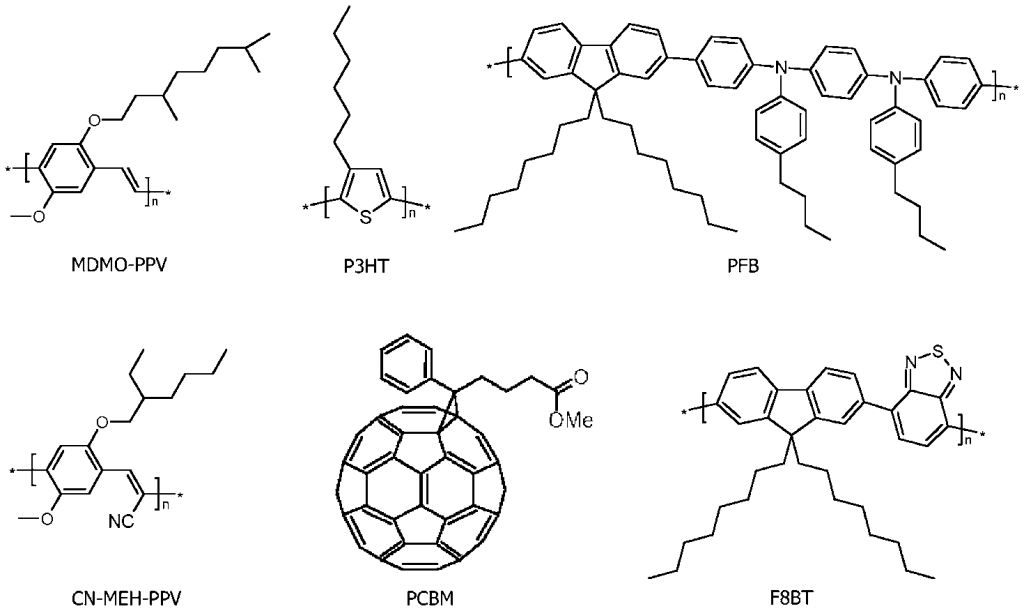

Figure 3.4: Some conjugated polymers and a soluble C_{60} derivative commonly applied in solar cells.

3.2 Operating principles and device structure of OSCs

As we stated previously, when a conjugated material is illuminated with visible or UV radiation, excited states named excitons are created but unlike what happens in classical semiconductors, they do not spontaneously deliver an electron-hole pair. This is due to two facts: first charge carriers move slowly because of the low mobilities and, second, dielectric constants are very small ($\varepsilon_r \sim 3$-4) and make Coulomb attractive forces more important. Singlet excitons can diffuse moving from a molecule to another or they can decay producing a photon or a long-lived and lower energy excited state called triplet. Excitons that diffuse to an interface between two different materials may transition to a state which is intermediate between strong coupling and complete dissociation, called polaron pair. In this configuration charges are still bound together but lie each on one side of the material interface and their coulombic attraction is partially screened by the chemical potential drop due to the difference in electron affinity. Polarons are trapped on the interface and do not diffuse. They can either dissociate into free charges, breaking the coulombian bond under the action of an electric field, or decay back to the exciton state, diffusing into one of the two materials in contact. The concept of polaron pair will be clearer when introducing the internal device structure of OSCs.

The common design of an OSC is represented in Fig. 3.5. The photoactive layer is usually sandwiched between two electrodes made respectively of transparent indium tin oxide (ITO)-covered glass and aluminum. The two contacts may be modified by

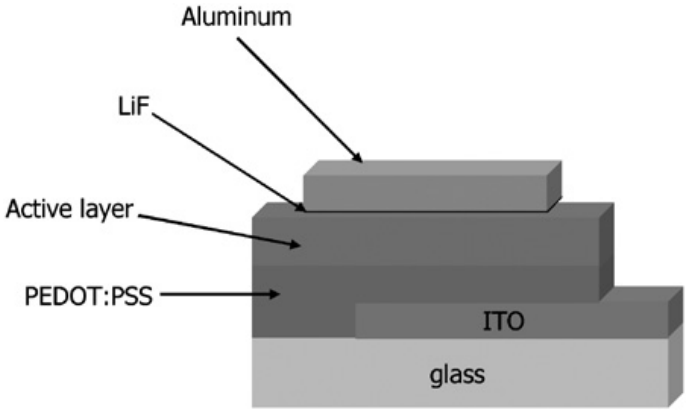

Figure 3.5: Common design of an organic solar cell.

the introduction of other layers, for example as in Fig. 3.5 PEDOT:PSS and lithium fluoride, in order to diminish the energy barrier heights and thus improve charge injection properties. The architecture of the photoactive layer is one of the most important factors in determining the efficiency of the solar cell and the evolution of the design used in practice is represented in Fig. 3.6.

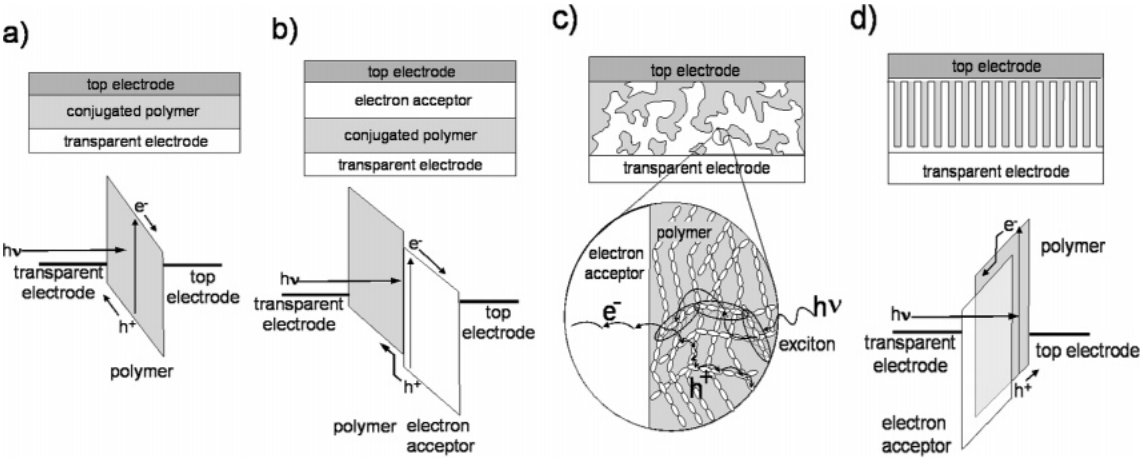

Figure 3.6: Evolution of device architectures of conjugated polymer-based photovoltaic cells: (a) single layer, (b) bilayer, (c) disordered bulk heterojunction and (d) ordered bulk heterojunction (reproduced from [17]).

First prototypes of OSCs had an active layer made of a single organic material (Schottky-type devices) and charges could be dissociated at the Schottky junction, see Fig. 3.7(a). For the reduced diffusion length of excitons in organic materials ($\sim$3-10 nm) only the ones generated closely to the small area next to the contact (indicated by W in Fig. 3.7(a)) could contribute to the photocurrent. In addiction opposite charges had to travel in the same material with high probability of recombining back to the exciton state and hence limiting further the current.

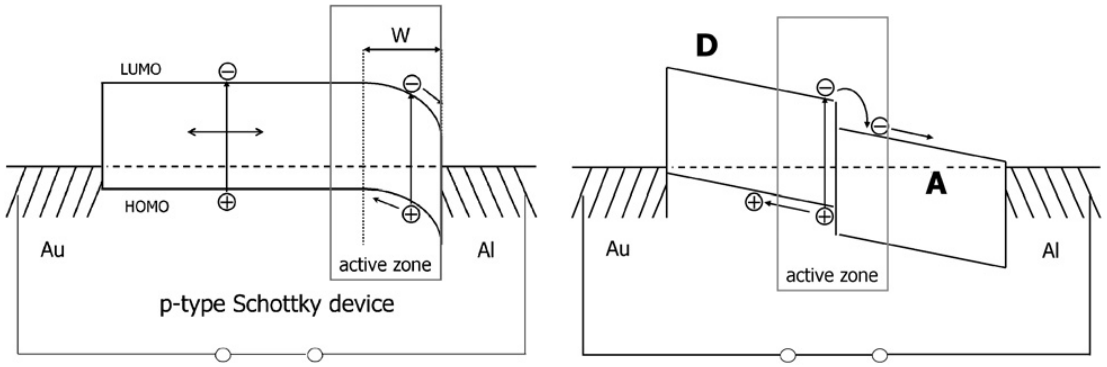

(a) Single layer device. (b) Double layer device.

Figure 3.7: Energy level diagrams for single and double layer devices.

As we previously reported, a significant improvement in device performance is obtained using two different materials in the photoactive layer arranged with a biplanar configuration. The materials need to have different electron affinities, respectively acting as electron-acceptor (n-type) and electron-donor (p-type). The working principle of a biplanar device is of particular interest for the development of the mathematical models used later on, therefore we analyse it here in more detail.
In the situation depicted in Fig. 3.8(a), the absorption of a photon has occurred in either materials and an exciton has been created. After that, the exciton starts to diffuse into the organic material and since it is neutrally charged the motion is driven only by concentration gradient with a characteristic diffusion length of a few nanometers.

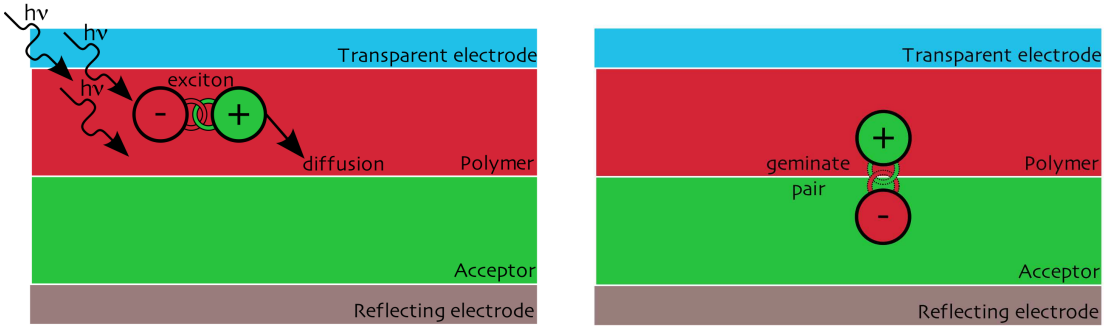

(a) Exciton generation and diffusion (b) Polaron pair creation

Figure 3.8: Photogeneration mechanism.

Fig. 3.8(b) clarifies the concept of polaron, or geminate pair. When an exciton is able to reach the donor-acceptor interface before decaying, the potential drop stretches it, generating a new particle, named polaron, in which charges are still coulombically bound with a lower energy and are localized in the two different materials. Polarons do not move on the interface and in their evolution they can either recombine back

to the exciton state or generate two free charge carriers under the action of the electric field.
Once charges are free to move (Fig. 3.9) they are transported with hopping events by drift caused by the built-in field, though diffusion can play an important role. Finally charges are collected at the electrodes generating the photocurrent.

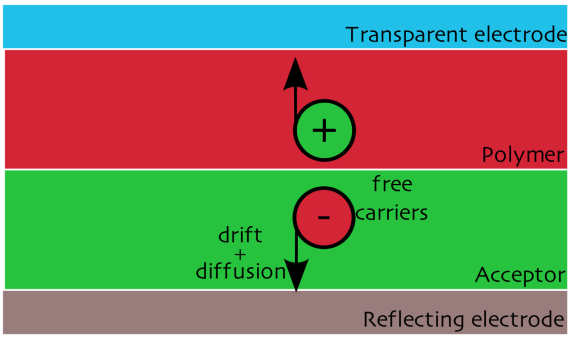

Figure 3.9: Transport of charge carriers.

As we previously said, excitons have a limited characteristic diffusion length (a few nanometers) while the bilayer of organic materials has a thickness of 100 nm or more. The consequence of this is that only the excitons that are generated in the proximity of the interface are successfully dissociated, while the majority of them decay to the ground state. Hence the active zone occupies only a minor portion of the device area, as it is shown in Fig. 3.7(b).
To overcome this limitation bulk heterojunction (BHJ) devices were conceived, in which donor and acceptor materials are blended together in order to maximize the interfacial area, see Fig. 3.10. In this way the distance that excitons have to cover

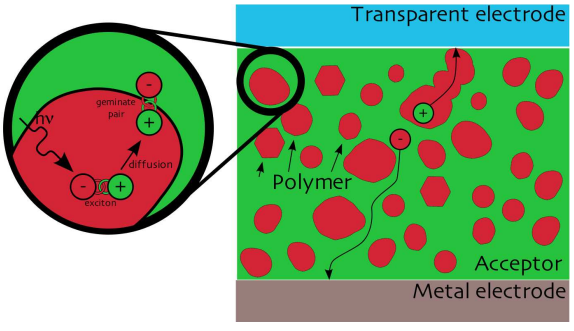

Figure 3.10: Bulk heterojuncion donor-acceptor blend.

before finding a dissociation site is intended to be of the same order of the diffusion length and a large part of them is successfully converted into the polaron form. The active zone extends throughout the full absorption region, as illustrated in Fig. 3.11 together with the energy levels diagram. The photoactive blends for BHJ devices

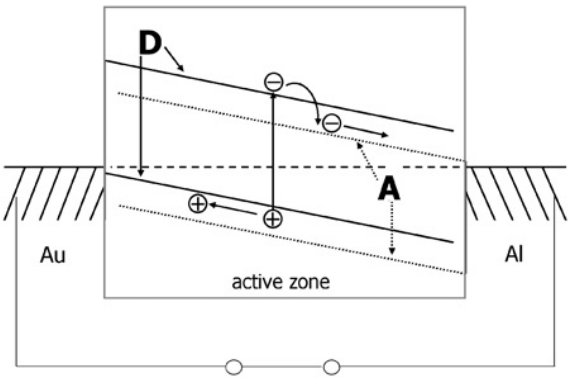

Figure 3.11: Energy levels in bulk heterojuncion devices.

are usually produced by spin-casting the donor and the acceptor from a common solution, that is a particular technique in which the materials are melted together while gradually solified.
This particular morphology has the positive effect of greatly increasing the produced photocurrent, nevertheless there are some aspects working against efficiency. First of all the disorder that enhances charge dissociation also has the side effect of reducing the effective mobility because carriers have to travel through a very complex pattern before reaching the electrodes. Secondly the donor-acceptor blend can show dead-end paths in which carriers are trapped and hence to recombine with an opposite sign charge into polaron state. Moreover the hopping-based transport involves molecular movement and this can bring to structural instabilities of the photoactive layer with consequent loss of performance over time.
For this reason several concepts of ordered bulk heterojuctions have been recently introduced, as an example see Fig. 3.6(d). Ordering the intermixed materials to the nanoscale would lead to superior mobility in both of them for the more regular path to be followed by the charge carriers. In addition the chances of charge trapping or structural instability would be minimized without a loss in terms of active interfacial area. Such structures can be obtained in several ways. One possible approach is to apply highly ordered inorganic nanostructures, in which the conjugated p-type polymer is filled in with a second step [52, 29, 71]. Two general types of structures may be distinguished, nanopores and nanorods, both produced by growth on the electrode substrate. These would have the double task of scaffolding the photoactive polymer and transporting the electrons to the cathode. For the reason that the n-type material is an inorganic one, most commonly transparent titanium-oxide (TiO_2) this kind of cells are called Hybrid Solar Cells. Another possible approach for the production of self-assembling ordered structures is to use copolymers [71], particular materials obtained by the junction of simpler polymers. Using triblock copolymers, with two

blocks having respectively donor and acceptor properties and the third acting as a connection, it is in principle possible to unify all the functionalities in a unique molecule.
Several other variants of the devices we presented are available in literature. For example it is very common to use an inorganic material as electron-acceptor in disordered bulk heterojunction cells in order to increase charge mobility. At the beginning of this chapter we mentioned that the efficiency record was achieved with a device that employs small organic molecules and a tandem architecture [41]. Small molecules are simpler than the polymers they share most electrical properties with, but they are characterized by higher mobilities and lower stability in time. A tandem architecture [52, 29, 71] sees two different cells stacked as shown in Fig. 3.12. The

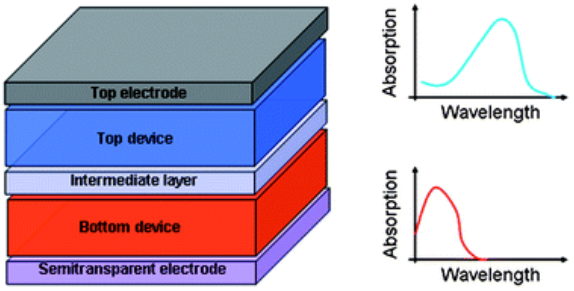

Figure 3.12: Tandem cells architecture and absorption wavelength ranges.

materials the cell is made of are chosen in such a way that the layers do not compete in photons absorption so that a larger part of the sunlight spectrum is used.

3.3 Mathematical models for OSCs

We will now present two mathematical models of the physical phenomena we described in the previous part of the chapter that differ in the morphology they refer to. The first model reproduces the behaviour of a bulk heterojunction device and, although the internal architecture in this case is the most complex among the ones we described, the underlying hypotheses make the model quite simple. The other model deals with nanostructured devices and considers in detail the phenomena that take place at the interface, an aspect which is not addressed in the previous case. This latter model is suitable for bilayer devices too, since morphology is simple but the way of handling the interface is the same.
For sake of clarity in the presentation, all the parameters appearing in the models that require an additional definition are described in Sect. 3.3.3.

3.3.1 Mathematical model for bulk-heterojunction devices

The model of bulk-heterojunction devices we report here is the one presented in the papers [20, 44] and in the Master Thesis [23], which we will refer to for details on parameter formulation.
The model has two main underlying hypotheses. First, mixing between donor and acceptor materials occurs even at very small characteristic lengths so that it is possible to consider the polymer blend as an uniform medium with model parameters obtained by averaging over the entire structure. Secondly, as the major part of excitons reach a dissociation site and are transformed into polaron pairs, it is possible to refer to them as synonyms.
Since we suppose the photoactive layer to be homogeneous and there are no phenomena that promote asymmetry in the behaviour of the cell, the effects in the directions perpendicular to the one in which current flows, that is from one electrode to the other, are unimportant. For this reason the model is basically one-dimensional. Nevertheless, as we decided to use a bidimensional code for the implementation in order to allow later improvements, we state the model in a 2D environment. Let $\Omega = [0, L]^2$ be the domain representing a section of the cell, with the boundary $\Gamma \equiv \partial\Omega$ divided in three disjoint subregions Γ_A, Γ_C and Γ_N respectively representing the anode, the cathode and the interior artificial boundaries, see Fig. 3.13. The additional x-

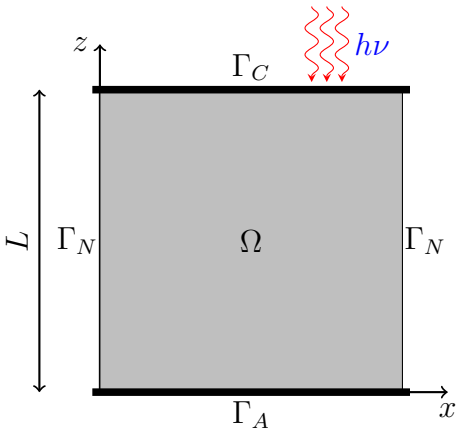

Figure 3.13: Schematic representation of the domain of the model for a bulk heterojunction solar cell.

dimension is treated as a *dummy* one and homogeneity is obtained by applying null flux conditions on the artificial boundariy Γ_N.
The equations of the model that describe the evolution of the spatial densities of electrons and holes, that we denote respectively with n and p (m^{-3}), can be derived from the conservation law for the electric charge. The continuity equations

expressing it are:

$$\begin{cases} \dfrac{\partial n}{\partial t} - \dfrac{1}{q}\operatorname{div}\mathbf{J}_n = G_n - R_n \\ \dfrac{\partial p}{\partial t} + \dfrac{1}{q}\operatorname{div}\mathbf{J}_p = G_p - R_p \end{cases} \qquad \text{in } \Omega \times (0, T_f), \tag{3.1}$$

where $T_f > 0$. Using from now on the symbol η to indicate either of n or p, $\mathbf{J}_\eta$ indicate the carrier *flux densities*, G_η are the *carrier generation rates* and R_η are the *recombination rates*. Although originally proposed for inorganic devices, the drift-diffusion model [46] for carrier flux densities still holds in this application and reads

$$\begin{cases} \mathbf{J}_n = qD_n\nabla n - q\mu_n n\nabla\varphi \\ \mathbf{J}_p = -qD_p\nabla p - q\mu_p p\nabla\varphi \end{cases} \qquad \text{in } \Omega \times (0, T_f), \tag{3.2}$$

φ being the electric potential, D_η the charge carrier *diffusion coefficients* and μ_η the *carrier mobilities*, which were found to be electric field dependent [65]. The first terms in (3.2) refer to gradient-driven diffusion while the other ones are due to an *electrostatic drift*.

Einstein relation [6, 44] is assumed to hold, meaning dependence of diffusivity on mobility,

$$D_\eta = \mu_\eta V_{TH} \tag{3.3}$$

where the *thermal voltage* is defined as $V_{TH} = K_B T/q$, K_B being the Boltzmann constant, T the absolute temperature and q the elementary charge, although it has been shown that diffusion coefficients can be enhanced at high charge densities [66]. Taking into consideration what we reported in the previous section, the source for carrier density is the dissociation of polaron pairs. Let us indicate with X the spatial density of polaron pairs (m^{-3}) and with k_{diss} their dissociation rate, the generation terms then read $G_\eta = k_{diss}X$ with the dissociation rate showing dependence on electric field too. We will later discuss some models for this parameter in section 3.3.3. The terms R_η account instead for the phenomena of *bimolecular recombination*, in which electrons and holes bound back together under the action of mutual attraction. The process is modeled using $R_\eta = \gamma np$ with the coefficient γ described according to the Langevin theory [53]. Also for this parameter more details will be stated later on.

The electrostatic potential φ appearing in (3.2), satisfies the Poisson equation

$$-\operatorname{div}\left(\varepsilon_0\varepsilon_r\nabla\varphi\right) = q(p - n) \qquad \text{in } \Omega \times (0, T_f), \tag{3.4}$$

where ε_0 is the electric constant and ε_r is the averaged relative dielectric permittivity of the blend. We remind that for the electric field it holds

$$\mathbf{E} = -\nabla\varphi.$$

The last equation entering in the model is the ordinary differential equation describing the evolution of exciton density X, that is

$$\frac{\partial X}{\partial t} = G - k_{rec}X + k_{diss}(\mathbf{E})X + \gamma np \qquad \text{in } \Omega \times (0, T_f). \tag{3.5}$$

The variation of this quantity is the sum of a source and reaction term. Positive contributes are given by the incident photon flux which determines an *exciton generation rate* G and by the balance of the recombination term γnp in equations (3.1). As we said in the previous section, exciton can either dissociate into charge carriers, see the term $-k_{diss}X$ appearing in equations (3.1), or decay to the ground state with a *recombination rate* k_{rec}.

The model has then to be closed with a proper set of boundary and initial conditions. On Γ_A and Γ_C, representing the metal electrodes in contact with the semiconducting blend, boundary conditions must describe the complex phenomenon of charge thermionic injection and recombination. In the work by Scott and Malliaras [16], starting from the Shottky barrier theory and considering the change of barrier height under the effect of the applied electric field and the image potential acting on charge carriers, Robin-type boundary conditions are obtained in the form

$$\begin{aligned} \gamma_n \frac{1}{q}\mathbf{J}_n \cdot \boldsymbol{\nu} &= \beta_n - \alpha_n n \\ -\gamma_p \frac{1}{q}\mathbf{J}_p \cdot \boldsymbol{\nu} &= \beta_p - \alpha_p p \end{aligned} \qquad \text{on } \big(\Gamma_A \cup \Gamma_D\big) \times (0, T_f), \tag{3.6}$$

where $\boldsymbol{\nu}$ is the outward normal unit vector along the boundary Γ. The parameters γ_η are non negative while β_η are the rates at which charges are injected into the device and α_η are the rates at which electrons and holes recombine with their image charges at the contacts, respectively [20]. However, modeling these parameters is still an issue of research and the description proposed in [16] needs to be modified empirically to avoid unphysical behaviour of the computed solution [44]. For more details on the parameters appearing in (3.6) see [23].

For the electric potential φ, the application of a voltage between the electrodes is considered and it is modeled using the Dirichlet conditions

$$\begin{aligned} \varphi &= V_{appl} - V_{bi} \qquad \text{on } \Gamma_A \times (0, T_f) \\ \varphi &= 0 \qquad\qquad\quad \text{on } \Gamma_C \times (0, T_f), \end{aligned} \tag{3.7}$$

where the chatode is assumed to be at ground potential. V_{appl} is the externally applied voltage while V_{bi} is the *built-in potential*, given by the difference between the workfunctions of the electrodes

$$V_{bi} = q(\phi_A - \phi_C).$$

As we previously reported, homogeneity along the *dummy direction* x is obtained with the imposition of null Neumann conditions on the artificial boundaries Γ_N

$$\begin{aligned} &\mathbf{J}_n \cdot \boldsymbol{\nu} = 0 \\ &\mathbf{J}_p \cdot \boldsymbol{\nu} = 0 \qquad\qquad \text{on } \Gamma_N \times (0, T_f). \\ &\varepsilon_0 \varepsilon_r \nabla \varphi \cdot \boldsymbol{\nu} = 0 \end{aligned} \tag{3.8}$$

Finally positive initial conditions for the densities are added to the model

$$n(\mathbf{x}, 0) = n_0(\mathbf{x}), \quad p(\mathbf{x}, 0) = p_0(\mathbf{x}), \quad X(\mathbf{x}, 0) = X_0(\mathbf{x}) \qquad \text{in } \Omega.$$

We now summarise what we described in this section restating the model in a more concise way. The subproblems that have to be solved are:

$$\begin{cases} \dfrac{\partial n}{\partial t} - \operatorname{div}\Big(\mu_n V_{TH}\nabla n - \mu_n n\nabla\varphi\Big) = k_{diss}X - \gamma np & \text{in } \Omega\times(0,T_f) \\ \gamma_n\big(\mu_n V_{TH}\nabla n - \mu_n n\nabla\varphi\big)\cdot\boldsymbol{\nu} = \beta_n - \alpha_n n & \text{on } \big(\Gamma_A\cup\Gamma_C\big)\times(0,T_f) \\ \big(\mu_n V_{TH}\nabla n - \mu_n n\nabla\varphi\big)\cdot\boldsymbol{\nu} = 0 & \text{on } \Gamma_N\times(0,T_f) \\ n(\mathbf{x},0) = n_0(\mathbf{x}) & \text{in } \Omega, \end{cases} \tag{3.9}$$

$$\begin{cases} \dfrac{\partial p}{\partial t} - \operatorname{div}\Big(\mu_p V_{TH}\nabla p + \mu_p p\nabla\varphi\Big) = k_{diss}X - \gamma np & \text{in } \Omega\times(0,T_f) \\ -\gamma_p\big(\mu_p V_{TH}\nabla p + \mu_p p\nabla\varphi\big)\cdot\boldsymbol{\nu} = \beta_p - \alpha_p p & \text{on } \big(\Gamma_A\cup\Gamma_C\big)\times(0,T_f) \\ -\big(\mu_p V_{TH}\nabla p + \mu_p p\nabla\varphi\big)\cdot\boldsymbol{\nu} = 0 & \text{on } \Gamma_N\times(0,T_f) \\ p(\mathbf{x},0) = p_0(\mathbf{x}) & \text{in } \Omega, \end{cases} \tag{3.10}$$

$$\begin{cases} \dfrac{\partial X}{\partial t} = G - k_{rec}X + k_{diss}(E)X + \gamma np & \text{in } \Omega\times(0,T_f) \\ X(\mathbf{x},0) = X_0(\mathbf{x}) & \text{in } \Omega, \end{cases} \tag{3.11}$$

$$\begin{cases} -\operatorname{div}\Big(\varepsilon_0\varepsilon_r\nabla\varphi\Big) = q\big(p-n\big) & \text{in } \Omega\times(0,T_f) \\ \varphi = V_{appl} - V_{bi} & \text{on } \Gamma_A\times(0,T_f) \\ \varphi = 0 & \text{on } \Gamma_C\times(0,T_f) \\ -\varepsilon_0\varepsilon_r\nabla\varphi = 0 & \text{on } \Gamma_N\times(0,T_f). \end{cases} \tag{3.12}$$

Remark 3.3.1. A simpler approach for charge carrier boundary conditions can be considered in place of Scott-Malliaras boundary conditions (3.6). Since electrons at the anode experience a high barrier between the workfunction of the ITO layer and the LUMO of the acceptor and the same holds for holes regarding the metallic cathode and the HOMO of the donor, very few particles would overcome this gap contributing to the injection current. The result of this is are small dark current values. Assuming contact to be of ohmic type, implying that the Fermi levels line up to the ones of the materials of the blend, and the validity of Maxwell-Boltzmann statistics, we get the following boundary conditions

$$\begin{aligned} &n = N_0 exp\left(-\tfrac{V_{bi}}{V_{TH}}\right) \\ &p = P_0 \end{aligned} \quad \text{on } \Gamma_A\times(0,T_f) \qquad \begin{aligned} &n = N_0 \\ &p = P_0 exp\left(-\tfrac{V_{bi}}{V_{TH}}\right) \end{aligned} \quad \text{on } \Gamma_C\times(0,T_f) \tag{3.13}$$

These modifications have little impact on the results of the model in stationary regime, since charge carrier density magnitudes are mostly determined by the external generation term. Output current is not affected either because it depends on the slope of the density solution next to the electrodes and changes in the boundary value have small impact on it. For this reason we often adopted these boundary conditions, especially for exploratory simulations.

3.3.2 Mathematical model for nanostructured heterojunction devices

We now focus on the devices whose morphology is characterised by a sharp distinction of the areas occupied by the acceptor and the donor materials, namely planar double layer solar cells and nanostructured heterojunction ones.
The milestone work for modeling these kind of cells is [6] in which a 1D model for bilayer devices is developed, including continuity equations for charge carriers and Poisson equation for the electric potential. Excitons are identified for simplicity with polaron pairs and since they are assumed to exist only at the interface, which in this case comes to be just a point, their evolution is described by a 0-D model (ODE). Coupling between excitons and free carriers is achieved by means of a term acting only in a neighbourhood of the interface of a given width H, where all the phenomena of dissociation, decay and recombination are assumed to take place. Apart of this, the approach is very similar to the one of our model for bulk heterojunction cells we described in the previous section, using Einstein relation, Scott-Malliaras boundary conditions and Langevin-type recombination.
The first attempt for a bidimensional model was made in [14]. In that work polaron pairs are still treated as a synonym of excitons but they are assumed to exist over the entire device and the relative continuity equation is added to the model. Nevertheless the handling of the terms modeling the interface phenomena is unclear and lacking of mathematical rigour.
The previous two references were further developed in [78, 77] by Willams and Walker, whose model represented the starting point in the definition of ours. In their production the key modification was the distinction between excitons, which are assumed to live and calculated all over the domain, and polaron pairs, supposed to be trapped on the interface. In that way the model is more consistent with the physics of the problem. Nevertheless the dissociation and recombination phenomena are still modeled with a term acting in a thin slab across the interface in the same fashion as [6], making implementation a bit tricky. Our work focused on the improvement of this aspect, transferring the effects of the active area term directly into the interface conditions, resulting in a more mathematically elegant and rigor-

ous representation.
There are two main assumptions at the basis of our model. First, all the phenomena that bring to the generation or the loss of a polaron pair are located at the interface between the acceptor and the donor. Anyway, a parameter H, representing the characteristic distance from the interface that all the phenomena take place within, is kept from the formulation in [78, 77]. The second hypothesis comes from the fact that donor material has low values for both electron affinity and mobility. For this reason electron density is very likely to assume negligible values and it is reasonable to suppose it equal to zero in the whole acceptor area. The same argument holds for holes in the donor material.
We consider a domain Ω divided into two parts Ω_p and Ω_n, which represent respectively the area occupied by the p-type donor material and by the n-type acceptor one, with a separating interface $\Gamma = \Omega_p \cap \Omega_n$ of arbitrary profile, see Fig. 3.14. Anode

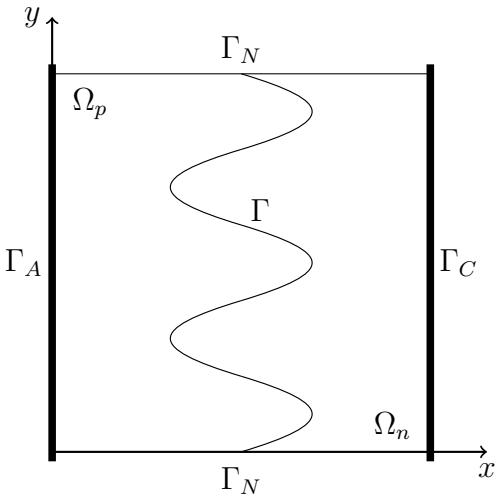

Figure 3.14: Schematic representation of the domain of the model for a nanostructured heterojunction solar cell.

and cathode are represented respectively by the portions of the boundary named coherently to the BHJ model with Γ_A and Γ_C. The parts indicated as Γ_N are instead artificial boundaries where symmetric conditions are applied.
Keeping n and p for spatial carrier densities as in the model of the previous section and using the second of the two hypotheses we previously stated, the evolution of electrons and holes is determined again by the continuity equations

$$\begin{cases} \dfrac{\partial n}{\partial t} - \dfrac{1}{q}\operatorname{div} \mathbf{J}_n = 0 & \text{in } \Omega_n \times (0, T_f) \\ n = 0 & \text{in } \big(\Omega_p \setminus \Gamma\big) \times (0, T_f), \end{cases} \tag{3.14}$$

$$\begin{cases} \dfrac{\partial p}{\partial t} + \dfrac{1}{q}\mathrm{div}\,\mathbf{J}_p = 0 & \text{in } \Omega_p \times (0, T_f) \\ p = 0 & \text{in } \big(\Omega_n \setminus \Gamma\big) \times (0, T_f). \end{cases} \tag{3.15}$$

Notice that the right hand sides of the continuity equations differ with respect to (3.1) since polaron pair dissociation and charge pair recombination are assumed to occur only on the interface Γ and the associated terms are supposed to appear in the corresponding boundary condition. Again, drift-diffusion model is used for the definition of carrier flux densities

$$\begin{cases} \mathbf{J}_n = qD_n\nabla n - q\mu_n n\nabla\varphi & \text{in } \Omega_n \times (0, T_f) \\ \mathbf{J}_p = -qD_p\nabla p - q\mu_p p\nabla\varphi & \text{in } \Omega_p \times (0, T_f) \end{cases} \tag{3.16}$$

and Einstein relation (3.3) is assumed to hold in both materials.
For a clearer presentation of the model we now anticipate with respect to what we did for the previous one the description of boundary conditions to be applied for charge densities equations. Following the simpler approach of Remark 3.3.1, Dirichlet-type boundary conditions are applied at the electrodes

$$\begin{aligned} n &= N_0 \exp\left(-\frac{\phi^c_{bn}}{k_B T}\right) && \text{on } \Gamma_C \times (0, T_f) \\ p &= P_0 \exp\left(-\frac{\phi^a_{bp}}{k_B T}\right) && \text{on } \Gamma_A \times (0, T_f) \end{aligned} \tag{3.17}$$

with the equivalent state densities N_0 and P_0 defined by

$$N_0 = N_C \exp\left(-\frac{E^a_{gap}}{2k_B T}\right) \qquad P_0 = N_V \exp\left(-\frac{E^d_{gap}}{2k_B T}\right) \tag{3.18}$$

ϕ^c_{bn} and ϕ^a_{bp} being the thermionic emission injection barrier height respectively for electrons at the cathode and for holes at the anode, N_C and N_V are the conduction and valence band densities of states and E^a_{gap} and E^d_{gap} are the bandgaps in the acceptor and in the donor materials.
As a consequence of the first hypothesis we stated at the beginning of this presentation, the carrier flux densities on the interface Γ are the sum of the positive contribution due to dissociation of polaron pairs, whose spatial density is indicated by X (m^{-2}), and the negative term of bimolecular recombination

$$\begin{aligned} \mathbf{J}_n \cdot \boldsymbol{\nu}_n &= k_{diss}(\mathbf{E})X - \gamma npH && \text{on } \Gamma \times (0, T_f) \\ -\mathbf{J}_p \cdot \boldsymbol{\nu}_p &= k_{diss}(\mathbf{E})X - \gamma npH && \text{on } \Gamma \times (0, T_f). \end{aligned} \tag{3.19}$$

This feature represents one of the improvements with respect to the model in [78, 77] since it allows to handle the physical phenomena modeling without introducing a

boundary layer that would lead to a more difficult numerical implementation. Notice the parameter H that is inherited from [78, 77], acting for both dimensional balance and accounting for the extension of the photoactive area.
On the artificial boundaries null flux is imposed to enforce symmetry conditions

$$\begin{aligned} \mathbf{J}_n \cdot \boldsymbol{\nu} &= 0 \qquad \text{on } \left(\partial\Omega_n \cap \Gamma_N\right) \times (0, T_f) \\ -\mathbf{J}_p \cdot \boldsymbol{\nu} &= 0 \qquad \text{on } \left(\partial\Omega_p \cap \Gamma_N\right) \times (0, T_f). \end{aligned} \tag{3.20}$$

The electrostatic potential φ appearing in the drift-diffusion model (3.16) satisfies Poisson equations that slightly differ from (3.4) since charge carriers live in distinct areas of the domain and that read

$$\begin{aligned} -\mathrm{div}\left(\varepsilon_0 \varepsilon_{rn} \nabla\varphi\right) &= -qn \qquad \text{in } \Omega_n \times (0, T_f) \\ -\mathrm{div}\left(\varepsilon_0 \varepsilon_{rp} \nabla\varphi\right) &= qp \qquad \text{in } \Omega_p \times (0, T_f), \end{aligned} \tag{3.21}$$

with $\varepsilon_{r\eta}$ as the relative dielectric permittivity of the material in the subdomain Ω_η. Boundary conditions for φ are the same as in the previous model, namely

$$\begin{aligned} \varphi &= V_{appl} - V_{bi} \qquad \text{on } \Gamma_A \times (0, T_f) \\ \varphi &= 0 \qquad \text{on } \Gamma_C \times (0, T_f) \\ \left(-\varepsilon_0 \varepsilon_{r\eta} \nabla\varphi\right) \cdot \boldsymbol{\nu} &= 0 \qquad \text{on } (\partial\Omega \cap \Gamma_N) \times (0, T_f). \end{aligned} \tag{3.22}$$

At the interface Γ two more conditions are needed. The first comes from potential continuity and the second is derived from the continuity of the normal component of the *electric displacement field*

$$\mathbf{D} = \varepsilon_0 \varepsilon_{r\eta} \mathbf{E} = -\varepsilon_0 \varepsilon_{r\eta} \nabla\varphi.$$

Defining the *jump operator* between two sets Ω_1 and Ω_2 for a scalar quantity θ as

$$[\![\theta]\!]_\Gamma = \theta|_{\Omega_1} - \theta|_{\Omega_2}$$

and for a vector one $\boldsymbol{\psi}$

$$[\![\boldsymbol{\psi}]\!]_\Gamma = \boldsymbol{\psi}|_{\Omega_1} \cdot \boldsymbol{\nu}_1 + \boldsymbol{\psi}|_{\Omega_2} \cdot \boldsymbol{\nu}_2$$

the interface conditions are

$$\begin{cases} [\![\varphi]\!]_\Gamma = 0 \\ [\![-\varepsilon_0 \varepsilon_{r\eta} \nabla\varphi]\!]_\Gamma = 0 \end{cases} \qquad \text{on } \Gamma \times (0, T_f). \tag{3.23}$$

As in [78, 77] excitons are considered separately from polaron pairs and, while these latter are calculated only on the interface, a continuity equation in the whole domain for excitons is added to the model. By indicating exciton spatial density with S, it reads

$$\frac{\partial S}{\partial t} + \mathrm{div}\, \mathbf{J}_S = G - \frac{S}{\tau_{S,dec}} \qquad \text{in } (\Omega_n \cup \Omega_p) \times (0, T_f) \tag{3.24}$$

where in the right hand side G denotes the exciton spatial generation rate and the second term models the exciton decay with characteristic lifetime $\tau_{S,dec}$.
Excitons have no charge and for this reason the associated flux is not influenced by electric field $\mathbf{E}$ and it is driven only by diffusion with parameter D_S

$$\mathbf{J}_S = -D_S \nabla S \qquad \text{in } (\Omega_n \cup \Omega_p) \times (0, T_f). \tag{3.25}$$

At the electrodes excitons are assumed to be perfectly separated [77] so

$$S = 0 \qquad (\Gamma_A \cup \Gamma_D) \times (0, T_f), \tag{3.26}$$

but since both charges are harvested by the same contact, no contribution to photocurrent is given. This aspect is however still not fully understood and controversial, needing for further modeling effort in future work.
Excitons are supposed to be continuous across the interface Γ and the jump of the relative density flux is given, accordingly to the description of the physical phenomena, by the sum of a term due to their dissociation into polaron pairs and another one referable to the decay of these latter

$$\begin{cases} [\![S]\!]_\Gamma = 0 \\ [\![\mathbf{J}_S]\!]_\Gamma = \dfrac{HS}{\tau_{S,diss}} - \eta_{st} k_{rec} X \end{cases} \qquad \text{on } \Gamma \times (0, T_f). \tag{3.27}$$

Here $\tau_{S,diss}$ is the characteristic time of the transition from exciton to polaron pair state and k_{rec} is the rate at which the opposite phenomenon takes place. It is important to highlight that only singlet excitons can play an active role in the photogenerative process [31]. The parameter η_{st} accounts exactly for the fraction of singlet excitons over the total number of them and since they are in a ratio 1:3 [31], η_{st} is set equal to 0.25.
The second condition in (3.27) is a novel feature of our model which differs from the one in [78, 77] as in that work excitons were supposed to be perfectly dissociated at the interface too, leading to a Dirichlet-type null condition like the one of (3.26).
The last equation of the model is again the one describing the evolution of polaron pairs which has a form similar to (3.5)

$$\frac{\partial X}{\partial t} = \frac{HS}{\tau_{S,diss}} - k_{rec} X + k_{diss}(\mathbf{E}) X + \gamma n p H \qquad \text{in } \Gamma \times (0, T_f) \tag{3.28}$$

with the difference that now this equation is considered only along the interface Γ. The first and the last term at the right-hand side are the positive contributions due to the state transition from exciton state and bimolecular recombination while the remaining ones model the opposite phenomena.

At last, positive initial conditions for the densities are needed to close the model

$$\begin{array}{llll} n(\mathbf{x},0) = n_0(\mathbf{x}) & \text{in } \Omega_n & p(\mathbf{x},0) = p_0(\mathbf{x}) & \text{in } \Omega_p \\ S(\mathbf{x},0) = S_0(\mathbf{x}) & \text{in } \Omega_n \cup \Omega_p & X(\mathbf{x},0) = X_0(\mathbf{x}) & \text{on } \Gamma. \end{array} \tag{3.29}$$

Again we summarise the model in compact way, dividing it into subproblems.

$$\begin{cases} \dfrac{\partial n}{\partial t} - \operatorname{div}\left(\mu_n V_{TH} \nabla n - \mu_n n \nabla \varphi\right) = 0 & \text{in } \Omega_n \times (0, T_f) \\ n = N_0 \exp\left(-\dfrac{\phi_{bn}^c}{k_B T}\right) & \text{on } \Gamma_C \times (0, T_f) \\ \left(\mu_n V_{TH} \nabla n - \mu_n n \nabla \varphi\right) \cdot \boldsymbol{\nu}_n = k_{diss}(\mathbf{E}) X - \gamma n p H & \text{on } \Gamma \times (0, T_f) \\ \left(\mu_n V_{TH} \nabla n - \mu_n n \nabla \varphi\right) \cdot \boldsymbol{\nu} = 0 & \text{on } \left(\partial\Omega_n \cap \Gamma_N\right) \times (0, T_f) \\ n(\mathbf{x}, 0) = n_0(\mathbf{x}) & \text{in } \Omega_n \end{cases} \tag{3.30}$$

$$\begin{cases} \dfrac{\partial p}{\partial t} - \operatorname{div}\left(\mu_p V_{TH} \nabla p + \mu_p p \nabla \varphi\right) = 0 & \text{in } \Omega_p \times (0, T_f) \\ p = P_0 \exp\left(-\dfrac{\phi_{bp}^a}{k_B T}\right) & \text{on } \Gamma_C \times (0, T_f) \\ -\left(D_p \nabla p + \mu_p p \nabla \varphi\right) \cdot \boldsymbol{\nu}_p = k_{diss}(\mathbf{E}) X - \gamma n p H & \text{on } \Gamma \times (0, T_f) \\ -\left(D_p \nabla p + \mu_p p \nabla \varphi\right) \cdot \boldsymbol{\nu} = 0 & \text{on } \left(\partial\Omega_p \cap \Gamma_N\right) \times (0, T_f) \\ p(\mathbf{x}, 0) = p_0(\mathbf{x}) & \text{in } \Omega_p \end{cases} \tag{3.31}$$

$$\begin{cases} \dfrac{\partial S}{\partial t} - \operatorname{div}\left(D_S \nabla S\right) = G - \dfrac{S}{\tau_{S,dec}} & \text{in } (\Omega_n \cup \Omega_p) \times (0, T_f) \\ S = 0 & \text{on } (\Gamma_A \cup \Gamma_D) \times (0, T_f) \\ [\![S]\!]_\Gamma = 0 & \text{on } \Gamma \times (0, T_f) \\ [\![-D_S \nabla S]\!]_\Gamma = \dfrac{HS}{\tau_{S,diss}} - \eta_{st} k_{rec} X & \text{on } \Gamma \times (0, T_f) \\ S(\mathbf{x}, 0) = S_0(\mathbf{x}) & \text{in } \Omega_n \cup \Omega_p \end{cases} \tag{3.32}$$

$$\begin{cases} \dfrac{\partial X}{\partial t} = \dfrac{HS}{\tau_{S,diss}} - k_{rec} X + k_{diss}(\mathbf{E}) X + \gamma n p H & \text{on } \Gamma \times (0, T_f) \\ X(\mathbf{x}, 0) = X_0(\mathbf{x}) & \text{on } \Gamma \end{cases} \tag{3.33}$$

$$\begin{cases} -\operatorname{div}\left(\varepsilon_0 \varepsilon_{rn} \nabla \varphi\right) = -qn & \text{in } \Omega_n \times (0, T_f) \\ -\operatorname{div}\left(\varepsilon_0 \varepsilon_{rp} \nabla \varphi\right) = qp & \text{in } \Omega_p \times (0, T_f) \\ \varphi = V_{appl} - V_{bi} & \text{on } \Gamma_A \times (0, T_f) \\ \varphi = 0 & \text{on } \Gamma_C \times (0, T_f) \\ \left(-\varepsilon_0 \varepsilon_{r\eta} \nabla \varphi\right) \cdot \boldsymbol{\nu} = 0 & \text{on } (\partial\Omega \cap \Gamma_N) \times (0, T_f) \\ [\![\varphi]\!]_\Gamma = 0 & \text{on } \Gamma \times (0, T_f) \\ [\![-\varepsilon_0 \varepsilon_{r\eta} \nabla \varphi]\!]_\Gamma = 0 & \text{on } \Gamma \times (0, T_f) \end{cases} \tag{3.34}$$

3.3.3 Modeling parameters

As we already reported, charge carrier mobilities assume in organic materials much lower values than in classical inorganic semiconductors and they are found to be dependent on the electric field **E** [65] and weakly on the carrier density [74] due to the presence of disorder. As in most works in literature [6, 14, 44, 77, 78] we opted to use a simplified Poole-Frenkel model

$$\mu_\eta = \mu_{\eta 0} \exp\left(\xi_\eta \sqrt{E}\right) \tag{3.35}$$

where $\mu_{\eta 0}$ is the zero-field carrier mobility, E is the magnitude of the electric field vector and ξ_η is a material dependent parameter.
The Langevin model [50] for γ in homogeneous materials can be expressed by

$$\gamma = \frac{q(\mu_n + \mu_p)}{3\varepsilon_0 \varepsilon_r}$$

where the sum of mobilities is used since both carriers are free to move towards each other. For this reason the fastest carrier type determines the recombination rate. This approach was used in [6, 14] even though the phenomena in bilayer and bulk heterojunctions seems to act differently. In fact, when recombination occurs at an interface between two materials and the carriers are confined in distinct regions, a charge has to wait for an opposite sign one to approach and hence the slowest carrier determines the recombination rate. This is reproduced using the following formula for γ proposed in [78, 77]

$$\gamma = \frac{q \min(\mu_n, \mu_p)}{3\varepsilon_0 \varepsilon_r} \tag{3.36}$$

in which the smaller of the two carrier mobilities is considered.
For polaron dissociation rate k_{diss}, instead, different approaches are used for the two models we presented. In the case of bulk-heterojunction devices the parameter is modeled as in [23] following Onsager's theory [59] which was later extended by Braun in [11]. It is calculated by using the formula

$$k_{diss}(\mathbf{E}) = \frac{3\gamma}{4\pi a^3} \exp\left(-\frac{V_B}{V_{TH}}\right)\left(1 + b + \frac{b^2}{3} + \frac{b^3}{18} + \frac{b^4}{180}\right) \tag{3.37}$$

where γ is the Langevin constant, a is the distance between the bound charges and V_B and b are defined by

$$V_B = \frac{q}{4\pi\varepsilon_0\varepsilon_r a} \qquad b = \frac{qE}{8\pi\varepsilon_0\varepsilon_r V_{TH}},$$

being respectively the polaron pair binding potential and a proper scaling of the electric field strength.

In bilayer and nanostructured devices polarons can instead be dissociated only in one direction, while in BHJs the convoluted nature of the interface makes separation to occur in every direction, and for this reason the phenomenon is enhanced for negative values of the electric field. An appropriate model for k_{diss} has to take these facts into consideration and the model proposed in [6] and later used in [78, 77] goes in that direction. The polaron pair dissociation rate is hence given by

$$k_{diss}\left(\mathbf{E}\right) = \begin{cases} \dfrac{2k_{diss}(0)}{M}\left[\exp(M)\left(1-\dfrac{1}{M}\right)+\dfrac{1}{M}\right] & \text{for } E_n < 0 \\ \dfrac{4k_{diss}(0)}{M^2}\left(1-\exp\left(-\dfrac{M^2}{4}\right)\right) & \text{for } E_n \geq 0 \end{cases} \tag{3.38}$$

where $k_{diss}(0)$ is the value at zero field, M is defined by

$$M = \frac{q}{k_B T}\sqrt{\frac{q|E_n|}{\pi\varepsilon_0\varepsilon_r}}$$

and E_n is the averaged normal electric field across the interface Γ

$$E_n = \frac{1}{2}\Big(\mathbf{E}_{\Omega_n}\cdot\boldsymbol{\nu}_n - \mathbf{E}_{\Omega_p}\cdot\boldsymbol{\nu}_p\Big).$$

In Fig. 3.15 the dependence of the two considered models on the electric field is

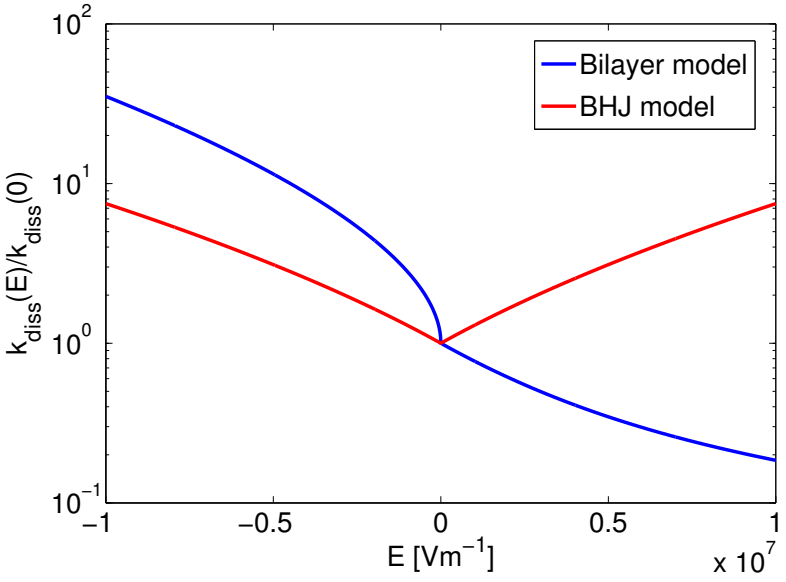

Figure 3.15: Normalized dependence of polaron pair dissociation rate.

depicted, clearly showing the enhancement of k_{diss} for negative values of the field and the reduction of k_{diss} for positive ones, in the case of for the modified model with respect to Onsager's theory. In addiction, notice the symmetry of the behaviour for

Onsager's approach due to the fact that direction is not considered in that model. The last parameter to be described is the exciton generation rate G and several choices are available for it. Some works in literature used uniform in space generation rates [44, 20, 23] and, although this represents a quite rough approximation of the phenomenon of absorption, the results are satisfactory. In [78, 77] and [14] the effect of progressive absorption in the material, with the consequent decrease of exciton generation, is considered using a Lambertian profile of the type

$$G(x, y) = \Phi\alpha \exp\left(-\alpha(x - \overline{x})\right) \tag{3.39}$$

where Φ is the incident photon flux, α the absorption coefficient and $\overline{x}$ is the x-coordinate of the closest point to the transparent electrode at which absorption occurs. These two approaches are the ones we considered in our work. More complicated models can be used, as for example see [78, 77] or [75], in which light reflection and refraction phenomena are considered, but we didn't analyse these aspects of the modeling which will be subject of future work.

Chapter 4

Numerical Methods

In this chapter we present the numerical techniques used to solve the mathematical models introduced in Chapters 2 and 3. For a comprehensive numerical and analytical discussion of the BHJ model we refer to the works [23] and [20]. Here, in the first part, we will refer to the model for nanostructured device since the DSSC models, from the mathematical point of view, are a special instance of it. Later on, in the chapter we will consider simplified model problems, in order to lighten the notation and make concepts easier to handle and describe.

Our approach is based on Rothe's method (also known as method of horizontal lines) which consists of three main steps: first, the time dependent problem is transformed into a sequence of stationary differential problems by approximating the time derivatives with a suitable difference formula; then, the resulting non-linear elliptic problems are linearized by the Newton-Raphson method; finally, the obtained linear differential problems are solved numerically using the edge average finite element method (EAFE) [80, 32, 5], a very popular scheme in the numerical simulation of semiconductor devices.

4.1 Time Discretization

In the first step of Rothe's method we transform the time dependent problems into a sequence of stationary elliptic problems, replacing the partial time derivative with a finite difference approximation. The approximation can be chosen among several methods; specifically, we adopt Backward Differencing Formulas (BDF [2]) of order $m \leq 5$. To define the resulting stationary problem, let $0 = t_0 < \cdots < t_K < T_f$ be a strictly increasing, not necessarily uniformly spaced, finite sequence of time levels and assume the quantities n, p, X, S and φ to be known functions of $\boldsymbol{x}$ for every

t_k, $k = 0$ ... K - 1. Then we obtain

$$\begin{cases} \sum_{k=0}^{m} \theta_k n_{K-k} - \frac{1}{q}\mathrm{div}\,\mathbf{J_n}(n_K, \varphi_K) & = 0 \\ \sum_{k=0}^{m} \theta_k p_{K-k} + \frac{1}{q}\mathrm{div}\,\mathbf{J_p}(p_K, \varphi_K) & = 0 \\ \sum_{k=0}^{m} \theta_k S_{K-k} + \mathrm{div}\,\mathbf{J_S}(S_K) - U_K & = 0 \\ \sum_{k=0}^{m} \theta_k X_{K-k} - W_K & = 0 \\ -\mathrm{div}\,(\varepsilon_0 \varepsilon_{rn} \nabla\varphi) + qn & = 0 \\ -\mathrm{div}\,(\varepsilon_0 \varepsilon_{rp} \nabla\varphi) - qp & = 0 \end{cases} \tag{4.1}$$

where $f_k = f(\mathbf{x},t_k)$ for any generic function $f(\mathbf{x},t)$, while U_K and W_K are the right-hand sides of the equations (3.24) and (3.28). Equations (4.1), together with the constitutive relations for the fluxes given in (3.16) and (3.25) and the set of boundary conditions, constitute a system of nonlinear elliptic differential equations coupled with two algebraic constrain equations ($(4.1)_{5-6}$).
In our work, the selection of the successive time level t_k and of the formula's order m, as well as the computation of the coefficients θ_k, $k = 0$, ..., m, is performed adaptively in such a way to minimize the time discretisation error while minimizing the total number of time steps.

4.2 Linearization

Given a nonlinear PDEs system, it is very difficult, and in most cases impossible, to determine an analytical solution for the problem itself. A possible way out to overcome this difficulty is to apply an iterative procedure. Functional iterations provide an explicit approach to translate the original nonlinear system into a sequence of linear problems, the solution of which should converge to a corresponding solution of the original problem.
We adopt the Newton-Raphson method as functional iteration technique for the linearization and successive solution of problem (4.1). To ease the notation, throughout this subsection the subscripts denoting the time level will be dropped. Denoting by $\boldsymbol{y} = [n, p, S, X, \varphi]^T$ be the vector of dependent variables, the nonlinear system (4.1)

can be written in compact form as

$$\mathbf{F}(\mathbf{y}) = \mathbf{0}, \qquad \text{with} \qquad \mathbf{F}(\mathbf{y}) = \begin{Bmatrix} f_n(n,p,X,\varphi) \\ f_p(n,p,X,\varphi) \\ f_S(X,S) \\ f_X(n,p,S,X) \\ f_{\varphi n}(n,\varphi) \\ f_{\varphi p}(p,\varphi) \end{Bmatrix}, \tag{4.2}$$

where f_i is the nonlinear operator associated with the i-th equation of system (4.1). One step of the Newton-Raphson method can be written as

$$\mathbf{J}(\mathbf{y})\Delta\mathbf{y} = -\mathbf{F}(\mathbf{y}), \tag{4.3}$$

where $\mathbf{J}$ is the Jacobian matrix and $\Delta\mathbf{y} := [\Delta n, \Delta p, \Delta S, \Delta X, \Delta\varphi]^T$ is the unknown increment vector. The Jacobian entries are given by the Frechét derivative $\partial_a(f)$ with respect to unknown a. The exact computation of all the derivatives in the Jacobian can become quite complicated if the full model for all the coefficients is taken into account, since most coefficients are electric field dependent. To solve this problem, we adopt a quasi-Newton method where, rather than the exact Jacobian $\mathbf{J}(\mathbf{y})$, we use an approximation $\tilde{\mathbf{J}}(\mathbf{y})$ in which the dependence of the mobilities, of the diffusion coefficients and of the dissociation coefficient on the electric field is neglected. This approach has the further advantage of consuming less memory when implemented numerically and facilitating the software library we adopt.

4.3 Spatial Discretization

Once the linearization is applied, the resulting linear system of PDEs is numerically approximated by means of the Galerkin-Finite element method (G-FEM). Standard G-FEM are in general not suitable for problems where the drift terms become dominant since numerical solution may be affected by the presence of spurious oscillations if the mesh size is not small enough. Many special techniques have been developed to avoid the occurrence of this inconvenient, including finite volume methods [21], streamline diffusion finite volume methods [47] and the hybrid streamline-upwinding-Petrov-Galerkin method [12, 43]. We decide not to adopt any of these approaches, rather, we use the Edge-Averaged Finite Element (EAFE), a multidimensional extension to finite elements of the Scharfetter-Gummel difference scheme, which provides an exponential fitting finite element discretization [5, 32, 80, 51]. The advantage of emploing the EAFE method is that if a maximum principle holds for the problem on the continuous level then discrete counterpart holds too [80]. A scheme that satisfies a maximum principle is referred to as a *monotone scheme* [80]. A well-known

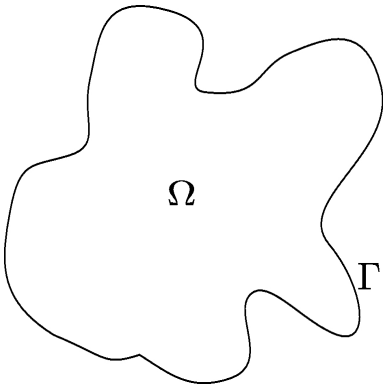

Figure 4.1: Problem Domain

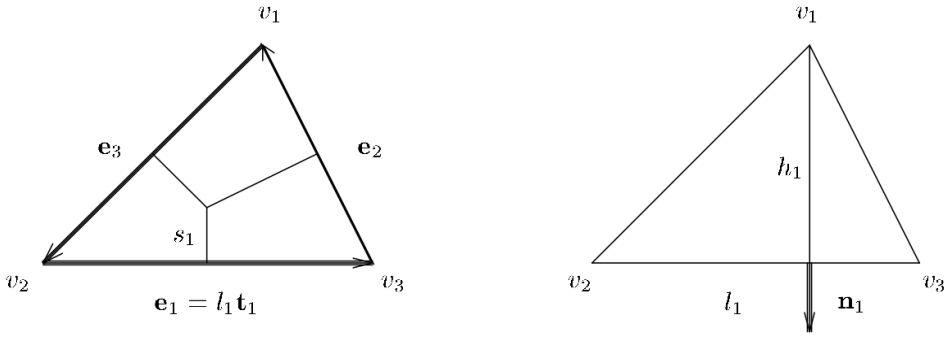

Figure 4.2: Parameters associated with triangle K

sufficient condition for a scheme to be monotone is that the corresponding stiffness matrix is an M-matrix. It can be shown that the stiffness matrix obtained with this method is an M-matrix under the sole assumption that the triangulation of the domain is of Delaunay type [80]. This fact is very important since if the EAFE is applied to a carrier continuity equation in the Drift-Diffusion model, it ensures that the computed carrier concentration is strictly positive. In addition, this method preserves the current, along the edges of the triangulation.
We consider the EAFE method applied to the following model continuity equation for u, on a domain $\Omega \subset \mathbb{R}^2$ with boundary $\partial\Omega = \Gamma$ (see Fig.4.1):

$$\begin{cases} -\mathrm{div}\,\mathbf{J}(u) = f & \text{in } \Omega \\ u = 0 & \text{on } \Gamma \end{cases} \tag{4.4}$$

where $\mathbf{J} = \mu(\nabla u - u\nabla\psi)$, $\mu \in \mathcal{C}^0(\overline{\Omega})$ is a strictly positive real function such that $\mu = \mu(\mathbf{x}) \geq \mu_0 \geq 0$ for every $\boldsymbol{x} \in \Omega$, ψ is a continuous linear piecewise function over $\overline{\Omega}$ and $f \in \mathrm{L}^2(\Omega)$.

Upon introducing the following change of variable

$$u := ne^{\psi}. \tag{4.5}$$

Using (4.5) into the definition of the flux yields

$$\boldsymbol{J}(n) = \mu e^{\psi} \nabla n \tag{4.6}$$

from which the weak formulation of problem (4.4) is: find $n \in H_0^1(\Omega)$ such that

$$B(n, v) = 0 \quad \forall v \in H_0^1(\Omega), \tag{4.7}$$

where

$$B(n, v) = \int_{\Omega} \mathbf{J}(n) \cdot \nabla v \, \mathrm{d}\Omega \tag{4.8}$$

is the bilinear form associated with the problem. It can be easily checked that the bilinear form is continuous and coercive on H_0^1, then the application of the Lax-Milgram Lemma ensures that problem (4.7) has a unique solution, this automatically implying that also (4.4) admits a unique weak solution $u \in H_0^1(\Omega)$.
We now apply the G-FEM with piecewise linear finite elements on a regular triangulation $\mathcal{T}_h$ of the domain Ω, such that

$$\overline{\Omega} = \bigcup_{K \in \mathcal{T}_h} K \tag{4.9}$$

and with the following properties:

- $\mathrm{int}\,(K) \neq \emptyset$
- $\mathrm{int}\,(K_1) \cap \mathrm{int}\,(K_2) = \emptyset$ for each distinct K_1, $K_2 \in \mathcal{T}_h$
- if $F = K_1 \cap K_2 \neq \emptyset$ (with K_1 and K_2 distinct elements of $\mathcal{T}_h$) then F is a common side or vertex of K_1 and K_2
- $\mathrm{diam}(K) \leq h$ for each $K \in \mathcal{T}_h$.

For simplicity of exposition we assume that the triangulation covers Ω exactly. Given $K \in \mathcal{T}_h$, we introduce some local notation for triangles. As pictured in Fig. 4.2, we label the vertices v_i, $i = 1, 2, 3$ in counterclockwise order. Let the edge opposite v_i be denoted $\mathbf{e}_i$ and oriented such that it connects v_{i+1} to v_{i-1}. Let l_i denote its length, and $\mathbf{t}_i$ the unit tangent vector oriented in the same direction. Denote the unit outward normal vector to edge $\boldsymbol{e}_i$ by $\mathbf{n}_i$ and denote the segment from the midpoint of $\mathbf{e}_i$ to the intersection of the perpendicular edge bisectors by s_i. We will also need a difference operator along $\mathbf{e}_i$ defined, for each continuous functions, as

$$\delta_i(\eta) = \eta(v_{i-1}) - \eta(v_{i+1}). \tag{4.10}$$

Finally, let $V_h = \{v \in \mathcal{C}^0(\overline{\Omega}) : v|_K \in \mathbb{P}^1\} \subset H_0^1$ be the piecewise linear finite element space and denote the nodal basis functions by ϕ_i which are one at v_i and zero at the other vertices.
The equation associated with the generic test function ϕ_h over K for the problem (4.7) reads:

$$\int_K \mathbf{J}(n_h) \cdot \nabla \phi_h = 0, \qquad \phi_h,\, n_h \,\in V_h. \tag{4.11}$$

The approximation of $\mathbf{J}_h$ with standard G-FEM leads to the following discrete weak formulation

$$\int_K \mathbf{J}_h^{GAL}(n_h) \cdot \nabla \phi_h = 0, \qquad \phi_h,\, n_h \,\in V_h. \tag{4.12}$$

where $\mathbf{J}_h^{GAL}(\mathrm{n}_h) = \bar{a}\ \nabla n_h^k$. The quantity $\bar{a}$ is the integral average of μe^{ψ} over the element K:

$$\bar{a} = \frac{\displaystyle\int_K \mu e^{\psi}\, d\mathbf{x}}{|K|} \tag{4.13}$$

then, from the choice of the finite element space, the flux $\mathbf{J}_h^{GAL}(\mathrm{u}_h)$ is constant over the single triangle of the mesh. Compared to standard G-FEM, the EAFE method is characterized by a different treatment of the flux over K, in fact the diffusion coefficient of the differential operator is not simply approximated through an integral average but with an harmonic average along the triangle sides $\mathbf{e}_i$.
Given a function $\eta \in \mathcal{C}^0(\overline{K})$, we define the harmonic average of η along the edge $\mathbf{e}_i$ as follows

$$\widehat{\eta} := \left(\frac{\displaystyle\int_{\mathbf{e}_i} \eta^{-1}\, \mathrm{ds}}{l_i} \right)^{-1}. \tag{4.14}$$

Taking into account relation (4.14), we derive the EAFE discrete weak formulation of (4.7)

$$\int_K \mathbf{J}_h^{EA}(n_h) \cdot \nabla \phi_h = 0, \qquad \phi_h,\, n_h \,\in V_h \tag{4.15}$$

where

$$\mathbf{J}_h^{EA}(n_h) = \sum_{j=1}^{3} J_j^{EA}(n_h)\, \mathbf{j}_j. \tag{4.16}$$

The first term in the last relation can be explicitly written as

$$J_j^{EA} = \widehat{a}_j \nabla n_h \cdot \mathbf{t}_j = \widehat{a}_j \frac{\delta_j(n_h)}{l_j} \tag{4.17}$$

where $\widehat{a}_j$ is the harmonic average of μe^{ψ} along $\mathbf{e}_j$, in this case equal to:

$$\widehat{a} := \left(\frac{\displaystyle\int_{\mathbf{e}_j} (\mu e^{\psi})^{-1}\, ds}{l_j} \right)^{-1} = \mu e^{\psi_{j-1}} \mathrm{Be}(\psi_{j-1} - \psi_{j+1}), \tag{4.18}$$

$\mathrm{Be}(\psi_j)$ being the inverse Bernoulli function, defined as

$$\mathrm{Be}(x) := \frac{x}{e^x - 1} \tag{4.19}$$

The choice of piecewise linear finite elements is crucial, because in this way the flux projection J_j^{EA} along each triangle edge is a constant value, which can be used to construct the approximation of $\mathbf{J}$ over K. The second term of (4.16) is a basis function set for the flux approximation along the edge:

$$\mathbf{j}_j = \frac{l_j s_j}{|K|} \mathbf{t}_j. \tag{4.20}$$

The above description shows that the $\mathbf{J}_h^{EA}(n_h)$ is a constant approximation of $\mathbf{J}(n)$ over the element K and a linear operator that allows to reconstruct a vector field over K starting from its tangential components along the triangle edges [5].
For the numerical implementation of the method and to analyze its monotonicity, it is essential to derive the stiffness matrix associated with to each element K. Substituting in (4.15) the test function ϕ_h with the basis function ϕ_i $(i = 1, 2, 3)$ defined on the triangle K we obtain

$$\begin{aligned} \int_K \mathbf{J}_h^{EA}(n_h) \cdot \nabla \phi_i &= \sum_j^3 J_j^{EA}(n_h) \int_K \mathbf{j}_j \cdot \nabla \phi_i \\ &= J_{i-1}^{EA}(n_h) \int_K \frac{l_{i-1} s_{i-1} \mathbf{t}_{i-1}}{|K|} \cdot \nabla \phi_i \\ &\quad + J_i^{EA}(n_h) \int_K \frac{l_i s_i \mathbf{t}_i}{|K|} \cdot \nabla \phi_i \\ &\quad + J_{i+1}^{EA}(n_h) \int_K \frac{l_{i+1} s_{i+1} \mathbf{t}_{i+1}}{|K|} \cdot \nabla \phi_i. \end{aligned} \tag{4.21}$$

Recalling that the following relationships hold on an arbitrary triangle K [4]:

$$\nabla \phi_i = -\frac{\mathbf{n}_i}{h_i} \tag{4.22}$$

$$l_i \mathbf{t}_i \cdot \nabla \phi_i = 0 \tag{4.23}$$

$$l_{i\pm1} \mathbf{t}_{i\pm1} \cdot \nabla \phi_i = \pm 1, \tag{4.24}$$

from (4.21) it follows that:

$$\int_K \mathbf{J}_h^{EA}(n_h)\cdot\nabla\phi_i = J_{i-1}^{EA}(n_h)\int_K \frac{l_{i-1}s_{i-1}\mathbf{t}_{i-1}}{|K|}\cdot\nabla\phi_i + J_{i+1}^{EA}(n_h)\int_K \frac{l_{i+1}s_{i+1}\mathbf{t}_{i+1}}{|K|}\cdot\nabla\phi_i. \tag{4.25}$$

In order to continue in the calculation of the local stiffness matrix we introduce an important property of (4.16) (see Lemma 4.1 [5])

$$\int_K \mathbf{J}_h^{EA}(n_h)\cdot\nabla\phi_i\, d\mathbf{x} = J_{i+1}^{EA}(n_h)s_{i+1} - J_{i-1}^{EA}(n_h)s_{i-1}. \tag{4.26}$$

Therefore the explicit form of the flux integration over K can be easily written highlighting the contribution of each basis function:

$$\begin{aligned}
\int_K \mathbf{J}_h^{EA}(n_h)\cdot\nabla\phi_1 &= J_2^{EA}(n_h)s_2 - J_3^{EA}(n_h)s_3 \\
&= \left(\hat{a}_2\frac{s_2}{l_2} + \hat{a}_3\frac{s_3}{l_3}\right)n_1 - \hat{a}_3\frac{s_3}{l_3}n_2 - \hat{a}_2\frac{s_2}{l_2}n_3 \\
\int_K \mathbf{J}_h^{EA}(n_h)\cdot\nabla\phi_2 &= J_3^{EA}(n_h)s_3 - J_1^{EA}(n_h)s_1 \\
&= -\hat{a}_3\frac{s_3}{l_3}n_1 + \left(\hat{a}_3\frac{s_3}{l_3} + \hat{a}_1\frac{s_1}{l_1}\right)n_2 - \hat{a}_1\frac{s_1}{l_1}n_3 \\
\int_K \mathbf{J}_h^{EA}(n_h)\cdot\nabla\phi_3 &= J_3^{EA}(n_h)s_1 - J_1^{EA}(n_h)s_2 \\
&= -\hat{a}_2\frac{s_2}{l_2}n_1 - \hat{a}_2\frac{s_1}{l_1}n_2 + \left(\hat{a}_1\frac{s_1}{l_1} + \hat{a}_2\frac{s_2}{l_2}\right)n_3,
\end{aligned} \tag{4.27}$$

that in algebraic form reads:

$$A^K\mathbf{n}^K = \mathbf{f}^k \tag{4.28}$$

where

$$A^K = \begin{bmatrix} \hat{a}_2\frac{s_2}{l_2} + \hat{a}_3\frac{s_3}{l_3} & -\hat{a}_3\frac{s_3}{l_3} & -\hat{a}_2\frac{s_2}{l_2} \\ -\hat{a}_3\frac{s_3}{l_3} & \hat{a}_3\frac{s_3}{l_3} + \hat{a}_1\frac{s_1}{l_1} & -\hat{a}_1\frac{s_1}{l_1} \\ -\hat{a}_2\frac{s_2}{l_2} & -\hat{a}_1\frac{s_1}{l_1} & \hat{a}_1\frac{s_1}{l_1} + \hat{a}_2\frac{s_2}{l_2} \end{bmatrix} \quad \mathbf{n}^K = \begin{bmatrix} n_1 \\ n_2 \\ n_3 \end{bmatrix} \tag{4.29}$$

Summing the above local contributions over each mesh triangle K, we can assemble the global stiffness matrix A of the problem. It is immediate to check that A is a M-matrix because its entries satisfy the following conditions:

$$\begin{aligned}
&A_{jj} > 0 \quad \forall j; && A_{ij} \quad \forall i,j \,:\, i \neq j; \\
&A_{jj} \geq \sum_{i=1, i\neq j}^{N_h} |A_{ij}| \quad \forall j; && A_{jj} > \sum_{i=1, i\neq j}^{N_h} |A_{ij}| \quad \text{for at least one } j.
\end{aligned} \tag{4.30}$$

Under the regularity assumptions on the problem coefficients and if the triangulation $\mathcal{T}_h$ is of Delaunay type, then A is an irreducible M-Matrix with respect to its columns and the discrete maximum principle holds. For a more general diffusion-convection equation, if we assume that the coefficients are piecewise smooth functions, the diffusion term is non-negative and the triangulation is weakly acute, then the stiffness matrix is an M-Matrix [80].
Returning to the original u variable, we have to invert (4.5) at each mesh node, obtaining:

$$A^K\mathbf{n} = \left(A^K \begin{bmatrix} e^{-\psi_1} & 0 & 0 \\ 0 & e^{-\psi_2} & 0 \\ 0 & 0 & e^{-\psi_3} \end{bmatrix} \right) \mathbf{u} \tag{4.31}$$

that gives back the two-dimensional Scharfetter-Gummel method on triangular meshes. For the error analysis of the method and its generalization to diffusion-convection-reaction problems see [80].

4.4 Substructuring Methods

In both DSSC and bilayer OSC models the solution of PDEs in two different domains are involved. To handle this problem, we applied a substructuring method properly designed for systems of partial differential equations. To simplify the presentation we introduce the following model boundary problem:

$$\begin{cases} -\operatorname{div}\mathbf{J}(u) = f & \text{in } \Omega \\ u = \varphi_D & \text{on } \Gamma_D \\ \mathbf{J}\cdot\boldsymbol{\nu} = \varphi_N & \text{on } \Gamma_N \end{cases} \tag{4.32}$$

In (4.32), Ω is supposed to be a two-dimensional domain with Lipschitz boundary $\partial\Omega = \Gamma_D \cup \Gamma_N$, such that $\Gamma_D \cap \Gamma_N = \emptyset$, whose outer normal direction is denoted by $\boldsymbol{\nu}$. We assume the operator $\mathbf{J}(u^{(i)}) = \mu(\nabla u + u\nabla\psi)$, $f \in L^2(\Omega)$, $\mu \in {}^{\infty}(\Omega)$, $0 < \delta < \mu$ in Ω, $\psi \in H^1(\Omega)$ and $\varphi_D, \varphi_N \in L^{\infty}(\partial\Omega)$. The assumptions are made to ensure the of the problem to admit a unique solution (c.f. Sect. 4.3).
To proceed with the multi-domain formulation, we introduce a partition of the computational domain Ω into two non overlapping subdomains Ω_1 and Ω_2. The interface $\Gamma = \overline{\Omega_1} \cap \overline{\Omega_2}$ is supposed to be a Lipschitz $(n-1)$-dimensional manifold (see Fig.4.3). In the following we indicate by $u^{(i)}$ the restriction on Ω_i $(i = 1, 2)$ of the solution u, and by $\boldsymbol{\nu}_i$ the outward pointing normal on $\partial\Omega_i$.

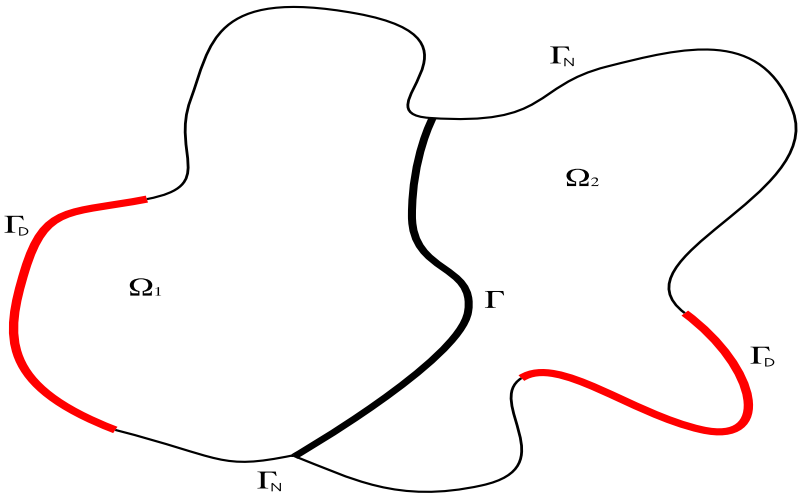

Figure 4.3: Example of possible computational domain

Then, our multi-domain reference problem is:

$$\begin{cases} -\operatorname{div} \mathbf{J}(u^{(i)}) = f & \text{in } \Omega_i \\ \mathbf{J}(u^{(i)}) \cdot \boldsymbol{\nu}_i = \varphi_N & \text{on } \Gamma_N \cap \Omega_i \\ u^{(i)} = \varphi_D & \text{on } \Gamma_D \cap \Omega_i \\ [\![u]\!]_\Gamma = 0 & \\ [\![\mathbf{J} \cdot \boldsymbol{\nu}_i]\!]_\Gamma = 0 & \end{cases} \tag{4.33}$$

The last two equations are called the *transmission conditions* at the interface Γ. In order to present the variational forms for problem (4.33) we introduce the bilinear form:

$$a_{\Omega_i}(w^{(i)}, v^{(i)}) = \int_{\Omega_i} \mathbf{J}(w^{(i)}) \cdot \nabla v^{(i)} \, d\Omega_i \tag{4.34}$$

and the linear functionals

$$F_{\Omega_i}(v^{(i)}) = \int_{\Omega_i} f v^{(i)} \, d\Omega_i \tag{4.35}$$

$$G_{\Omega_i}(v^{(i)}) = F_{\Omega_i}(v^{(i)}) + \int_{\partial\Omega_i} H v|_{\partial\Omega_i} \, d\sigma_i \tag{4.36}$$

where $H = \mathbf{J}(u^{(i)}) \cdot \boldsymbol{\nu}_i$ is the flux across the boundary $\partial\Omega_i$ (i.e $H = \varphi_N$ on Γ_N). The weak multidomain formulation of problem (4.33) can be obtained using the extension operators in order to describe interface conditions, in this way we obtain: find $u^{(1)} \in U_1$, $u^{(2)} \in U_2$ such that:

$$u^{(1)}\big|_\Gamma = u^{(2)}\big|_\Gamma \tag{4.37}$$

$$\sum_{i=1}^{2} \left[a_{\Omega_i}\Big(u^{(i)}, \mathcal{R}^{(i)}\eta\Big) \right] + G_{\Omega_i}\Big(\mathcal{R}^{(i)}\eta\Big) = 0 \quad \forall \eta \in \Lambda \tag{4.38}$$

$$a_{\Omega_1}\left(u^{(1)}, v^{(i)}\right) = G_{\Omega_1}\left(v^{(1)}\right) \quad \forall v^{(1)} \in V_{1,0} \tag{4.39}$$

$$a_{\Omega_1}\left(u^{(2)}, v^{(2)}\right) = G_{\Omega_2}\left(v^{(2)}\right) \quad \forall v^{(2)} \in V_{2,0} \tag{4.40}$$

where

$$V := H^1_{\Gamma_D} := \{v \in H^1(\Omega) \,:\, v|_{\Gamma_D} = 0\} \tag{4.41}$$

$$V_{i,0} := \{v \in H^1_{\Gamma_D}(\Omega_i) \,:\, v|_{\Gamma_D} = 0\}$$

$$\Lambda := \left\{\phi \in H^{1/2}(\Gamma) \,:\, \phi = v|_\Gamma \text{ for a suitable } v \in H^1_{\Gamma_D}(\Omega)\right\}$$

$$U_i := \left\{v \in H^1(\Omega_i) \,:\, v|_{\Gamma_D \cup \partial\Omega_i} = \varphi_D \text{ and } v|_{\Gamma_D} = 0\right\} \tag{4.42}$$

and $\mathcal{R}^{(i)}\eta$ denotes an extension of $\eta \in \Lambda$ to U_i. We observe that for i fixed the term

$$a_{\Omega_i}\left(u^{(i)}, \mathcal{R}^{(i)}\eta\right) - G_{\Omega_i}\left(\mathcal{R}^{(i)}\eta\right) \tag{4.43}$$

represents the flux through the interface Γ. It is thus clear that (4.47) represents a conservation law across the interface.

To introduce the discretization multidomain formulation of equations (4.37)-(4.40) we consider the same finite decomposition of the computational domain introduced in Sect. 4.3. Let then $U^h_{i,0}$ and $V^h_{i,0}$ denote finite dimensional subspaces of $U_{i,0}$ and $V_{i,0}$ defined as:

$$U^h_{i,0} := X^1_h(\Omega) \cap U_{i,0} := \left\{v_h \in \mathcal{C}^0(\overline{\Omega_i}) \,:\, v_h|_{K_i} \in \mathbb{P}_1(K_i) \,\forall\, K_i \,\in\, \mathcal{T}_h\right\} \cap U_{i,0} \tag{4.44}$$

$$V^h_{i,0} := X^1_h(\Omega) \cap V_{i,0} \tag{4.45}$$

i.e. the space of continuous piecewise-linear polynomial functions over each subdomain Ω_i.

Finally we derive the discretized form of system (4.37)-(4.40) applying the same method presented in Sect. 4.3 (omitting the EAFE superscript), obtaining:

$$u^{(1)}_h\Big|_\Gamma = u^{(2)}_h\Big|_\Gamma \tag{4.46}$$

$$\sum_{i=1}^{2}\left[a_{\Omega_i}\left(u^{(i)}_h, \mathcal{R}^{(i)}_h\eta\right)\right] + G_{\Omega_i}\left(\mathcal{R}^{(i)}_h\eta\right) = 0 \quad \forall \eta \in \Lambda^h \tag{4.47}$$

$$a_{\Omega_1}\left(u^{(1)}_h, v^{(i)}_h\right) = G_{\Omega_1}\left(v^{(1)}_h\right) \quad \forall v^{(1)}_h \in V^h_{1,0} \tag{4.48}$$

$$a_{\Omega_1}\left(u^{(2)}_h, v^{(2)}_h\right) = G_{\Omega_2}\left(v^{(2)}_h\right) \quad \forall v^{(2)}_h \in V^h_{2,0} \tag{4.49}$$

where

$$\Lambda^h := \left\{\phi \in H^{1/2}(\Gamma) \,:\, \phi = v|_\Gamma \text{ for a suitable } v \in X^1_h(\Omega)\right\}.$$

Now, it is possible to write the algebraic counterparts of (4.46)-(4.49). For each subdomain we can divide the nodes of the computational grid into three disjoint subsets:

$$\mathbf{u}^{(i)} = \begin{bmatrix} \mathbf{u}_I^{(i)} \\ \mathbf{u}_D^{(i)} \\ \mathbf{u}_\Gamma^{(i)} \end{bmatrix} \tag{4.50}$$

where $\mathbf{u}_\Gamma^{(i)}$ are the nodes belonging to Γ, $\mathbf{u}_D^{(i)}$ are the ones belonging to $\Gamma_D \cap \overline{\Omega}_i$ and $\mathbf{u}_I^{(i)}$ are the internal ones. The algebraic version of the problem for $i = 1, 2$ is

$$A^{(i)} \begin{bmatrix} \mathbf{u}_I^{(i)} \\ \mathbf{u}_D^{(i)} \\ \mathbf{u}_\Gamma^{(i)} \end{bmatrix} = \begin{bmatrix} \mathbf{b}_I^{(i)} \\ \mathbf{b}_D^{(i)} \\ \mathbf{b}_\Gamma^{(i)} \end{bmatrix} + M^{(i)} \begin{bmatrix} 0 \\ \mathbf{H}_D^{(i)} \\ \mathbf{H}_\Gamma^{(i)} \end{bmatrix}. \tag{4.51}$$

In the above notation $\mathbf{H}_D^{(i)}$ represents the flux on the Dirichlet sides as well as $\mathbf{H}_\Gamma^{(i)}$ represents the flux on Γ. The matrix:

$$A^{(i)} = \begin{bmatrix} A_{II}^{(i)} & A_{ID}^{(i)} & A_{I\Gamma}^{(i)} \\ A_{DI}^{(i)} & A_{DD}^{(i)} & 0 \\ A_{\Gamma I}^{(i)} & 0 & A_{\Gamma\Gamma}^{(i)} \end{bmatrix} \tag{4.52}$$

refers to the discretization of the term $a_{\Omega_i}(\,\cdot\,,\,\cdot\,)$, while:

$$M^{(i)} = \begin{bmatrix} 0 & 0 & 0 \\ 0 & M_{DD}^{(i)} & 0 \\ 0 & 0 & M_{\Gamma\Gamma} \end{bmatrix} \tag{4.53}$$

is a 3×3 sparse block matrix that takes into accounts the quadrature rule adopted for the computation of integral on the right hand side of (4.46)-(4.49). Notice that $M_{\Gamma\Gamma}$ does not have any domain index, because we have assumed the conformity of the two grids over Γ, therefore it must be $M_{\Gamma\Gamma}^{(1)} = M_{\Gamma\Gamma}^{(2)}$. The interface conditions are simply:

$$\mathbf{u}_\Gamma^{(1)} = \mathbf{u}_\Gamma^{(2)}, \tag{4.54}$$

$$\mathbf{H}_\Gamma^{(1)} + \mathbf{H}_\Gamma^{(2)} = 0. \tag{4.55}$$

As $\mathbf{u}_D^{(i)}$ is a given datum, we can reduce (4.66) to the following system:

$$\begin{bmatrix} A_{II}^{(i)} & A_{I\Gamma}^{(i)} \\ A_{\Gamma I}^{(i)} & A_{\Gamma\Gamma}^{(i)} \end{bmatrix} \begin{bmatrix} \mathbf{u}_I^{(i)} \\ \mathbf{u}_\Gamma^{(i)} \end{bmatrix} = \begin{bmatrix} \mathbf{b}_I^{(i)} \\ \mathbf{b}_\Gamma^{(i)} \end{bmatrix} - \begin{bmatrix} A_{ID}^{(i)} \mathbf{u}_D^{(i)} \\ 0 \end{bmatrix} + \begin{bmatrix} 0 \\ M_{\Gamma\Gamma} \mathbf{H}_\Gamma^{(i)} \end{bmatrix}. \tag{4.56}$$

Equation (4.56) is the starting point for the derivation of two different approaches to the solution of (4.33) namely the "Schur complement approach" [64] and the one

we call "Global approach" that we actually employ in our work. In order to construct the Schur-complement matrix it is necessary to consider some inverse matrices. The method we use in our implementation is based on an opposite point of view, without imposing the transmission conditions ($(4.33)_{4-5}$) in explicit way. In fact, using (4.54)-(4.56) we obtain:

$$\begin{bmatrix} A_{II}^{(1)} & 0 & A_{I\Gamma}^{(1)} \\ 0 & A_{II}^{(2)} & A_{I\Gamma}^{(2)} \\ A_{\Gamma I}^{(1)} & A_{\Gamma I}^{(2)} & \sum_{i=1}^{2} A_{\Gamma\Gamma}^{(i)} \end{bmatrix} \begin{bmatrix} \mathbf{u}_I^{(1)} \\ \mathbf{u}_I^{(2)} \\ \mathbf{u}_\Gamma \end{bmatrix} = \begin{bmatrix} \mathbf{b}_I^{(1)} - A_{ID}^{(1)}\mathbf{u}_D^{(1)} \\ \mathbf{b}_I^{(2)} - A_{ID}^{(2)}\mathbf{u}_D^{(2)} \\ \sum_{i=1}^{2} \mathbf{b}_\Gamma^{(i)} \end{bmatrix}. \tag{4.57}$$

Problem (4.57) has a definitely larger size but with respect to the "Schur complement approach" it is not necessary to deal with inverse matrix approximation.

4.5 Treatment of nonlocal boundary conditions

In this last section we describe the technique we employ to impose the nonlocal integral conditions that appear in the models for DSSCs devices. These particular conditions can account for various physical phenomena in several contexts (e.g. chemical engineering, thermoelasticity, population dynamics, heat conduction processes, control theory, medical science) and for this reason they gained much attention in recent years, in the mathematical community.
We consider the following model problem:

$$\begin{cases} -\operatorname{div} \mathbf{J}(u) = f & \text{in } \Omega \\ \mathbf{J}(u) \cdot \boldsymbol{\nu} = 0 & \text{on } \partial\Omega \\ \displaystyle\int_\Omega u \, \mathrm{d}x = 0 \end{cases} \tag{4.58}$$

with $\mathbf{J}(u) = \mu \nabla u$, $f \in L^2(\Omega)$, Ω being a two-dimensional domain with Lipschitz boundary $\partial\Omega$ and outer normal unit vector $\boldsymbol{\nu}$ defined on it. For simplicity of presentation we assume both null boundary flux condition and null average over the domain. A compatibility condition has then to be satisfied by f, in fact, integrating over the domain, applying the divergence theorem and using the boundary flux condition we have:

$$\int_\Omega f \, \mathrm{d}x = -\int_\Omega \operatorname{div} \mathbf{J}(u) \, \mathrm{d}x = -\int_{\partial\Omega} \mathbf{J}(u) \cdot \boldsymbol{\nu} \, \mathrm{d}x = 0 \tag{4.59}$$

meaning that f has to be a null average function too.
Let us introduce the space $V = H^1(\Omega)$ and the bilinear form

$$a(u, v) = \int_\Omega \nabla u \cdot \nabla v \, \mathrm{d}x \qquad \forall u, v \in V. \tag{4.60}$$

Then problem (4.58) is equivalent to the constrained minimization problem

$$\inf_{\substack{v\in V\\ \int_\Omega v=0}} \frac{1}{2}\,a(v,v) - \int_\Omega fv\,\mathrm{d}x. \tag{4.61}$$

Let Q be the space of constant functions over Ω and introduce the augmented Lagrange functional

$$\mathcal{F}(v,\lambda) = \frac{1}{2}\,a(v,v) - \int_\Omega fv\,\mathrm{d}x + \lambda\int_\Omega v\,\mathrm{d}x \tag{4.62}$$

with $\lambda \in Q$ acting as a Lagrange multiplier associated with the null average constraint. In this way (4.58) is in turn equivalent to the saddle point problem

$$\inf_{V\in V}\sup_{q\in Q}\mathcal{F}(v,\lambda) = \inf_{V\in V}\sup_{q\in Q}\frac{1}{2}\,a(v,v) - \int_\Omega fv\,\mathrm{d}x + \lambda\int_\Omega v\,\mathrm{d}x \tag{4.63}$$

from which we get the following in variational form: find $(u,\lambda)\in V\times Q$ such that:

$$\begin{cases} a(u,v) + \lambda\displaystyle\int_\Omega v\,\mathrm{d}x = \int_\Omega fv\,\mathrm{d}x & \forall v\in V\\ q\displaystyle\int_\Omega u\,\mathrm{d}x = 0 & \forall q\in Q. \end{cases} \tag{4.64}$$

To switch to the discrete form we introduce the finite element spaces

$$V_h = \left\{v\in\mathcal{C}^0(\Omega) : v|_K\in\mathbb{P}^1(K)\forall K\in\mathcal{T}_h\right\} \qquad Q_h = Q$$

and the variational problem straightforwardly turns into: find $(u_h,\lambda_h)\in V_h\times Q_h$ s.t.

$$\begin{cases} a_h(u_h,v_h) + \lambda_h\displaystyle\int_\Omega v_h\,\mathrm{d}x = \int_\Omega fv_h\,\mathrm{d}x & \forall v_h\in V_h\\ q_h\displaystyle\int_\Omega u_h\,\mathrm{d}x = 0 & \forall\quad q_h\in Q_h \end{cases} \tag{4.65}$$

where

$$a_h(u_h,v_h) = \int_\Omega \nabla u_h\cdot\nabla v_h\,\mathrm{d}x \qquad \forall u_h,v_h\in V_h.$$

denoting as usual ϕ_i the basis function associated with node v_i, A the stiffness matrix associated with $a(\,\cdot\,,\,\cdot\,)$ and vectors B and f whose elements are defined by

$$B_j = \int_\Omega \phi_j\,\mathrm{d}x \qquad f_j = \int_\Omega f\phi_j\,\mathrm{d}x \qquad \forall j$$

the algebraic form of problem (4.65) is

$$\begin{bmatrix} A & B^T\\ B & 0\end{bmatrix}\begin{bmatrix}\mathbf{u}\\ \lambda\end{bmatrix} = \begin{bmatrix}\mathbf{f}\\ 0\end{bmatrix}. \tag{4.66}$$

Chapter 5

Numerical simulations

In this final chapter we report and discuss the results of the simulations we performed considering several configurations of the devices we described in Chapters 2 and 3. Particular attention has been devoted to determine the effects of varying material parameters, external conditions and morphology in order to obtain some indications for optimal device design.

Before focusing on the analysis of the results of simulations for each family of devices, it is necessary to introduce some parameters and quantities that are commonly considered when characterizing photovoltaic cells. Figure 5.1 shows the shape of a

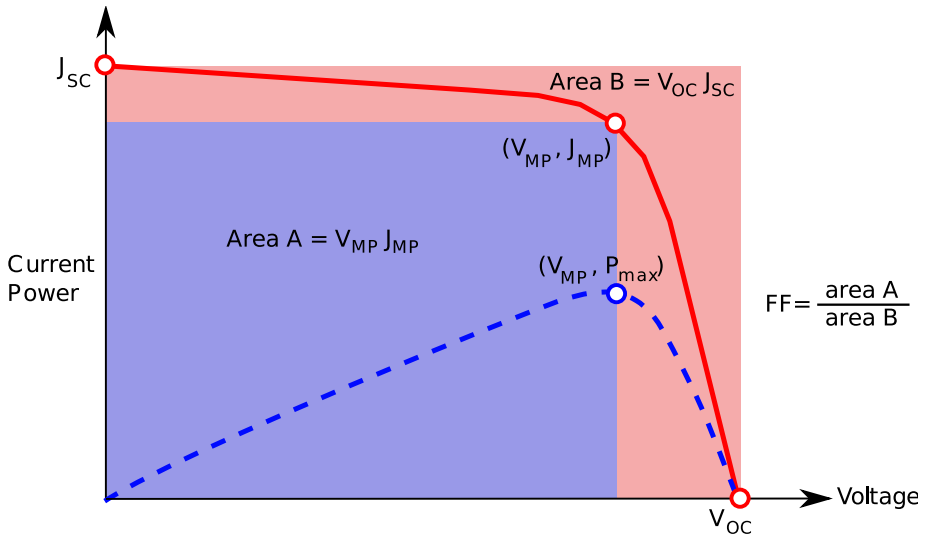

Figure 5.1: Graph of cell output current (solid line) and power (dashed). Points show short-circuit current (J_{sc}), open-circuit voltage (V_{oc}) and maximum power operational point (V_{mp}, I_{mp}).

common current-voltage characteristic for a solar cell under illumination. The short circuit current density J_{sc} is defined as the current density at zero applied bias

when the potential difference between the electrodes is given just by the built-in voltage drop V_{bi}. The open circuit voltage V_{oc} is instead the applied bias at which the photogenerated current equals the injected current and therefore the total current is zero.

We implemented our models using Octave, an open-source language quite popular since it is almost full-compatible with the commercial suite Matlab. This was determined by the availability of some computer code developed in previous works for the generation and handling of meshes (octave package `msh` [19]) and for assembling the matrices resulting from the discretizations determined by EAFE method (package `bim` [18]). Stationary and evolutionary problems are solved respectively with the nonlinear solvers `fsolve` and `daspk`, for details see [13, 49]. Again, in the intent of employing just open-source software, the plots referring to bidimensional simulations were obtained using Paraview, a multi-platform data analysis and visualization application.

5.1 Simulation of DSSC devices

The first set of simulations is aimed to analyze ion mass transport within the cell, the target being to reproduce the results obtained in [61]. A second set of simulations is then performed referring to the complete transport model of Chapter 2 which also includes charge transport by means of electric drift.

5.1.1 Mass transport model

In order to perform an appropriate comparison with the results presented in [61] we use the same values for the model parameters which are reported in Table 5.1. In this analysis we focus our attention on:

- the spatial distribution of ionic species concentrations;
- the influence of the ionic species and of the bulk layer on the cell performance;
- the behavior of saturation current as a function of the bulk layer thickness;
- the effect of the direction of illumination on the current density and the ionic concentrations.

The concentration profiles of the various species resulting from a simulation with output density current set to 160 Am^{-2} are displayed in Fig. 5.2 and they are in complete agreement with Fig. 6 of [61]. The change of porosity between the two regions, gives rise to a discontinuity in the slope of the distribution curves. We observe

Parameter	**Symbol**	**Numerical value**
Initial concentration of iodide	$n^0_{I^-}$	$3.01 \cdot 10^{26}$ m^{-3}, 0.50 mol
Initial concentration of triiodide	$n^0_{I_3^-}$	$2.40 \cdot 10^{25}$ m^{-3}, 0.04 mol
Initial concentration of cations	n^0_C	$3.41 \cdot 10^{26}$ m^{-3}, 0.54 mol
Iodide diffusion constant	D_{I^-}	$3 \cdot 10^{-10}$ $\mathrm{m}^2\,\mathrm{s}^{-1}$
Triiodide diffusion constant	$D_{I_3^-}$	$2.8 \cdot 10^{-10}$ $\mathrm{m}^2\,\mathrm{s}^{-1}$
Porosity	η	0.3
Thickness of TiO_2 layer	l_s	$10 \cdot 10^{-6}$ m
Thickness of bulk layer	l_b	$4 \cdot 10^{-6}$ m
TiO_2 relative dielectric constant	ϵ_s	50
Bulk relative dielectric constant	ϵ_b	36
Temperature	T	298 K

Table 5.1: Model parameters.

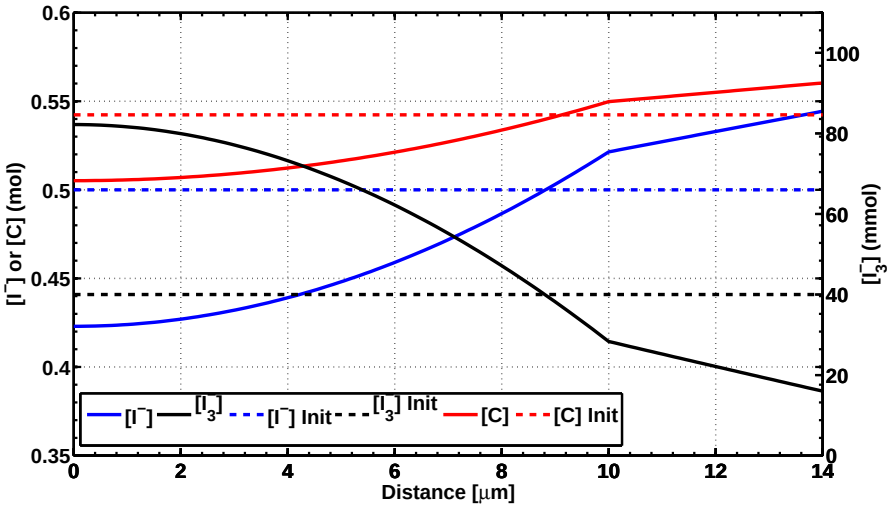

Figure 5.2: Ionic species concentration profiles within the cell with output current of 160 A m^{-2}.

that the concentrations of the ionic species vary with respect to the initial condition under illumination. The reason of this is to be found in the chemical reactions (2.2) and (2.1) that take place within the cell. According to the former, in the vicinity of the porous material, the triiodide is generated and as a consequence its concentration increases while the iodide decreases because it is consumed in the dye regeneration. On the contrary, in the second reaction, the I^- is regenerated at the cathode and its profile increases.

We then focus the investigation on the dependence of ion distributions on the light intensity, or, equivalently for this simplified model, the output density current. We consider three values of this latter, namely 200, 240 and 260 A m^{-2} and the results are shown in Fig. 5.3. We observe that rising the value of the current, the minority species I_3^- has concentrations close to zero at the cathode, resulting in the limitation of the regenerative process of I^-. When this phenomenon occurs the current delivered by the cell saturates to a maximum value called limiting current. This aspect is very important since it highlights that the ionic species I_3^- plays the role of the limiting factor for the performance of the device. A physical motivation has been proposed in [61]. According to this, since the ratio between the initial concentration of triiodide and iodide is 0.08, the majority species could behave as a barrier to the motion of the I_3^-.

The nonuniform distributions of the charged species are responsible for a potential drop and associated electric field within the cell. These quantities are displayed in Fig. 5.4, where we observe that the electric field exhibits a discontinuity at the in-

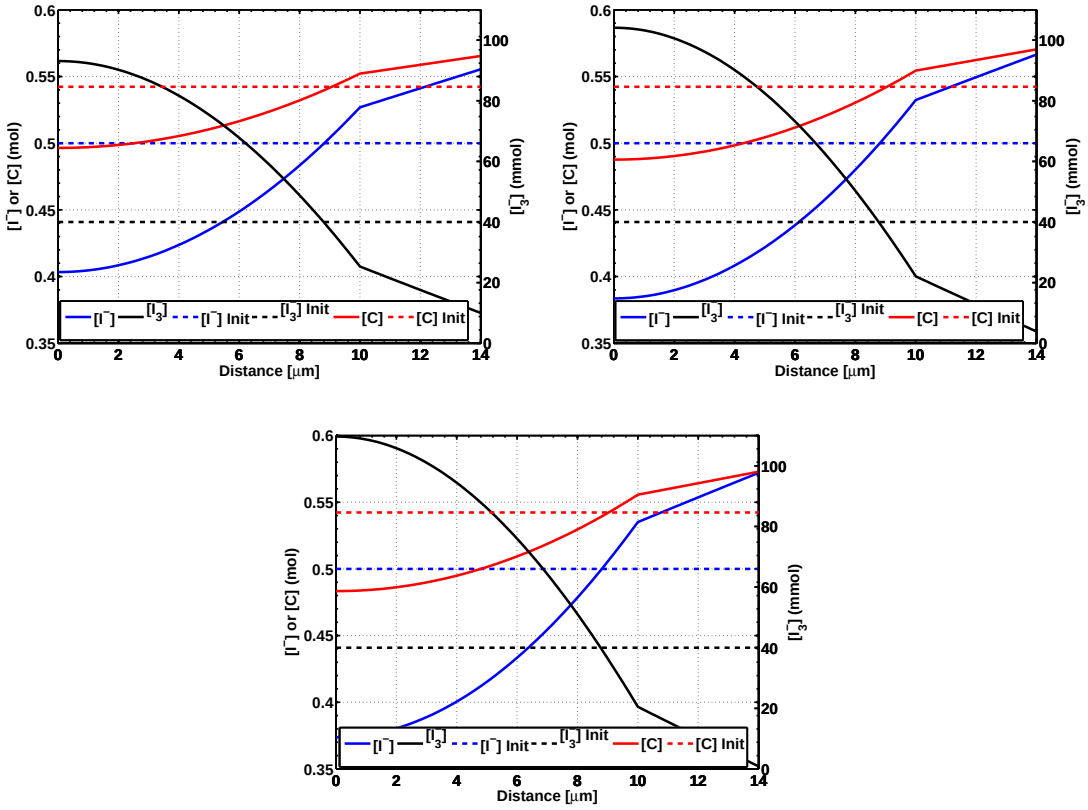

Figure 5.3: Ionic species concentration profiles within the cell with output currents of 200, 240 and 260 mA m^{-2}.

terface between the porous material and the bulk.
The potential and electric field are in absolute value much smaller than the ones that are usually observed in a standard p/n junction device. This has a positive impact on device operation because the ions involved in the reactions are all negatively charged and high values of the electric field would imply migration towards the cathode, in particular for the limiting carrier I_3^-, then limiting the performance of the cell.

The maximum current density is related to the *overpotential* ϕ of the counter electrode, that is the difference in its *electrode potential* between its equilibrium potential and the operating one when a current is flowing. The electrode potential is the electrical potential difference between an electrode and a reference electrode. Instead, the equilibrium potential is the electrical potential of an electrode measured with respect to a reference electrode when there is a current flowing through the electrode. Assuming that the cathode potential is given by the Nernst expression, using the concentration in the vicinity of the counter electrode and taking into account the

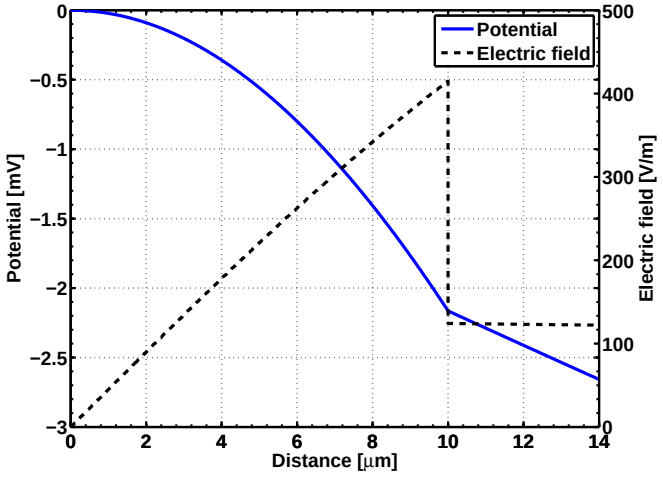

Figure 5.4: Potential and electric field in the cell with an output current of 160 mA m^{-2}.

stoichiometric parameters of (2.1), we have:

$$\phi = \frac{RT}{2F}\left\{\ln\left(\frac{n_{I_3^-}}{n^0_{I_3^-}}\right) - 3\ln\left(\frac{n_{I^-}}{n^0_{I^-}}\right)\right\}, \tag{5.1}$$

where R and F are the gas and Faraday constants respectively. This quantity represents the extra energy needed to force the electrode reaction (2.1) to proceed at a required rate. Consequently, the operating potential of the cathode is always more negative than its equilibrium potential. It is clear from (5.1) that the overpotential decreases when the concentration of $n_{I_3^-}$ tends to zero and this occurs when the current density increases. To study the concentration overpotential we perform a set of simulations focusing on the influence of ionic migration, by either including it in the model or considering pure diffusive transport, and of the presence of a bulk layer. The comparison of the obtained profiles for ϕ is displayed in Fig. 5.5 and again a very close correspondence is achieved with respect to Fig. 6 in [61]. We observe that, as the current density approaches the saturation value, migration plays against performance for both the configurations of cell (with or without bulk layer), decreasing slightly the limiting current. Apart from this, it is important to point out that the inclusion of a bulk layer just 4 μm thick in the structure of the device is sufficient to improve its performance in a considerable way. The increase of saturation current is in fact of about 45% with respect to the case with no bulk layer.

In order to determine the optimal bulk layer length for the considered device we perform a series of simulations modifying the morphology of the cell. In Fig. 5.6 we report the behavior of overpotential as a function of the output current density for several values of the bulk layer thickness in the range between 0.1 and 0.8 μm. By this

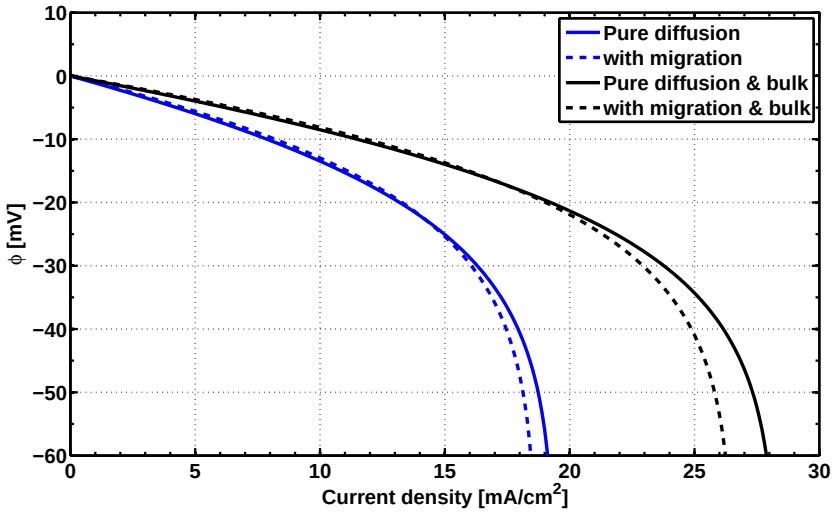

Figure 5.5: Overpotential as a function of output current density for several configurations.

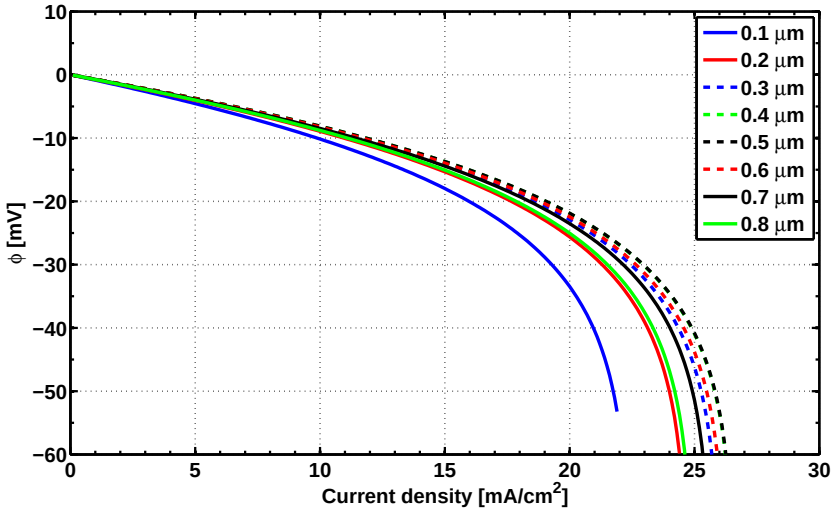

Figure 5.6: Comparison of overpotential for different bulk lengths.

representation it is clear that some configurations are more performing than others and in particular the saturation current does not exhibit a monotone behavior, see Fig. 5.7, showing a maximum for a value around 0.4 μm.

In all the simulations we previously performed, the generation of excited states has been considered constant all over the cell since photon absorption was assumed to be negligible. Now we assume instead that light attenuation occurs inside the cell and we use formula (2.31) for excited states generation. In view of the asymmetry of the cell we expect illumination on either the front electrode and the counter electrode to determine different situations which we refer to as photoelectrode (PE) and cathode (CE) side illumination, respectively.

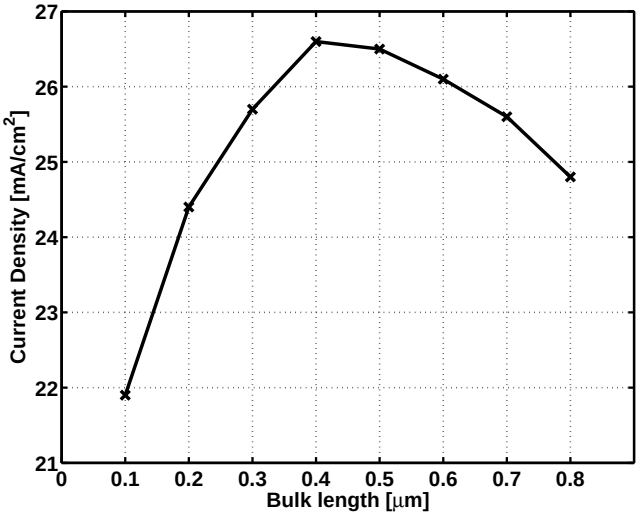

Figure 5.7: Limiting current density as a function of bulk thickness.

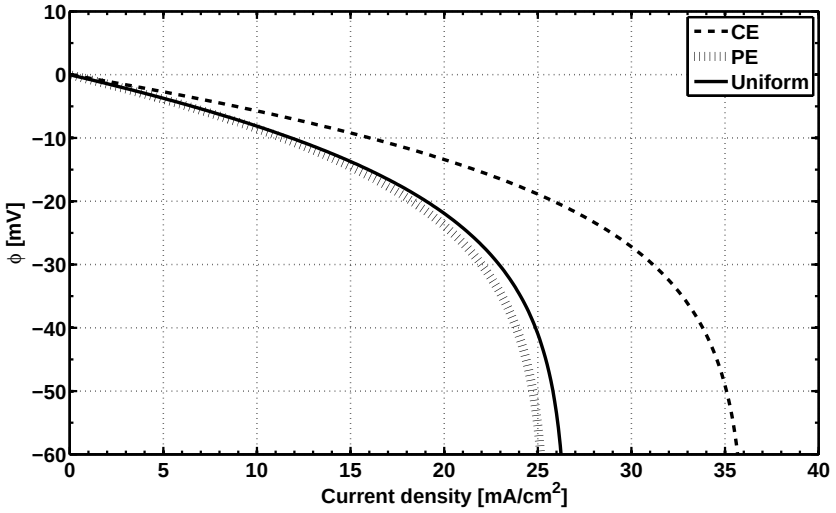

Figure 5.8: Overpotential as a function of the current density for the three modalities of illumination considered.

Using this relation we obtain the results shown in Fig. 5.8, where we compare the overpotential profile and maximum current density delivered by cell with uniform illumination against the other two configurations PE and CE. Results indicate that it is more convenient to irradiate the cell from the cathode since this allows to overcome the problem of the limitation of I_3^- species on the counter electrode.

5.1.2 Model with electrons

In this section we present the results obtained with the complete model described in Chapter 2. The values of model parameters are the same as in Tab. 5.1 and

we add the ones in Tab. 5.2 for the electron part. Here we consider two cases in

Parameter	Symbol	Numerical value
Initial electron concentration	n_e^0	$1 \cdot 10^{16}$ m^{-3}
Electron mobility	μ_e	$3 \cdot 10^3$ m^{2}V^{-1}s^{-1}
Electron recombination constant	k_e	$1 \cdot 10^4$ s^{-1}

Table 5.2: Model parameters to be added in the complete model.

which illumination is applied from either the cathode or the anode with an the electron generation term following formula (2.31). In each of these configurations we simulate the behavior of the cell at short circuit condition and at another one in which a current flows, that is chosen to be 160 A m^{-2} for both illumination profiles. The recombination model we consider is the one defined by (2.32).
We then focus our attention on the analysis of the distributions of the electrons into the semiconductor, see Fig. 5.9. At short circuit condition electron distribution

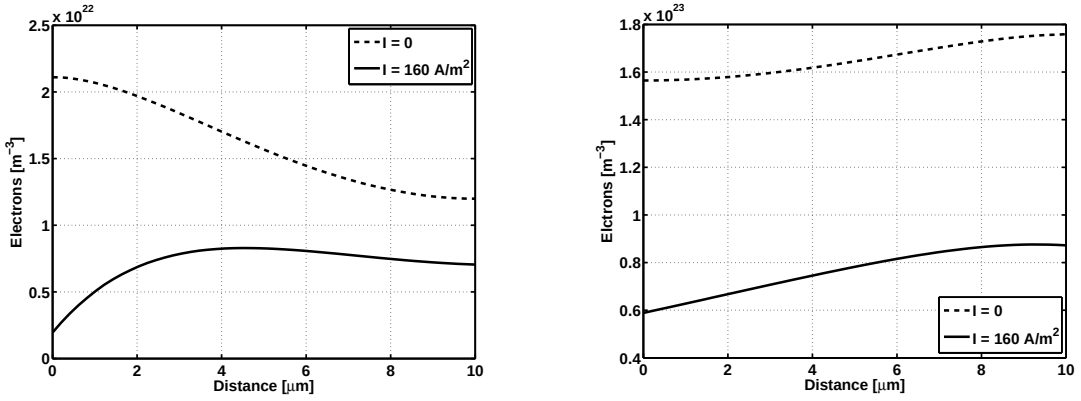

Figure 5.9: Electron concentrations for two different direction of illumination.

results in a non constant profile in both illumination regimes attaining higher values where the peak of generation occurs. The higher slope of the profile in the PE case is a consequence of the fact that electric field driven migration acts on the direction where generation is more intense. In the current flowing condition instead, a very interesting event occurs in the case of PE illumination. Electron density shows a maximum in the area about 4 μm far from the anode, meaning that from there to the interface between the TiO_2 and the bulk layer, diffusion driven transport and electric field migration act in competitive way. Since electric field is known to attain small values in DSSCs, it is most likely that the area of the cell included between 4 and 10 μm is inert with all the generated electrons experiencing recombination.
Since the ionic species concentrations are several orders of magnitude higher than the values we found for the electron density, we can conclude that their distribution are

not affected by the introduction of the electrons into the model. As a consequence, neither the potential nor the electric field are modified in an appreciable way and we do not report them.

5.2 Bulk-heterojunction devices

In this section we present the results of a few simulations we performed considering the model for bulk-heterojunction cells. In any way a detailed analysis of the behavior of this model, performed by testing its sensitivity on the variation of the values for the model parameters, is not the focus of this thesis work. For works oriented in that direction see [44, 20, 20].
Here we considered this model as a mean to introduce ourselves into the field of solar cells, intending to face to it in order to practice on a well known problem. Moreover, another 1D code implementing this model is already existing so we used the problem as a testing ground for our 2D code by performing a comparison of the results. For this reason, since we are not interested in a detailed description of the phenomena, we consider simplified constant model parameters and Dirichlet boundary conditions in the form (3.13) that represent a good compromise in terms of mathematical complexity and modeling power. We set model parameters to the values shown in Table 5.3 and calculations are performed for two situations differing for the exciton generation rates, namely equal to $4.3 \cdot 10^{26}\,\mathrm{m^{-3}s^{-1}}$ and $4.3 \cdot 10^{30}\,\mathrm{m^{-3}s^{-1}}$, under short circuit condition, simulating the transient of the cell in the time interval $(0, T)$ with $T = 10\,\mu\mathrm{s}$ with an initial time step of $10^{-9}\,\mathrm{s}$. Results for the electron and exciton densities at several time steps are reported in Fig. 5.10. Since model parameters are set to the same values for both positive and negative carriers, the results relative to

Parameter	**Symbol**	**Numerical value**
Conduction band states density	N_C	$10^{27}\ \mathrm{m^{-3}}$
Valence band states density	N_D	$10^{27}\ \mathrm{m^{-3}}$
Temperature	T	298 K
Built-in voltage	V_{bi}	0.5 V
Blend relative dielectric constant	ε_r	4
Electron mobility	μ_n	$2 \cdot 10^{-8}\ \mathrm{m^2\,V^{-1}\,s^{-1}}$
Hole mobility	$\mu_{0,p}$	$2 \cdot 10^{-8}\ \mathrm{m^2\,V^{-1}\,s^{-1}}$
Bimolecular recombination constant	γ	$1.8182 \cdot 10^{16}\ \mathrm{m^3\,s^{-1}}$
Exciton dissociation rate	k_{diss}	$2.588 \cdot 10^{6}\,\mathrm{s^{-1}}$
Exciton recombination rate	k_{rec}	$1 \cdot 10^{6}\,\mathrm{s^{-1}}$
Cathode injection barrier height	ϕ^c_{bn}	0.5 eV
Anode injection barrier height	ϕ^a_{bp}	0.5 eV
Space scaling	$\overline{L}$	$70 \cdot 10^{-9}$ m
Carrier scaling	$\overline{n}$	$1 \cdot 10^{27}\ \mathrm{m^{-3}}$

Table 5.3: Model parameters.

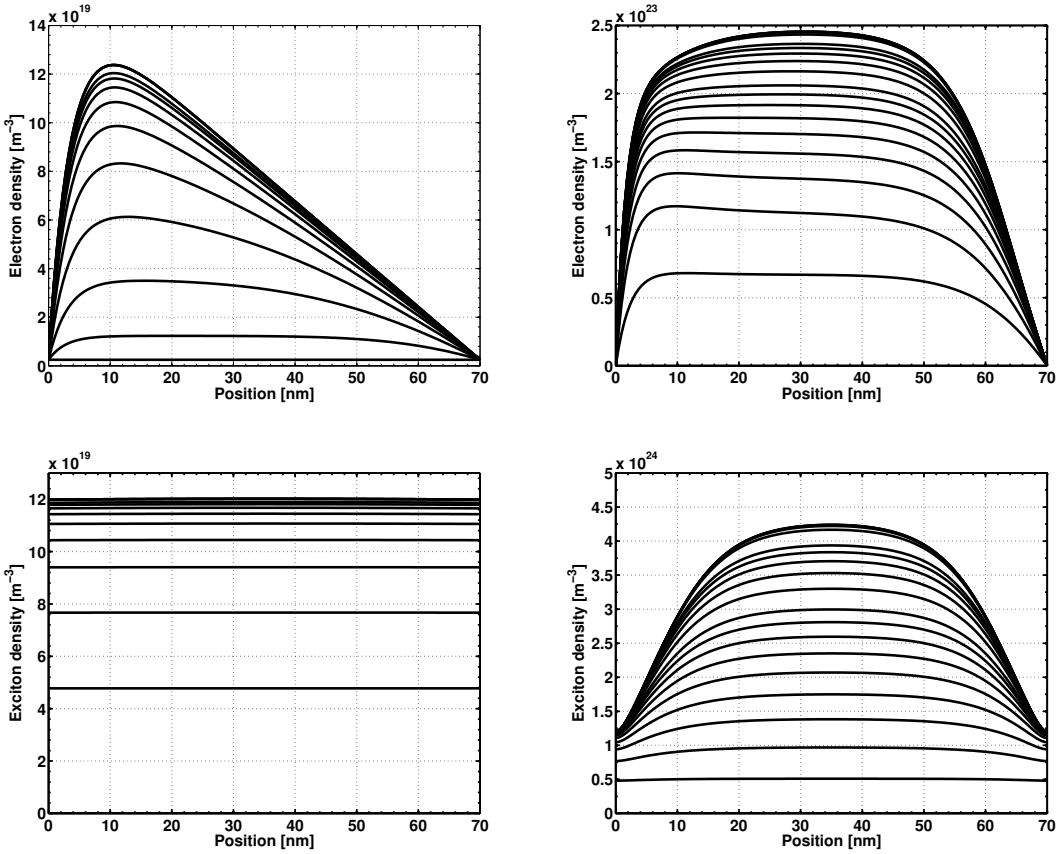

Figure 5.10: Electron and exciton densities with exciton generation rate $G = 4.3 \cdot 10^{26}\,\mathrm{m^{-3}s^{-1}}$ (left) and $G = 4.3 \cdot 10^{30}\,\mathrm{m^{-3}s^{-1}}$ (right) at short circuit conditions.

the holes exhibit exactly the same behavior as electrons with a reflection along the central vertical axis and for this reason we omitted their representation. We highlight the difference in the orders of magnitude of the densities in the two cases, that is due precisely for the different values of exciton generation. Also the qualitative profile vary in a significant way, in particular for the electron density a maximum close to the harvesting electrode can be clearly delineated at light illumination intensity while in other condition electrons are more distributed along the cell. The reason of this has to be found in bimolecular recombination. In fact, in the first case low densities bring to minimal recombination events and hence most of the generated electrons are successfully driven to the cathode. In the other case, in which densities are much higher and so recombination events, the number of electrons is somehow limited bringing to flatter profiles.

In Fig. 5.11 we report the photocurrent transients for the cell under the irradiation conditions considered. Values of about 3.2 and 8500 $\mathrm{Am^{-2}}$ for the current are obtained at stationary regime which is reached in a very short time.

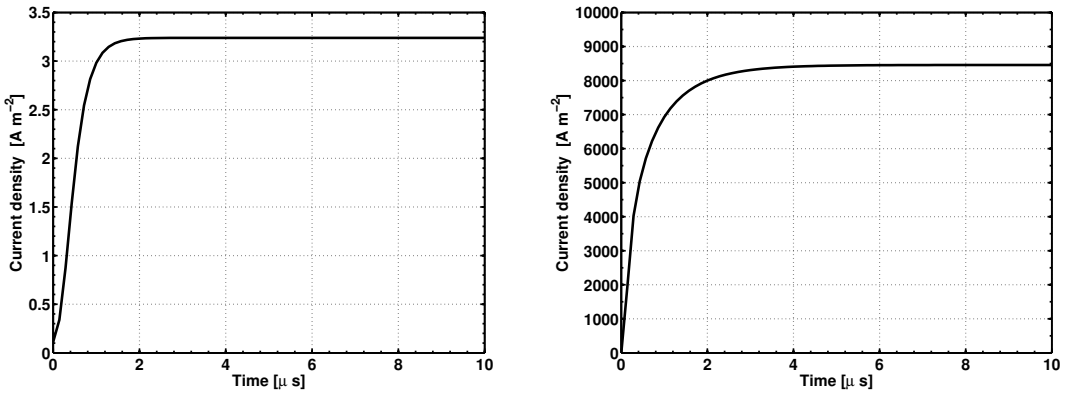

Figure 5.11: Photocurrent transient for generation rate values of $G = 4.3 \cdot 10^{26}\,\mathrm{m}^{-3}\mathrm{s}^{-1}$ (left) and $G = 4.3 \cdot 10^{30}\,\mathrm{m}^{-3}\mathrm{s}^{-1}$ (right) at short circuit conditions.

5.3 Nanostructured heterojunction devices

The first set of simulations is aimed to verify the consistency of the results of our model with respect to what is reported in the main works in literature on the subject. To be more precise, we consider references [78, 77] and we try to reproduce some of the graphs proposed therein describing carrier densities, electric field and current-voltage characteristics.

Since charge generation is enhanced with high contact surfaces and transport is promoted by regular paths towards the electrodes, we consider the ideal morphology for the device, shown in Fig. 5.12. The same geometry was used in [78, 77], and in a previous work [14] it has been shown to be more efficient than both planar bilayer and bulk-heterojunction structures. Since the interface pattern of Fig. 5.12(left) can be seen as the periodic reflection of the geometric module, shown in Fig. 5.12(righ), we consider the latter as the computational domain, applying periodic conditions on the artificial boundary Γ_N. In this way the algebraic systems to be solved will be much smaller with a consequent reduction of cpu-time needed.
In Table 5.4 we report the values of the model parameters we used in the simulation that, in order to perform an appropriate comparison, are taken from [78, 77]. In Table 5.6, instead, the geometrical details of the morphology of the device are shown. We define 1 Sun the power density in the range 459-460 nm in the AM 1.5 spectrum, that is the solar spectrum after the solar radiation has traveled through the

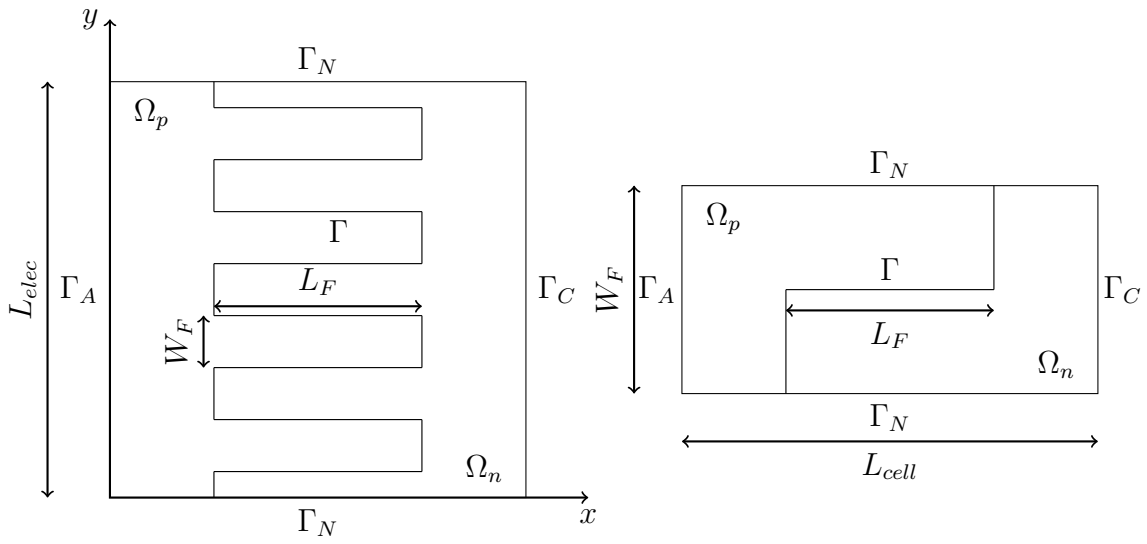

Figure 5.12: Geometry of the considered device and representation of unit domain module on which simulations are carried out.

atmosphere. We also consider the cells of our simulations to be illuminated with monochromatic light of that wavelength and this, in the case of 1 Sun irradiation, is equivalent to an incident intensity of $2.3 \cdot 10^{18}$ $\mathrm{m^{-1}s^{-1}}$. Since the cell we analyzed in the first case is 150 nm thick, the corresponding exciton generation parameter G is equal to $1.53 \cdot 10^{25}$ $\mathrm{m^{-3}s^{-1}}$.

We consider three operation conditions characterized by different applied potentials, namely short circuit ($V_{appl} = 0$), flat-band ($V_{appl} = V_{bi}$) and another one very close to open circuit with $V_{appl} - V_{bi} = 0.3$ V. The results for the charge carrier densities and the x-component of the electric field are reported in Fig. 5.13 and they show a complete agreement with the corresponding ones of Fig. 3.55 in [77]. At short circuit, carrier densities are relatively low and E_x is approximately constant to the value for zero field screening,

$$E_{con} = (V_{appl} - V_{bi})/L_{cell} = -4 \ \mathrm{MVm^{-1}}.$$

At flat band condition the peaks of charge carrier densities are similar in magnitude to the ones for short circuit, but depletion in the area of the electrodes is much more visible. For this reason and because the electrodes are at the same potential, the magnitude of the field is small. At the situation close to open circuit, instead, densities are significantly increased and this is the consequence of charge injection from the electrodes. In Fig. 5.14 we report the y-component of the electric field and it is possible to appreciate that the qualitative behavior is the same for all the configurations, with a rapid change of sign across the interface. Its magnitude instead, while being negligible at short circuit, increases with V_{appl} and for values close to V_{oc}

is of the same order as E_x.

We now want to obtain the current density characteristics of another device considered in [78, 77] that differs from the one of the previous simulations in the length of the electrodes and the finger width, see Table 5.6 for details. The current values are obtained performing a series of simulations for a several number of applied voltages in the range between 0V and the maximum value at which convergence is reached by the numerical method. We also tried to implement the model by Williams and Walker [77], following the details reported therein, and the comparison between the outputs of the two models is shown in Fig. 5.15. The behaviors are in very close agreement especially for an applied voltage between V_{bi} and V_{oc}, that in this case assumes the value of 0.87 V. The current decreases with the increase of applied bias because the electric field is increasing, which, in turn, reduces polaron pair dissociation, see Section 3.3.3. In addition, for a bias above V_{bi}, there will be a significant

Parameter	**Symbol**	**Numerical value**
Acceptor relative dielectric constant	$\varepsilon_{r,a}$	4
Donor relative dielectric constant	$\varepsilon_{r,d}$	4
Built-in voltage	V_{bi}	0.6 V
Temperature	T	298 K
Electron zero-field mobility	$\mu_{0,n}$	$3 \cdot 10^{-10}$ $\mathrm{m^2\,V^{-1}\,s^{-1}}$
Hole zero-field mobility	$\mu_{0,p}$	$1 \cdot 10^{-10}$ $\mathrm{m^2\,V^{-1}\,s^{-1}}$
Acceptor mobility material parameter	γ_a	$1.55 \cdot 10^{-4}$ $\mathrm{V^{-1/2}\,m^{1/2}}$
Donor mobility material parameter	γ_d	$3 \cdot 10^{-4}$ $\mathrm{V^{-1/2}\,m^{1/2}}$
Cathode injection barrier height	ϕ^c_{bn}	0.5 eV
Anode injection barrier height	ϕ^a_{bp}	0.5 eV
Exciton diffusion	D_S	$1 \cdot 10^{-7}$ $\mathrm{m^2 s^{-1}}$
Exciton decay time	$\tau_{S,dec}$	$1 \cdot 10^{-9}$ s
Exciton dissociation time	$\tau_{S,diss}$	$1 \cdot 10^{-12}$ s
Polaron pair recombination rate	k_{rec}	$1 \cdot 10^{6}$ $\mathrm{s^{-1}}$
Polaron pair zero-field dissociation rate	$k_{0,diss}$	$1 \cdot 10^{5}$ $\mathrm{s^{-1}}$
Active layer half-width	H	$1 \cdot 10^{-9}$ m
Conduction band states density	N_C	10^{27} $\mathrm{m^{-3}}$
Valence band states density	N_D	10^{27} $\mathrm{m^{-3}}$
Space scaling	$\overline{L}$	$150 \cdot 10^{-9}$ m
Carrier scaling	$\overline{n}$	$1 \cdot 10^{22}$ $\mathrm{m^{-3}}$
Exciton scaling	$\overline{X}$	$1 \cdot 10^{12}$ $\mathrm{m^{-2}}$

Table 5.4: Model parameters with units and values.

Size	Symbol	Numerical value
Cell length	L_C	$150 \cdot 10^{-9}$ m
Electrode length	L_{elec}	$440 \cdot 10^{-9}$ m
Finger length	L_F	$79 \cdot 10^{-9}$ m
Finger width	W_L	$55 \cdot 10^{-9}$ m

Table 5.5: Geometrical parameters of the cell relative to the first series of simulations.

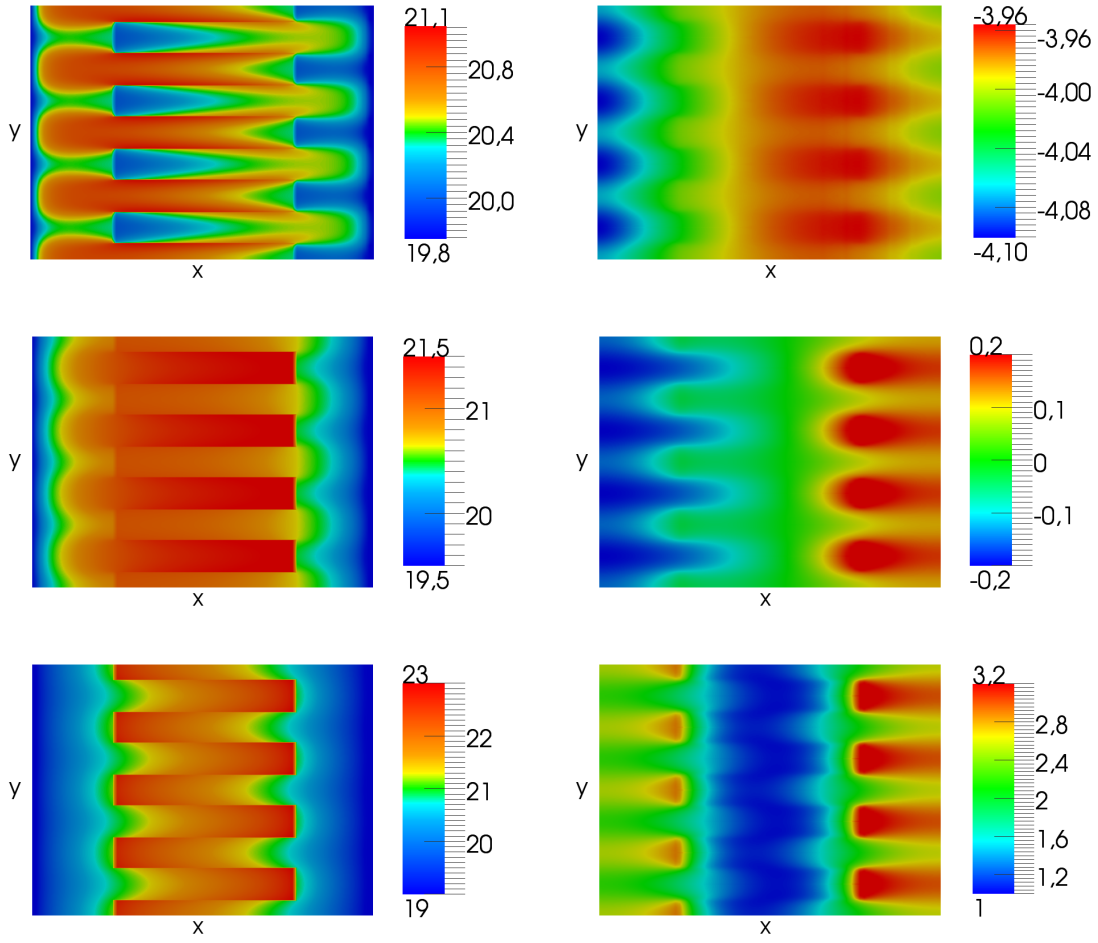

Figure 5.13: Color plots for base 10 logarithm of charge carrier densities [m^{-3}] (left column) and for the x-component of the electric field [MVm^{-1}] under 1 Sun illumination. From the top to the bottom, the applied voltages are, $V_{appl} = 0$, $V_{appl} = V_{bi}$ and $V_{Appl} = V_{bi} + 0.3$ V.

amount of charge injected into the device, increasing recombination and hence reducing the current. The predicted values for the short circuit current are respectively for the two models 1.25 and 1.28 mAm^{-2} that is a small difference just about 2%. This is most probably due to the different assumptions that are stated in the models

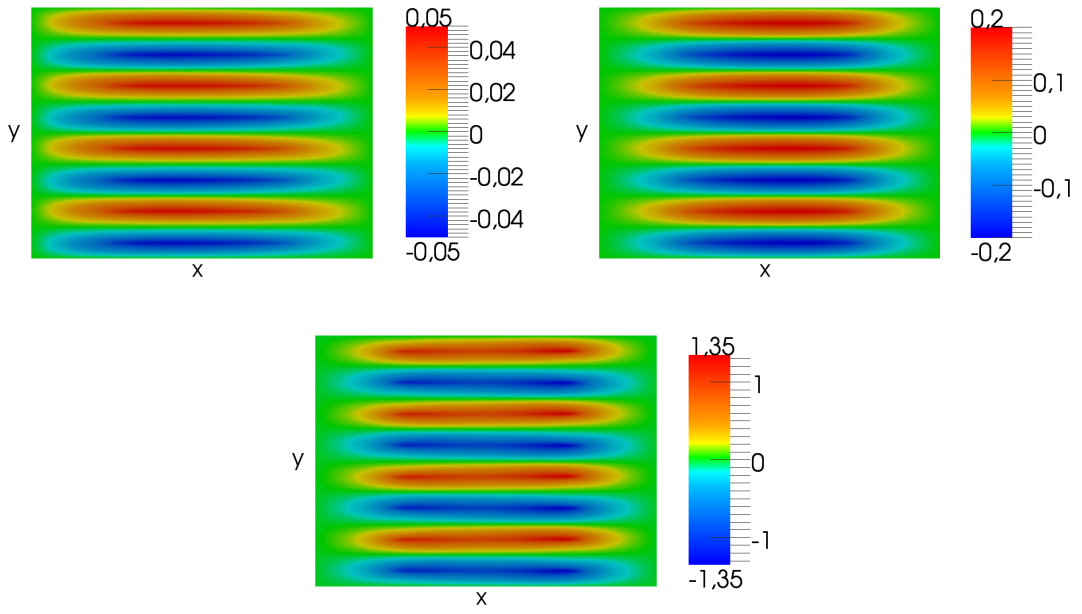

Figure 5.14: Color plots for the y-component of the electric field [MVm^{-1}] under 1 Sun illumination at applied voltages $V_{appl} = 0$, $V_{appl} = V_{bi}$ and $V_{Appl} = V_{bi} + 0.3$ V.

Size	Symbol	Numerical value
Cell length	L_C	$150 \cdot 10^{-9}$ m
Electrode length	L_{elec}	$50 \cdot 10^{-9}$ m
Finger length	L_F	$79 \cdot 10^{-9}$ m
Finger width	W_L	$6.25 \cdot 10^{-9}$ m

Table 5.6: Geometrical parameters of the cell relative to the second series of simulations.

regarding the transition phenomena from exciton to polaron state at the interface. While in [77, 78] complete quenching of excitons at the interface is assumed, and is obtained by imposing the density to be null there, in our model conditions (3.27) lead to non null values and hence to a slightly reduced production of polarons, that in turn determines less charge dissociation.

Taking into consideration the same device, we obtained the current-voltage characteristics for several irradiation conditions, extending the range of applied biases to the negative ones. We remark that the values well above 1 Sun, that could at first sight seem unfeasible and considered just as numerical exercises to test the behavior of the method, are actually achievable by using concentrating photovoltaic systems. We expect saturation to occur at negative applied biases and this behavior is actually reproduced by our model, see Fig. 5.16, with the saturation currents J_0 showing

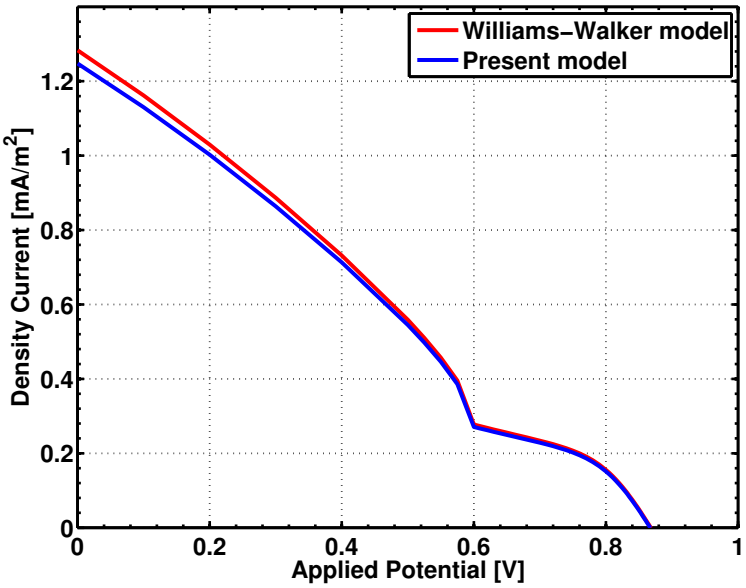

Figure 5.15: Comparison of the current-voltage characteristic lines obtained with our model and Williams-Walker one.

a non linear increase with the logarithm of the incident power. This is a consequence of the phenomenon of bimolecular recombination of electrons and holes that is greatly enhanced for intense illumination in the locations where charge densities attain high values. Again in Fig. 5.16 the open circuit voltage increases linearly with

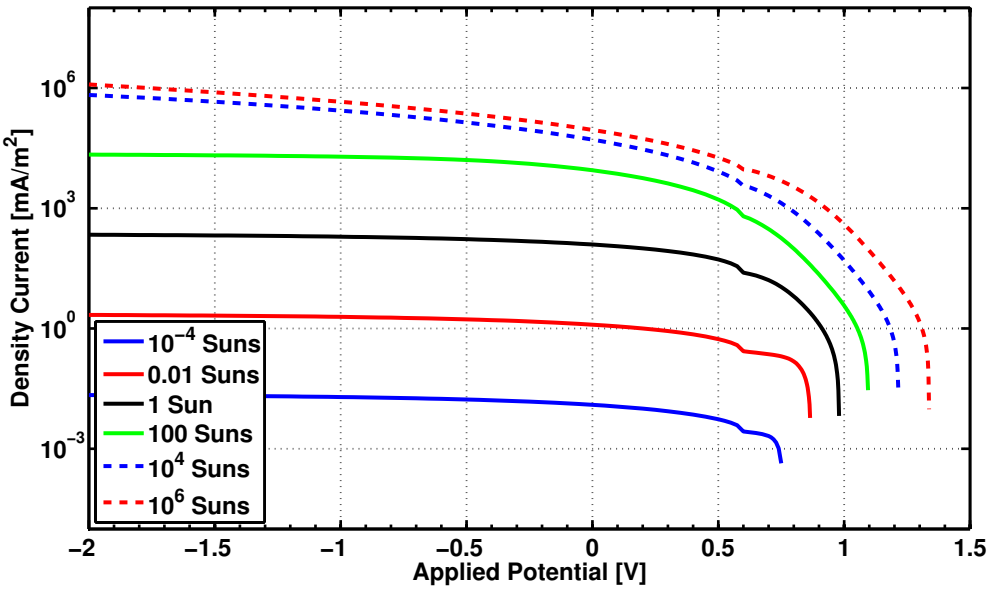

Figure 5.16: Current-voltage characteristic lines for various values of incident light.

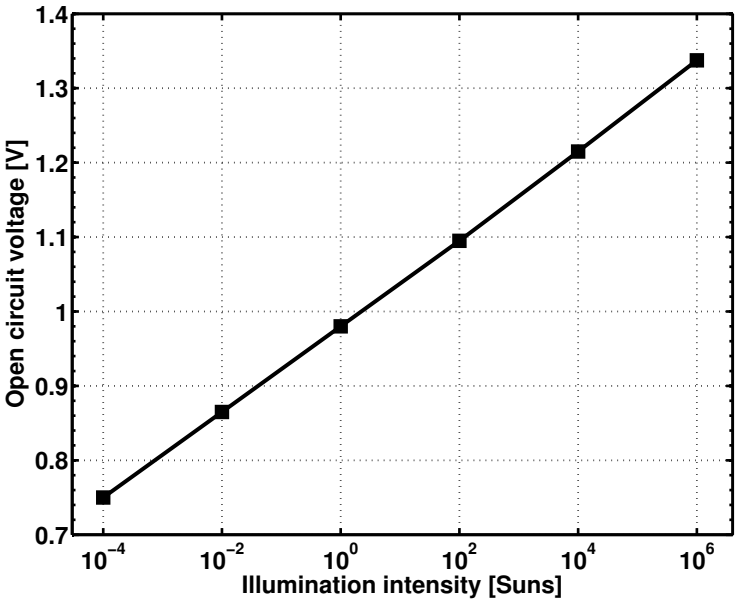

Figure 5.17: Open circuit voltage as a function of illumination intensity.

the logarithm of light irradiation and this behavior is better reproduced in Fig. 5.17.

In addiction, for a deeper comprehension of the information given by the current-voltage characteristics, we consider the *internal quantum efficiency* η_{IQE}, that is the ratio between the number of electrons injected in the external circuit and the number of absorbed photons

$$\eta_{IQE} = \frac{\text{number of electrons injected in the external circuit}}{\text{number of absorbed photons}} = \frac{J}{qL_{cell}G}, \qquad (5.2)$$

and that can be interpreted as a measure of the ability of the cell in generating photocurrent from the photons that are successfully absorbed by the materials. We consider a cell with the geometrical characteristics reported in Table 5.4 and a range of illumination intensities from 10^{-4} to 10^{4} Suns and we obtain the results of Fig. 5.18. With irradiations up to 1 Sun the cell presents high internal quantum efficiency for almost the entire range of the considered applied voltages since the dissociation of excitons is performed efficiently and their decay has a limited impact for the relatively low densities. Only in situations close to open circuit efficiency decreases since the unfavorable electric field promotes charge recombination and reduces the polaron pair dissociation. The behavior at high light intensity is instead very different, showing at 100 Suns a decrease even before short circuit and values below 5% all-over the voltage range for 10^{4} Suns. In this latter case the reason of such low values is to be found in the decay of excitons to the ground state that is a consequence of their high density. At 100 Suns, instead, the negative impact of

the electric field is the main reason of the reduction of the cell performance since it dampens the dissociation rate of polaron pairs.

Before focusing on other investigations, we conclude the comparison between the models showing that the one proposed in this thesis is asymptotically equivalent to the one of [78, 77] in the limit $\tau_{S,diss} \to 0$. As a matter of fact, in [78, 77] instantaneous transition of excitons into polaron pairs is assumed and values of the polaron pair creation characteristic time closer and closer to zero approximate this behavior. To support this statement, in Fig. 5.19 we report the results of a series of simulations in which the parameter $\tau_{S,diss}$ is taken in the range 10^{-21}~10^{-9}, and compared to the profile obtained with the Williams-Walker model. All the parameters are set to the values used in the previous simulations, the cell is 150 nm thick and the illumination considered is 1 Sun. Numerical results are in agreement with our expectations since the values of the solution on the interface (which is located in $x = 75$ nm) approach zero with decreasing $\tau_{S,diss}$.

We then shift the analysis on the impact that morphology has on the performance of the cell and in order to do so, we consider a reference square-shaped device with side length of 150 nm, illuminated at 1 Sun. We perform two series of simulations in which the number of fingers in the cell, i.e. the width of each of them, and their

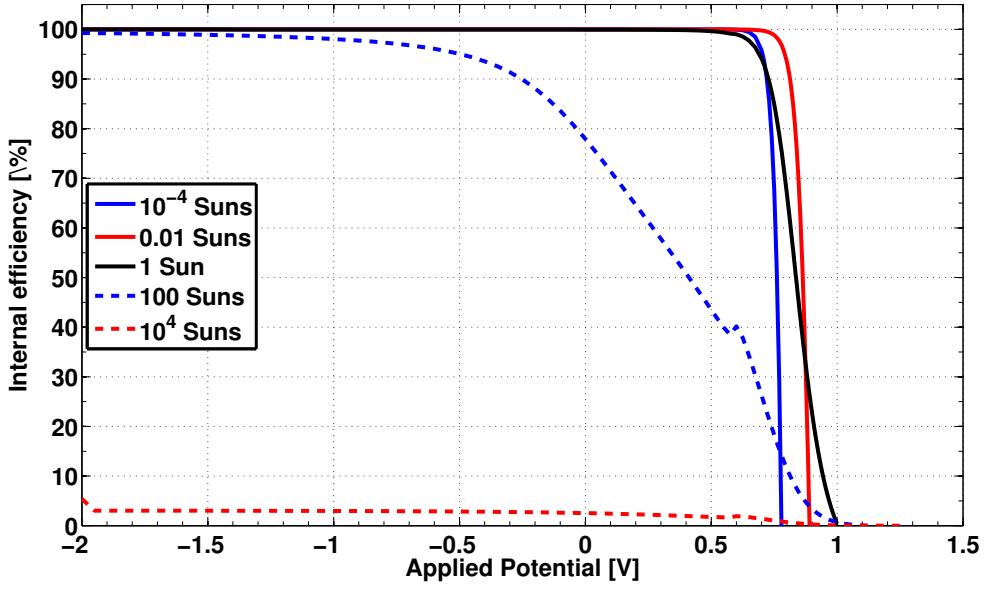

Figure 5.18: Internal quantum efficiency as a function of applied voltage for several values of light intensity.

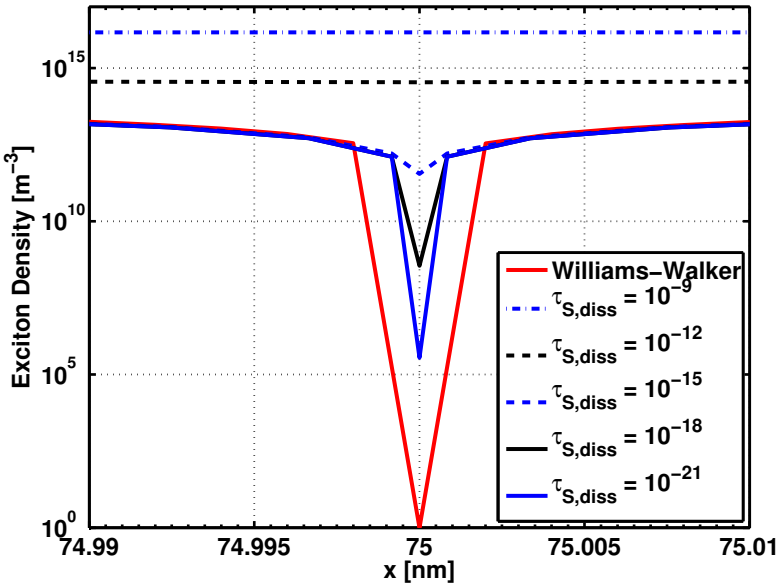

Figure 5.19: Zoom of exciton density (base 10 log scale) in the area across the interface in a biplanar device, for the Williams-Walker model and the one proposed in this thesis, for several values of $\tau_{S,diss}$.

length are respectively varied. In both these ways the contact area between donor and acceptor is increased, keeping constant the dimensions of the device, and we expect this to enhance the chance for excitons to reach a dissociation site. Nevertheless we are also aware that more interface could lead to more recombination events and thus to a saturation of the output current.

We first analyze the response of the output current when increasing the photoactive interface area by diminishing the width of the rods. The limiting configurations are the biplanar one and one with 15 rods of each material. This latter is known to be beyond the limit of current technology since at this day nanostructures with 10 nm length scale (7-8 fingers in our case) represent the best achievable result [54]. We refer to each morphology by means of the parameter N which is the number of rods of each material and we set the rod-length to the value 79 nm that we always used in the previous simulations. The results are reported in Fig. 5.20. As we expected, the biplanar configuration in the less performing one and the output current increases monotonically with the number of nodes. Again, in accordance with the second of our guesses, current experiences saturation with a high number of rods and to support this we also present the calculated exciton densities in Fig. 5.21. If compared to the situation relative to the biplanar device, top-left in Fig. 5.21, densities in interdigitated structures attain lower values as a consequence of the boosted transition to polarons and in particular it is difficult for them to diffuse in the areas between the

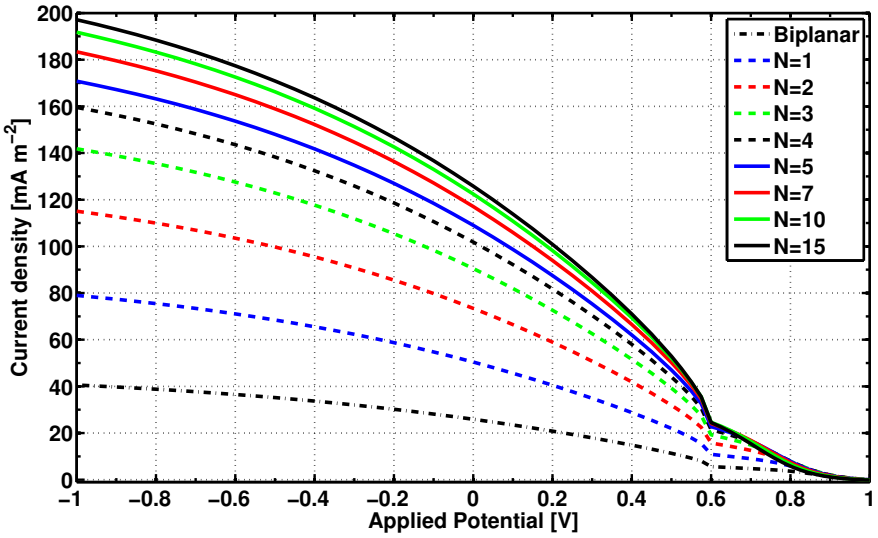

Figure 5.20: Current voltage characteristics for acceptor-donor interpenetrating morphologies with rods of various width.

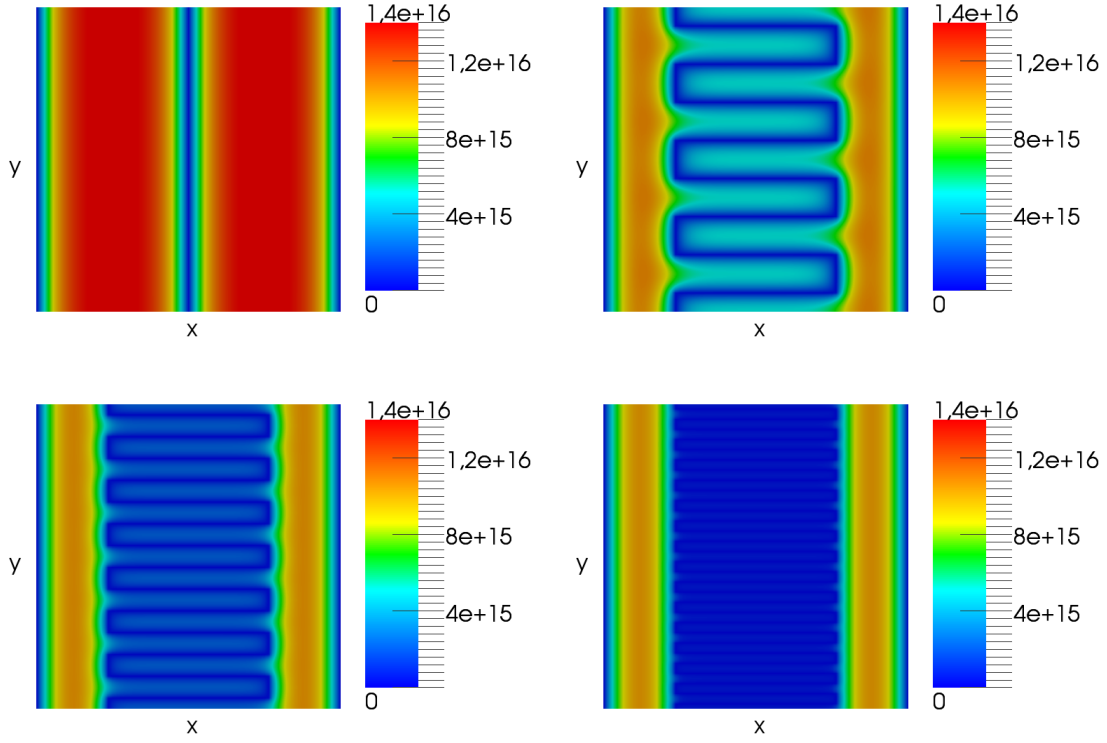

Figure 5.21: Color plots for the exciton density [m^{-3}] under 1 Sun illumination at short circuit $V_{appl=0}$ with several morphologies, biplanar and $N = 4, 7, 15$.

fingers. Hence, most part of the active sites do not experience high exciton flux and the number of generated polarons is limited, leading to saturation of the current.

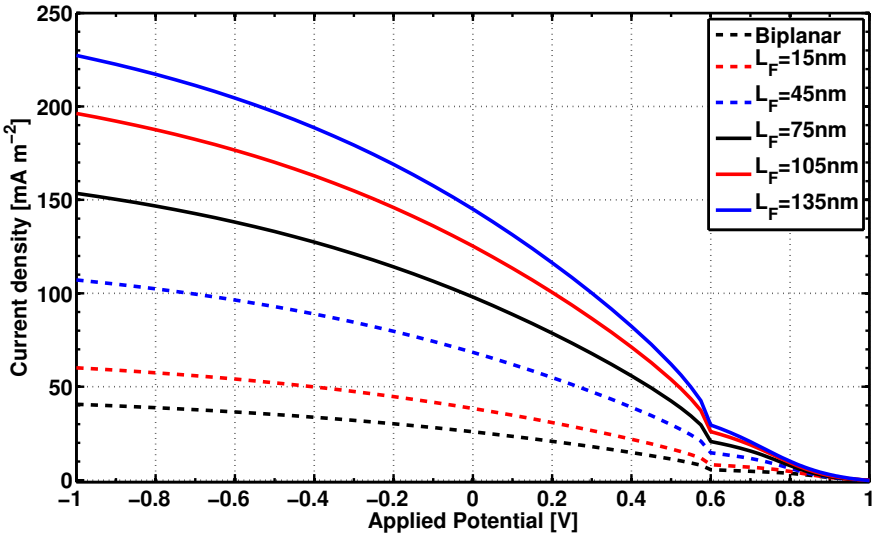

Figure 5.22: Current voltage characteristics for acceptor-donor interpenetrating morphologies with rods of various length.

Anyway we highlight that the current voltage characteristic relative to the configuration with rods approximately 10 nm wide, is very close to the ones with more complex morphologies and hence the achievable improvement employing such modifications would be very limited.

We finally analyze the other strategy aimed to increase the interface area and we consider a morphology consisting in two layers that interpenetrate with four rods each of length that varies from 0 (biplanar device) to 90% of the device length L_{cell}. Results are shown in Fig. 5.22 and once again the simulated behavior is consistent with our prediction. Current increases linearly with the length of the rods, and hence with the interface length, since this latter is given by the formula

$$L_{int} = L_{elec} + 2L_F.$$

A lower increase in output current can be obtained with finger lengths approaching L_{cell} but this is far from the saturation phenomenon observed for the other set of simulations.

Chapter 6

Concluding remarks and future work

The present Master thesis work has been focused on the mathematical modeling and numerical simulation of third generation solar cell. Various models proposed in literature have been analyzed, some improvements have been successfully implemented and numerical simulations helped to understand in deeper detail the influence of parameters and phenomena on the cell performance.
Future research is warranted in order to achieve full description of the behavior of these complex devices. In particular the following issues deserve highest priority in the effort for improving the physical accuracy of the models:

- as the structures under the consideration have geometrical features of size comparable with the wavelengths in the visible spectrum, a full description of the distribution of electromagnetic radiation energy in the device would be included to accurately predict the absorption rates and thus efficiency;
- a thorough comparison of numerical simulation results to experimental data in order to fully validate the models and calibrate the parameters.

More in detail, for the model relative to the DSSCs some possible improvements are:

- transient simulations would be useful to estimate the effect of trap assisted charge transport and quantitatively the rates of all chemical reactions occurring in the electrolyte;
- a rigorous derivation of porosity dependent transport coefficients via homogenization procedures would be in order;
- multidimensional simulations needed to address devices with ordered nanostructured morphology, would require to reformulate the models so that all reactions are localized at the material interfaces.

On the side of OSCs further activity could deal with:

- constitutive relations for model parameters are still subject of active research, a systematic set of simulation to compare the various models and to assess this properties in term of physical accuracy and numerical efficiency would be in order.
- energetic disorder and its impact on charge injection and transport has been so far neglected in our simulation, but has been shown in the literature to have non-negligible impact on device performance.

Bibliography

[1] International Energy Agency. 2010 key world energy statistics. Technical report, 2010.

[2] U.M. Ascher and L.R. Petzold. *Computer methods for ordinary differential equations and differential-algebraic equations*. Society for Industrial Mathematics, 1998.

[3] P. Atkins. *Physical Chemistry*. Oxford University Press, 2002.

[4] R.E. Bank, J.F. Bürgler, W. Fichtner, and R.K. Smith. Some upwinding techniques for finite element approximations of convection-diffusion equations. *Numerische Mathematik*, 58(1):185–202, 1990.

[5] R.E. Bank, W.M. Coughran Jr, and L.C. Cowsar. The finite volume Scharfetter-Gummel method for steady convection diffusion equations. *Computing and Visualization in Science*, 1(3):123–136, 1998.

[6] J.A. Barker, C.M. Ramsdale, and N.C. Greenham. Modeling the current-voltage characteristics of bilayer polymer photovoltaic devices. *Physical Review B*, 67:075205 (9pp), 2003.

[7] C. Bauer, G. Boschloo, E. Mukhtar, and A. Hagfeldt. Interfacial electron-transfer dynamics in Ru(tcterpy)(NCS)3-sensitized TiO_2 nanocrystalline solar cells. *Appl. Phys. Lett.*, 48:183, 1986.

[8] E. Becquerel. Recherches sur les effets de la radiation chimique de la lumiere solaire, au money des courants electrique. *C.R. Acad. Sci.*, 9:145–149, 1839.

[9] M. Berginc, M. Filipič, U.O. Krašovec, M. Nerat, A. Čampa, M. Hočevar, F. Smole, and M. Topič. *Electrical Model of Dye-Sensitized Solar Cells*. 2009.

[10] J. Bisquert, D. Cahen, G. Hodes, S. Ruehle, and A. Zaban. Physical chemical principles of photovoltaic conversion with nanoparticulate, mesoporous dye-sensitized solar cells. *J. Phys. Chem. B*, 108(24):8106–8118, 2004.

[11] C.L. Braun. Electric field assisted dissociation of charge transfer states as a mechanism of photocarrier production. *The Journal of Chemical Physics*, 80:4157, 1984.

[12] A.N. Brooks and T.J.R. Hughes. Streamline upwind/Petrov-Galerkin formulations for convection dominated flows with particular emphasis on the incompressible Navier-Stokes equations. *Computer methods in applied mechanics and engineering*, 32(1-3):199–259, 1982.

[13] P.N. Brown, A.C. Hindmarsh, and L.R. Petzold. A description of DASPK: A solver for large-scale differential-algebraic systems. *Lawrence Livermore National Report UCRL*, 1992.

[14] G.A. Buxton and N. Clarke. Computer simulation of polymer solar cells. *Modelling Simul. Mater. Sci. Eng.*, 15:13–26, 2007.

[15] D. Cahen, G. Hodes, M. Gratzel, J.F. Guillemoless, and I. Riess. Nature of photovoltaic action in dye-sensitized solar cells. *J. Phys. Chem. B*, 104(9):2053–2059, 2000.

[16] J. Campbell Scott and G.G. Malliaras. Charge injection and recombination at the methal-organic interface. *Chemical Physics Letters*, 299:115–119, 1999.

[17] K.M. Coakley and M.D. McGehee. Conjugated polymer photovoltaic cells. *Chemistry of Materials*, 16(23):4533–4542, 2004.

[18] C. de Falco and M. Culpo. bim octave-forge package. `http://octave.sourceforge.net/bim/index.html`.

[19] C. de Falco and M. Culpo. msh octave-forge package.

[20] C. de Falco, R. Sacco, and M. Verri. Analytical and numerical study of photocurrent transients in organic polymer solar cells. *Computer Methods in Applied Mechanics and Engineering*, 199(25-28):1722 – 1732, 2010.

[21] L.J. Durlofsky, B. Engquist, and S. Osher. Triangle based adaptive stencils for the solution of hyperbolic conservation laws. *Journal of Computational Physics*, 98(1):64–73, 1992.

[22] J.R. Durrant, S.A. Haque, and E. Palomares. Photochemical energy conversion: from molecular dyads to solar cells. *Chemical communications*, 2006(31):3279–3289, 2006.

[23] M. Favino. Mathematical modeling and numerical simulation of third generation solar cells. Master's thesis, Politecnico di Milano, 2008-2009.

[24] J. Ferber and J. Luther. Computer simulations of light scattering and absorption in dye-sensitized solar cells. *Solar Energy Materials and Solar Cells*, 54(1-4):265–275, 2004.

[25] J. Ferber, R. Stangl, and J. Luther. An electrical model of the dye-sensitized solar cell. *Solar Energy Materials and Solar Cells*, 53(1-2):29–54, 1998.

[26] A.C. Fisher, L.M. Peter, E.A. Ponomarev, A.B. Walker, and K.G.U. Wijayantha. Intensity dependence of the back reaction and transport of electrons in dye-sensitized nanocrystalline TiO_2 solar cells. *J. Phys. Chem. B*, 104(5):949–958, 2000.

[27] C. Flavin and M.H. Aeck. *Energy for Development: The Potential Role of Renewable Energy in Meeting the Millennium Development Goals*. Prepared for the Renewable Energy Policy Network by The Worldwatch Institute, 2005.

[28] Renewable Energy Policy Network for the 21st Century. *Renewables 2010 global status report*. 2010.

[29] S.R. Forrest. The limits to organic photovoltaic cell efficiency. *Mrs Bulletin*, 30(1):28–32, 2005.

[30] A.J. Frank, N. Kopidakis, and J. van de Lagemaat. Electrons in nanostructured TiO_2 solar cells: transport, recombination and photovoltaic properties. *Coordination chemistry reviews*, 248(13-14):1165–1179, 2004.

[31] R.H. Friend, R.W. Gymer, A.B. Holmes, J.H. Burroughes, R.N. Marks, C. Taliani, D.D.C. Bradley, D.A. Dos Santos, J.L. Bredas, and M. Lögdlun. Electroluminescence in conjugated polymers. *Nature*, 397(6715):121–128, 1999.

[32] E. Gatti, S. Micheletti, and R. Sacco. A new Galerkin framework for the drift-diffusion equation in semiconductors. *East West Journal of Numerical Mathematics*, 6:101–136, 1998.

[33] H. Gerischer and H. Tributsch. Electrochemische Untersuchungen zur spectraleu sensibilisierung von ZnO-Einkristallen. *Ber. Bunsenges. Phys. Chem*, 72:437–445, 1968.

[34] M. Grätzel. Conversion of sunlight to electric power by nanocrystalline dye-sensitized solar cells. *Journal of Photochemistry and Photobiology A: Chemistry*, 164(1-3):3–14, 2004.

[35] A.N.M. Green, E. Palomares, S.A. Haque, J.M. Kroon, and J.R. Durrant. Charge transport versus recombination in dye-sensitized solar cells employing nanocrystalline TiO_2 and SnO_2 films. *J. Phys. Chem. B*, 109(25):12525–12533, 2005.

[36] Energy & Strategy Group. *Solar Energy Report 2008.* Politecnico di Milano, School of Management, 2008.

[37] Energy & Strategy Group. *Solar Energy Report 2009.* Politecnico di Milano, School of Management, 2009.

[38] Gestore Servizi Elettrici gse s.p.a. http://www.gse.it.

[39] R.W. Gurney and N.F. Mott. Theory of the photolysis of silver bromide and photographic latent image. *Proc. R. Soc. Lond. A*, 164:151–167, 1938.

[40] A. Hagfeldt and M. Grätzel. Molecular photovoltaics. *Acc. Chem. Res*, 33(5):269–277, 2000.

[41] Heliatek Labs. Heliatek website. `http://www.heliatek.com/news-19`, 11-10-2010.

[42] S. Y. Huang. Charge recobination in dye-sensitzed nanocrystalline TiO_2 solar cells. *Journal of Physical Chemistry B,*, 48:2576–2582, 1997.

[43] T.J.R. Hughes. Multiscale phenomena: Green's functions, the Dirichlet-to-Neumann formulation, subgrid scale models, bubbles and the origins of stabilized methods. *Computer methods in applied mechanics and engineering*, 127(1-4):387–401, 1995.

[44] I. Hwang and N.C. Greenham. Modeling photocurrent transients in organic solar cells. *Nanotechnology*, 19:424012 (8pp), 2008.

[45] A. Iacchetti. Effetti della potenza incidente sull'efficienza dei fotorivelatori organici. Master's thesis, Politecnico di Milano, a.a. 2008-2009.

[46] J.W. Jerome. *Analysis of Charge Transport.* Springer-Verlag, Berlin Heidelberg, 1996.

[47] C. Johnson. *Numerical solution of partial differential equations by the finite element method*, volume 32. Cambridge university press Cambridge, 1987.

[48] A. Kambili, AB Walker, FL Qiu, AC Fisher, AD Savin, and LM Peter. Electron transport in the dye sensitized nanocrystalline cell. *Physica E: Low-dimensional Systems and Nanostructures*, 14(1-2):203–209, 2002.

[49] P.E. Van Keken, D.A. Yuen, and L.R. Petzold. DASPK: a new high order and adaptive time-integration technique with applications to mantle convection with strongly temperature-and pressure-dependent rheology. *Geophysical & Astrophysical Fluid Dynamics*, 80(1):57–74, 1995.

[50] P. Langevin. Recombinaison et mobilites des ions dans les gaz. *Ann. Chim. Phys*, 28:433, 1903.

[51] R.D. Lazarov and L.T. Zikatanov. An exponential fitting scheme for general convection-diffusion equations on tetrahedral meshes.

[52] A.C. Mayer, S.R. Scully, B.E. Hardin, M.W. Rowell, and M.D. McGehee. Polymer-based solar cells. *Materials Today*, 10(11):28–33, 2007.

[53] V.D. Mihailetchi, L.J.A. Koster, J.C. Hummelen, and P.W.M. Blom. Photocurrent generation in polymer-fullerene bulk heterojunctions. *Physical Review Letters*, 93(21):216601 (4pp), 2004.

[54] S. Molteni, F. Mazzotta, and B. Iandolo. Private communication. 2010.

[55] J. Moser. Notiz über die verstärkung photoelectrischer ströme durch optische sensibilisierung. *Monatsh. Chem*, 8:373, 1887.

[56] R.C. Nelson. Minority carrier trapping and dye sensitization. *J. Phys. Chem*, 169:705–713, 1965.

[57] M. Ni, M.K.H. Leung, D.Y.C. Leung, and K. Sumathy. An analytical study of the porosity effect on dye-sensitized solar cell performance. *Solar Energy Materials and Solar Cells*, 90(9):1331–1344, 2006.

[58] Council of the European Union. Press release 2785th council meeting environment. 2007.

[59] L. Onsager. Initial recombination of ions. *Physical Review*, 54(8):554–557, 1938.

[60] B. O'Regan and M. Grätzel. A low-cost, high-efficiency solar cell based on dye-sensitized colloidal TiO_2 films. *Nature*, 353:737–740, 1991.

[61] N. Papageorgiou, M. Grätzel, and PP Infelta. On the relevance of mass transport in thin layer nanocrystalline photoelectrochemical solar cells. *Solar Energy Materials and Solar Cells*, 44(4):405–438, 1996.

[62] M. Penny, T. Farrell, and C. Please. A mathematical model for interfacial charge transfer at the semiconductor-dye-electrolyte interface of a dye-sensitised solar cell. *Solar Energy Materials and Solar Cells*, 92(1):11–23, 2008.

[63] L.M. Peter and K.G.U. Wijayantha. Electron transport and back reaction in dye sensitised nanocrystalline photovoltaic cells. *Electrochimica Acta*, 45(28):4543–4551, 2000.

[64] A. Quarteroni and A. Valli. *Domain decomposition methods for partial differential equations*. Numerical mathematics and scientific computation. Clarendon Press, 1999.

[65] M. Redecker, DDC Bradley, M. Inbasekaran, and EP Woo. Nondispersive hole transport in an electroluminescent polyfluorene. *Applied Physics Letters*, 73:1565, 1998.

[66] Y. Roichman and N. Tessler. Generalized Einstein relation for disordered semiconductors — implications for device performance. *Applied Physics Letters*, 80:1948, 2002.

[67] T. Roubíček. *Nonlinear partial differential equations with applications*. Birkhauser, 2005.

[68] Royal Swedish Academy of Sciences. *The Nobel Prize in Chemistry, 2000: Conductive polymers*.

[69] A. Slaoui and R.T. Collins. Advanced Inorganic. *MRS bulletin*, 32, 2007.

[70] R.E. Smalley. Our energy challenge. *Public Lecture presented at Low Library, Columbia University*, 2003.

[71] T. Soga. *Nanostructured materials for solar energy conversion*. Elsevier Science Ltd, 2006.

[72] A. Stanley, B. Verity, and D. Matthews. Minimizing the dark current at the dye-sensitized TiO2 electrode. *Solar Energy Materials and Solar Cells*, 52(1-2):141–154, 1998.

[73] C.W. Tang. Two-layer organic photovoltaic cell. *Appl. Phys. Lett.*, 48:183, 1986.

[74] S.L.M. van Mensfoort and R. Coehoorn. Effect of gaussian disorder on the voltage dependence of the current density in sandwich-type devices based on organic semiconductors. *Phys. Rev. B*, 78, 2008.

[75] S. Wenger, M. Schmid, G. Rothenberger, M. Grätzel, and J. Schumacher. Model-based optical and electrical characterization of dye-sensitized solar cells. In *Proceedings of the 24th European Photovoltaic Solar Energy Conference and Exhibition*.

[76] W. West. First hundred years of spectral sensitization. *Proc. Vogel Cent. Symp. Photogr. Sci. Eng*, 18:35–48, 1974.

[77] J Williams. Finite element simulations of excitonic solar cells and organic light emitting diodes. Master's thesis, University of Bath, 2008.

[78] J. Williams and A.B. Walker. Two-dimensional simulations of bulk heterojunction solar cell characteristics. *Nanotechnology*, 19:424011, 2008.

[79] W.S. and Hans J. Queisser. Detailed balance limit of efficiency of p-n junction solar cells. *Journal of Applied Physics*, 32(3):510–519, 1961.

[80] J. Xu and L. Zikatanov. A monotone finite element scheme for convection-diffusion equations. *Mathematics of Computation*, 68(228):1429–1446, 1999.